



# Strojniški vestnik

## Journal of Mechanical Engineering



no. **6**

year **2022**

volume **68**

## Aim and Scope

The international journal publishes original and (mini)review articles covering the concepts of materials science, mechanics, kinematics, thermodynamics, energy and environment, mechatronics and robotics, fluid mechanics, tribology, cybernetics, industrial engineering and structural analysis.

The journal follows new trends and progress proven practice in the mechanical engineering and also in the closely related sciences as are electrical, civil and process engineering, medicine, microbiology, ecology, agriculture, transport systems, aviation, and others, thus creating a unique forum for interdisciplinary or multidisciplinary dialogue.

The international conferences selected papers are welcome for publishing as a special issue of SV-JME with invited co-editor(s).

## Editor in Chief

Vincenc Butala

University of Ljubljana, Faculty of Mechanical Engineering, Slovenia

## Technical Editor

Pika Škraba

University of Ljubljana, Faculty of Mechanical Engineering, Slovenia

## Founding Editor

Bojan Kraut

University of Ljubljana, Faculty of Mechanical Engineering, Slovenia

## Editorial Office

University of Ljubljana, Faculty of Mechanical Engineering

SV-JME, Aškerčeva 6, SI-1000 Ljubljana, Slovenia

Phone: 386 (0)1 4771 137

Fax: 386 (0)1 2518 567

info@sv-jme.eu, <http://www.sv-jme.eu>

**Print:** Demat d.o.o., printed in 250 copies

## Founders and Publishers

University of Ljubljana, Faculty of Mechanical Engineering, Slovenia

University of Maribor, Faculty of Mechanical Engineering, Slovenia

Association of Mechanical Engineers of Slovenia

Chamber of Commerce and Industry of Slovenia,

Metal Processing Industry Association

## President of Publishing Council

Mihael Sekavčnik

University of Ljubljana, Faculty of Mechanical Engineering, Slovenia

## Vice-President of Publishing Council

Bojan Dolšak

University of Maribor, Faculty of Mechanical Engineering, Slovenia

## International Editorial Board

Kamil Arslan, Karabuk University, Turkey

Hafiz Muhammad Ali, King Fahd U. of Petroleum & Minerals, Saudi Arabia

Josep M. Bergada, Politechnical University of Catalonia, Spain

Anton Bergant, Litostroj Power, Slovenia

Miha Boltežar, University of Ljubljana, Slovenia

Filippo Cianetti, University of Perugia, Italy

Janez Diaci, University of Ljubljana, Slovenia

Anselmo Eduardo Diniz, State University of Campinas, Brazil

Igor Emri, University of Ljubljana, Slovenia

Imre Felde, Obuda University, Faculty of Informatics, Hungary

Imre Horvath, Delft University of Technology, The Netherlands

Aleš Hribernik, University of Maribor, Slovenia

Soichi Ibaraki, Kyoto University, Department of Micro Eng., Japan

Julius Kaplunov, Brunel University, West London, UK

Iyas Khader, Fraunhofer Institute for Mechanics of Materials, Germany

Jernej Klemenc, University of Ljubljana, Slovenia

Milan Kljajin, J.J. Strossmayer University of Osijek, Croatia

Peter Krajnik, Chalmers University of Technology, Sweden

Janez Kušar, University of Ljubljana, Slovenia

Gorazd Lojen, University of Maribor, Slovenia

Darko Lovrec, University of Maribor, Slovenia

Thomas Lübben, University of Bremen, Germany

George K. Nikas, KADMOS Engineering, UK

Tomaž Pepelnjak, University of Ljubljana, Slovenia

Vladimir Popović, University of Belgrade, Serbia

Franci Pušavec, University of Ljubljana, Slovenia

Mohammad Reza Safaei, Florida International University, USA

Marco Sortino, University of Udine, Italy

Branko Vasić, University of Belgrade, Serbia

Arkady Voloshin, Lehigh University, Bethlehem, USA

## General information

Strojniški vestnik – Journal of Mechanical Engineering is published in 11 issues per year (July and August is a double issue).

Institutional prices include print & online access: institutional subscription price and foreign subscription €100,00 (the price of a single issue is €10,00); general public subscription and student subscription €50,00 (the price of a single issue is €5,00). Prices are exclusive of tax. Delivery is included in the price. The recipient is responsible for paying any import duties or taxes. Legal title passes to the customer on dispatch by our distributor. Single issues from current and recent volumes are available at the current single-issue price. To order the journal, please complete the form on our website. For submissions, subscriptions and all other information please visit: <http://www.sv-jme.eu>.

You can advertise on the inner and outer side of the back cover of the journal. The authors of the published papers are invited to send photos or pictures with short explanation for cover content.

We would like to thank the reviewers who have taken part in the peer-review process.

The journal is subsidized by Slovenian Research Agency.



### Cover:

A large amount of chicken feathers discarded as waste by several poultry-based industries is a serious solid-agricultural disposal issue. Additionally, several methods have been used to improve the properties of composite materials reinforced with natural materials. Here chicken feathers are trimmed by a pair of scissors to separate the avian fibres (barbs) from the quill (rachis) portion of the feathers for an average size of less than 1 cm. Polyester samples reinforced with chicken feather flakes immersed into a new topic, which is important for studying the effect of different solutions on creep behaviour.

Image Courtesy: Abed, B.H., Battawi, A.A., Khuder, A.W.H., Middle Technical University, Technical Engineering College-Baghdad, Iraq Republic  
© The Authors. CC BY 4.0 Int.

ISSN 0039-2480, ISSN 2536-2948 (online)

© 2022 with Authors.

SV-JME is indexed / abstracted in: SCI-Expanded, Compendex, Inspec, ProQuest-CSA, SCOPUS, TEMA. The list of the remaining bases, in which SV-JME is indexed, is available on the website.

Strojniški vestnik - Journal of Mechanical Engineering is available on <https://www.sv-jme.eu>.

# Contents

**Strojniški vestnik - Journal of Mechanical Engineering**  
**volume 68, (2022), number 6**  
**Ljubljana, June 2022**  
**ISSN 0039-2480**

**Published monthly**

## **Papers**

Balsam H. Abed, Ali A. Battawi, Abdul Wahab H. Khuder: Effect of Immersion Media for Polyester Composite Reinforced with Chicken Feathers on Creep Behaviour	377
Yunyue Xie, Qingliang Zeng, Kao Jiang, Zhaosheng Meng, Qinghai Li: Investigation of Dynamic Behaviour of Four-Leg Hydraulic Support under Double-Impact Load	385
HudaElsalam Mohamed, Unal Camdali, Atilla Biyikoglu, Metin Actas: Enhancing the Performance of a Vapour Compression Refrigerator System Using R134a with a CuO/CeO <sub>2</sub> Nano-refrigerant	395
Tie Zhang, Yachao Cao, Guangcai Ma: Indices to Evaluate the Performance of Force Transmission and Constraint for Parallel Mechanisms	411
An-Le Van, Trung-Thanh Nguyen: Optimization of Friction Stir Welding Operation using Optimal Taguchi-based ANFIS and Genetic Algorithm	424
Kanmani Ganesan, Saravanan Sambasivam, Rajesh Ramadass: Determination of Limiting Dome Height (LDH) Values for Inconel 718 Alloy Sheet Using FEA and a Hemispherical Punch Method	439



# Effect of Immersion Media for Polyester Composite Reinforced with Chicken Feathers on Creep Behaviour

Balsam H. Abed\* – Ali A. Battawi – Abdul Wahab H. Khuder  
Middle Technical University, Technical Engineering College-Baghdad, Iraq

*The use of composite materials has expanded in industrial applications around the world, reinforcing composites with waste materials like chicken feather is one of the effective ways to solve environmental concerns compared to traditional methods, as it is considered one of the renewable and inexpensive methods, in addition to its presence in abundance. The main added feature of composite materials over classic materials are the light weight. This paper investigates the effect of immersion media for a polyester composite reinforced with chicken feather fillers to enhance the creep characteristic. The composite was manufactured using a hand-layup process. The samples were produced by varying the weight ratios of fibre loading (0 %, 0.2 %, 0.4 %, 0.6 %, and 0.8 %) and immersed in three different media (KCl (salt media), NaOH (alkali media) and HNO<sub>3</sub> (acid media)). The creep samples were tested according to ASTM standards. The results show that chicken feather-reinforced composites immersed in various media have probable applications because of their superior mechanical properties over non-reinforced composites.*

**Keywords: immersed, chicken feather, polyester composite, creep behaviour, reinforcement**

## Highlights

- In this study, three different media were used to immerse polyester composites
- When compared to standard methods, reinforcing composites with waste materials such as chicken feathers is one of the most effective approaches to address environmental concerns.
- This study looked at the effect of creep behaviour on a polyester composite reinforced with chicken feather; there are few investigations on this type of test exist in comparison to when compared to the other mechanical properties.

## 0 INTRODUCTION

Due to disposal and pollution, chicken feather fibres have a prevalent concern. This has a severe influence on the environment; however, current study reveals that chicken feather waste may be used as reinforcement instead of being burned [1]. However, industries are primarily concentrating on the notion of sustainable manufacturing, which involves limiting the use of non-renewable resources and implementing environmentally friendly material processes, such as waste recycling and reuse. Composite materials are manufactured for this purpose, and substantial study is being out by researchers in many regions of the world. [2] and [3]. Chicken feathers comprise 91 % protein (keratin), 8 % water and 1 % lipids [4].

Several attempts had been made throughout the past decades to evaluate the potential of chicken feathers as reinforcements in applications of composite materials. Abed et al. [5] investigate the creep behaviour of an epoxy composite reinforced with Yttrium Oxide Powder at different weight ratios. Each volume ratio was subjected to five loads at a steady temperature. The creep behaviour of epoxy composite was studied using both experimental and computational methods.

Šafarič et al. [6] evaluated the use of wood waste with poultry feather waste to produce natural insulating fibreboard composite. The fibreboard composite was set using various amounts of poultry feather waste (20 % to 70 %) and wood waste, resembling mixed wood remains or wood shavings. The thermal and mechanical properties were studied, along with their biodegrading abilities. Oladele et al. [7] utilized brown chicken feather fibres to reinforce polyethylene as a substitution for synthetic fibres to improve mechanical properties of polyethylene, using varying ratios of fibre (2 wt.%, 4 wt.%, 6 wt.%, 8 wt.% and 10 wt.%) with the polyethylene matrix. The flexural modulus and tensile properties for each ratio were studied. In addition, scanning electron microscopy (SEM) and X-ray diffraction (XRD) were performed.

Abed and Battawi [8] investigated the creep behaviour of polystyrene composites reinforced with natural fibre at various weight fractions, constant loads, and temperatures. Hand layup technique was used to build the manufacturing setup for composite materials. Maxwell techniques were utilized to derive the stress and modulus of elasticity from the strain time curve using curve-fitting methods.

Reddy et al. [9] showed that chicken feathers could be used as a matrix to build total biodegradable

composites with properties comparable to those of polypropylene composites, even using jute fibre reinforcements. Using feathers as a matrix allows for 100 % biodegradable composites containing feathers or other bio-polymers as reinforcement at a low cost.

Amieva et al. [10] explored extrusion-processed chicken feathers for making recycled polypropylene compounds. The specimen density and thermal, morphological, and thermo-mechanical properties were assessed. The density of the composite material was lower than that of the non-recycled material. When compared to polypropylene compounds, the transition temperature of the composite materials remained unchanged.

The influence of creep behaviour on polyester composite reinforced with chicken feather was the subject of this research. In comparison to the rest of the mechanical properties, there are few studies on this type of test.

## 1 EXPERIMENTAL

### 1.1 Preparation of Fillers

The chicken feathers were gathered from poultry production units. They were first cleaned with ethanol, then washed five times with tap water and exposed to the sun for two days until they dried entirely. The dried chicken feathers were trimmed with scissors to separate the avian fibres (barbs) from the quill (rachis) portion of the feathers, as shown in Fig. 1. The average size of 1 cm was considered for chicken feather samples.



Fig. 1. Dried feathers

### 1.2 Sample Fabrication

Polystyrene (Ps) granules were dissolved by adding chloroform and mixing with a magnetic stirrer.

Liquid polyester (Up) was prepared separately and added to the Ps mixture at a 92:8 ratio of polyester to polystyrene and stirred for 3 h [8]. Thereafter, an appropriate hardener (K-6) was added to the solution in the recommended proportion (10:1) and stirred for 15 min. A rubber mould was initially gently washed, and liberated from moisture and dust. A thin layer of wax was then added along with its base plate to the inner walls of the rubber mould for quick removal of the cast after drying. Previously prepared avian fibres (dried chicken feathers) were laid longitudinally inside the mould with weight ratios (0 %, 0.2 %, 0.4 %, 0.6 %, and 0.8 %). The Up-Ps resin mixture was then poured over them using a hand lay-up method. Care was taken to prevent air bubble formation. Samples were kept in the mould for 18 h and subsequently placed in an oven at 55 °C for 3 h to rid the moisture.

### 1.3 Immersion Media

In the present work, samples were immersed in different media, as salt media (KCl), alkali media (NaOH), and acid media (HNO<sub>3</sub>), as shown in Fig. 2, at a rate of 5 % for 4 h. The samples were then washed with tap water and left to dry. Fig. 3 illustrates a creep sample of Up-Ps reinforced with different weight ratios of chicken feathers and immersed in the three media.



Fig. 2. Samples immersed in different media

### 1.4 Testing

The creep characteristics of the Up-Ps composites were estimated by creep testing. The tests were conducted according to ASTM D2990 [8] at a constant temperature of 21 °C using the creep testing machine model WP600, as shown in Fig. 4. A total of 45 creep tests were performed for all volume ratios (0 %, 0.2

%, 0.4 %, 0.6 %, and 0.8 %). Each ratio was tested three times to obtain an average. The load was applied for 1 hour, then removed, and readings were taken continuously for another hour.



Fig. 3. Creep sample of Ps-Up reinforced



Fig. 4. Creep testing machine (WP600) with chicken feathers

## 2 RESULTS AND DISCUSSION

A creep test was used to determine the mechanical properties (strain, stress, and modulus of elasticity) of the polyester composites reinforced with chicken feathers at 0.2 wt.%, 0.4 wt.%, 0.6 wt.%, and 0.8 wt.% and immersed in the three different media (salt, alkali, acid) at 26 °C atmospheric temperature. All the samples successfully carried the equivalent load for 1 hour. For the estimation, three samples were examined for mechanical properties, and the values were averaged.

Curve-fitting techniques, as shown in Fig. 5, were used for the extraction of stress and modulus

of elasticity) from the strain-time curve using the Maxwell method (spring and dashpot in series) [11].

$$\sigma(t) = \sigma_0 e^{-\frac{\delta_1 \cdot t}{\eta_1}}, \tag{1}$$

$$\delta_1 = \frac{\sigma_0}{\varepsilon_1}, \tag{2}$$

$$\eta_1 = \frac{\sigma_0}{\tan \beta}, \tag{3}$$

$$\varepsilon^- = \tan \beta = \frac{\Delta \varepsilon}{\Delta t} \cdot \frac{1}{S}, \text{ where } \varepsilon = \frac{\Delta L}{L}, \tag{4}$$

$$E(t) = \frac{\sigma(t)}{\varepsilon(t)} = \frac{\delta_1 \cdot \eta_1}{\eta_1 + \delta t}, \tag{5}$$

$$\varepsilon(t) = \frac{\sigma}{\varepsilon_1} + \frac{\sigma}{\eta_1} t. \tag{6}$$

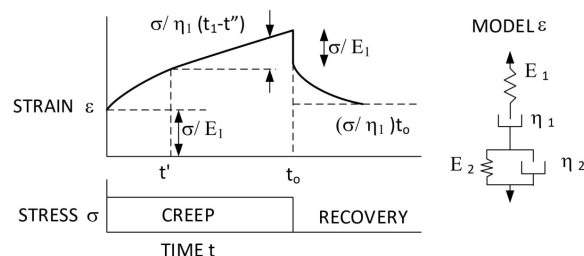


Fig. 5. Maxwell method (spring and dashpot in series)

### 2.1 Immersion in Salt Medium

Fig. 6 demonstrates creep behaviour (strain vs time) in KCl. The composite with 0.6 wt.% chicken feathers performed better than the other weight fractions in the salt medium, which yielded an 86.2 % enhancement in strain compared with pure polyester. All the reinforced composites showed a decrease in strain compared to the non-reinforced composite. The 0.4 wt.% chicken feather composite had the least strain among the reinforced composites, resulting in 47.6 % when compared to pure polyester. The deformation was seen to develop in three distinct stages: elastic, yielding, and a plastic deformation zone.

The stress vs time graphs for all reinforcements in salt media are shown in Fig. 7. The composite with 0.2 wt.% of chicken feathers achieved the highest percentage of stress (100.05 % stress improvement over pure polyester) in the salt media compared with other weight fractions. The composite with 0.4 wt.% achieved only 99.998 %, the lowest percentage of the

weight fractions, which indicates that immersing in KCl enhance the creep behaviour of the composites.

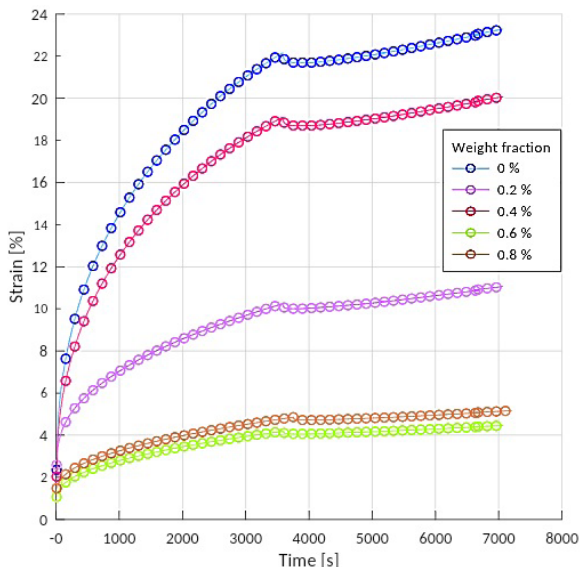


Fig. 6. Strain behaviour of polyester reinforced with different weight fraction of chicken feather immersed in KCl media

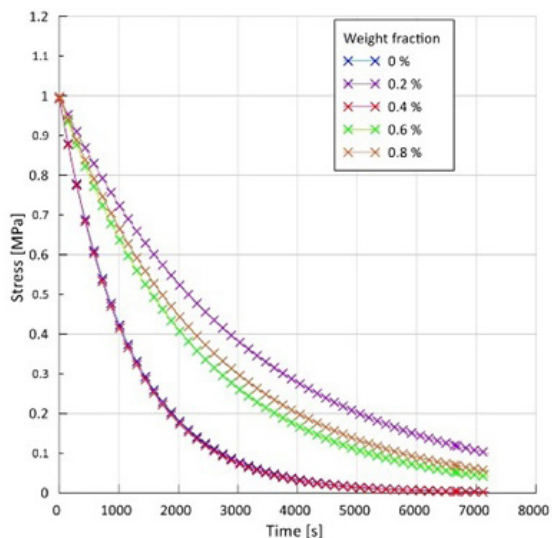


Fig. 7. Stress vs time for polyester reinforced by different chicken feather weight fraction immersed in KCl media

Fig. 8 represents the modulus of elasticity with time in the salt medium. The results revealed that the 0.2 wt.% chicken feather composite performed better than the other weight fractions in the salt medium, which yielded a 2.422 % enhancement in elasticity as compared with pure polyester. The 0.4 wt.% sample achieved the smallest improvement of 1.138 %. These findings imply that a fibre content of 0.2 wt.% is the ideal weight fraction for improving the property.

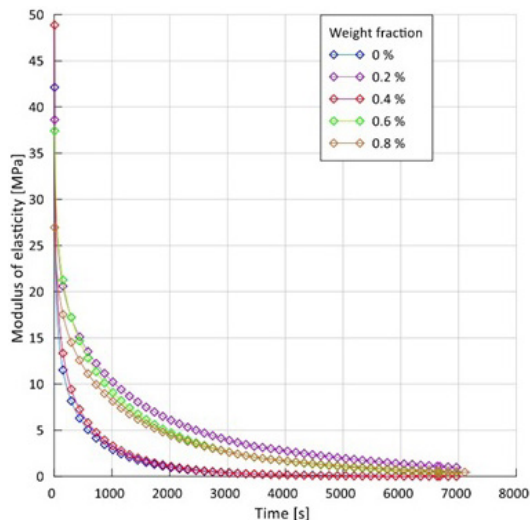


Fig. 8. Modulus of elasticity for polyester reinforced by different weight fraction of chicken feather immersed in KCl media

## 2.2 Immersion in Alkali Medium (NaOH)

The strain vs time graphs for all reinforcements in the alkali medium are shown in Fig. 9. The composite with 0.4 wt.% of chicken feathers exhibited a higher percentage of strain in the alkali medium compared with other weight fractions and yielded a 75 % enhancement in the strain as compared with pure polyester. The composite with 0.8 wt.% achieved only 43.12 %, which was the smallest percentage.

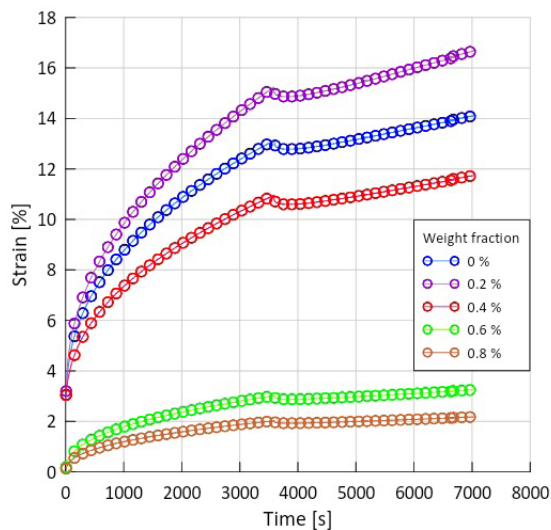


Fig. 9. Strain vs time for polyester reinforced by different weight fraction of chicken feather immersed in NaOH media

Fig. 10 demonstrates stress vs time graphs for all reinforcements in the alkali medium. The results

revealed that the 0.4 wt.% chicken feather composite had a better result than the other weight fractions, achieving 100.06 % stress improvement compared with pure polyester. The 0.2 wt.% sample achieved only 100.30 %, the lowest percentage of the weight fractions.

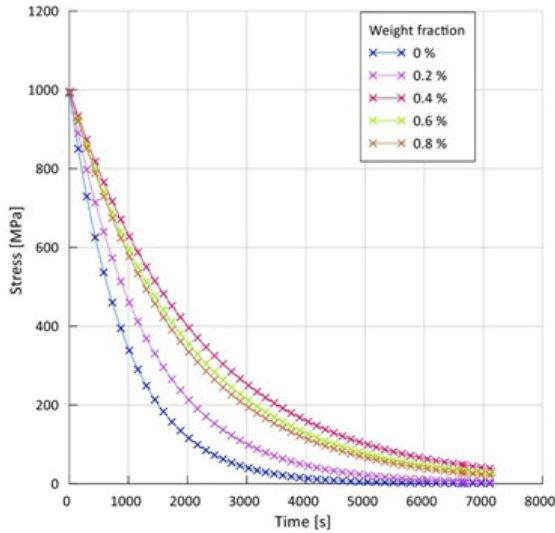


Fig. 10. Stress vs time for polyester reinforced by different weight fraction of chicken feather immersed in NaOH media

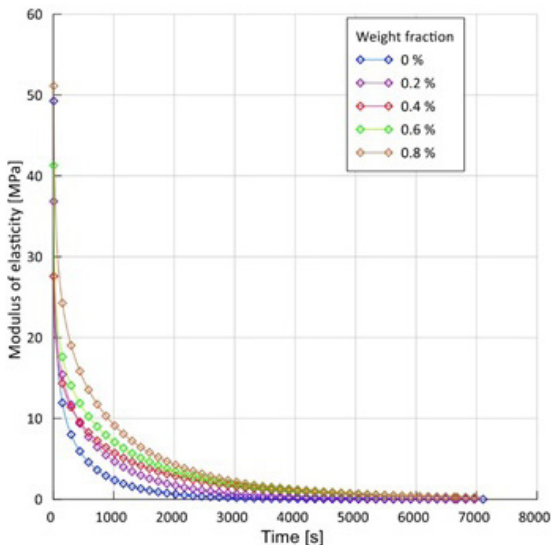


Fig. 11. Modulus of elasticity vs time for polyester reinforced by different weight fraction of chicken feather immersed in NaOH media

The modulus of elasticity vs time graphs for all reinforcements in the alkali medium are shown in Fig. (11). The composite with 0.8 wt.% had a higher percentage of modulus of elasticity in the alkali medium compared with other weight fractions,

recording a 2.32 % improvement in modulus of elasticity as compared with pure polyester. The 0.2 wt.% chicken feather composite had the lowest modulus of elasticity (1.42 %) as compared to pure polyester.

### 2.3 Immersion in Acidic Medium (HNO<sub>3</sub>)

Fig. 12 shows that strain vs time graphs for all reinforcements in the acidic medium. The results showed 0.2 wt.% chicken feather composite had a better strain than the other weight fractions in the acidic medium, yielding 112.5 % strain improvement compared with pure polyester. The 0.8 wt.% chicken feather composite had the lowest strain enhancement among the other samples, as it improved strain by (36.7 %) when compared to pure polyester. Because delamination increased after being submerged in acidic medium, the effect of acidic media on creep strain is relatively mild.

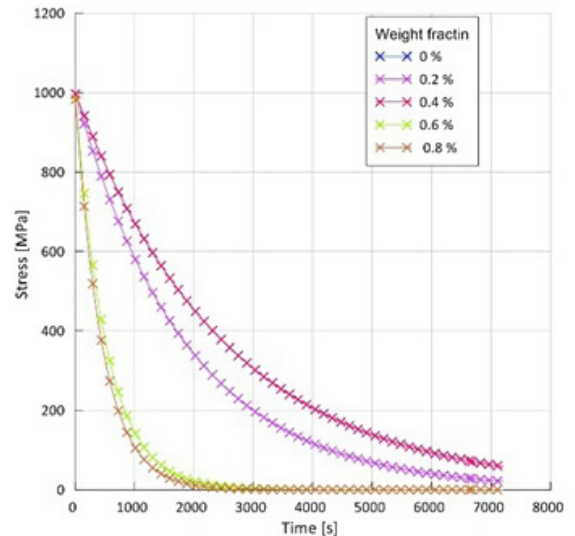
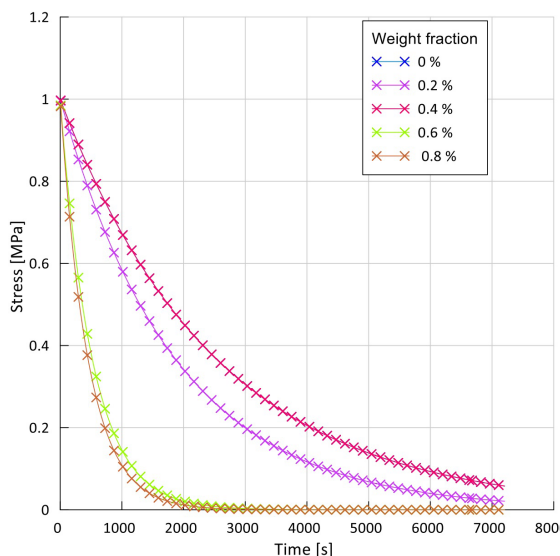


Fig. 12. Strain vs time for polyester reinforced by different weight fraction of chicken feather immersed in HNO<sub>3</sub> media

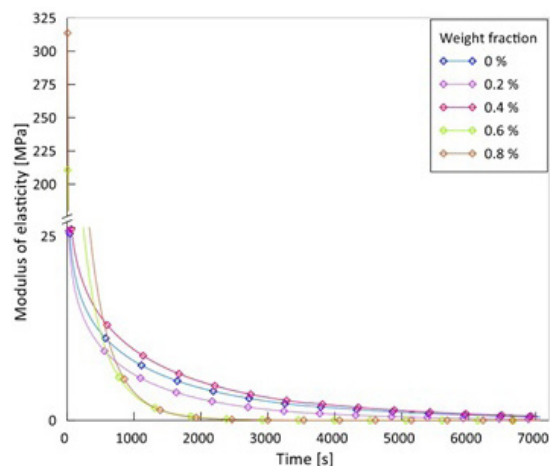
The stress vs time graphs for all reinforcements in the acidic medium are shown in Fig. 13. The results showed that 0.4 wt.% chicken feather composite outperformed the other weight fractions in the acidic medium, resulting in a 100.001 % enhancement in stress compared with pure polyester. The 0.8 wt.% achieved only 99.81 %, with was the smallest percentage among the weight fractions.

Fig. 14 depicts the modulus of elasticity vs time graphs for all reinforcements in acidic media. The 0.8 wt.% sample had a higher percentage increase of modulus of elasticity in the acidic medium than

the other weight fractions, which was 2.719 % when compared to pure polyester. The 0.2 wt.% only achieved 0.88 %, the smallest percentage among the weight fractions.



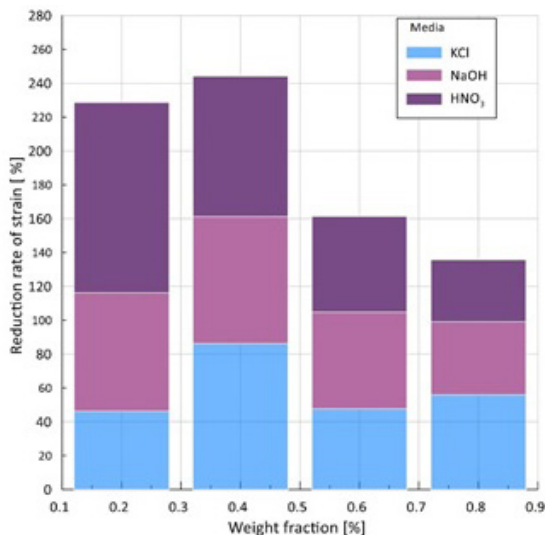
**Fig. 13.** Stress vs time for polyester reinforced by different chicken feather weight fraction immersed in  $HNO_3$  media



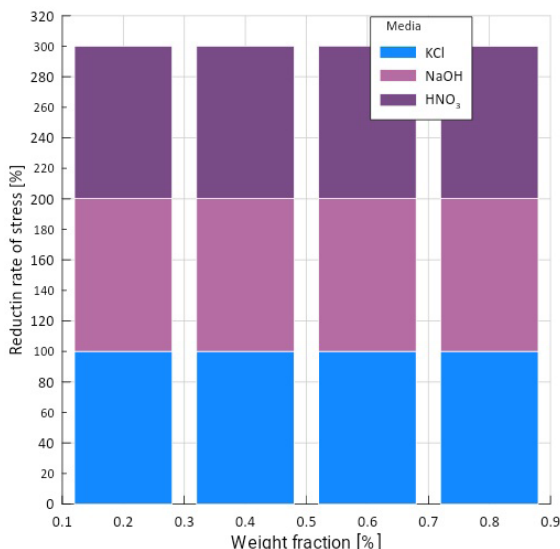
**Fig. 14.** Modulus of elasticity for polyester reinforced by different weight fraction of chicken feather immersed in  $HNO_3$  media

Fig. 15 clearly shows the comparison between the three different media (salt, alkali, and acid) on the percentage rate of creep strain. Of note, the strain decreases with increasing weight fraction of chicken feathers, which indicates the matrix's engagement with the filler was satisfactory. In addition, the percentage rates of creep stress in the three different media are compared in Fig. 16. The stress increased gradually with the increase of weight fractions of chicken feathers. Therefore, using chicken feathers

as a reinforcement material might have slowed the crack's progression and allowed the load to be held. Finally, Fig. 17 represents the comparison of the percentage rate of creep modulus of elasticity in the three media (salt, alkali, and acidic), showing that the modulus of elasticity increased with increasing weight fraction of chicken feathers.



**Fig. 15.** A comparative study for the effect of KCl, NaOH, and  $HNO_3$  media on the percentage rate of creep strain



**Fig. 16.** A comparative study for the effect of KCl, NaOH, and  $HNO_3$  media on the percentage rate of creep stress

### 3 CONCLUSION

The study was conducted to develop materials for engineering applications using poultry wastes that are

produced daily around the world. These composites, which are manufactured at a low cost and have superior properties, may be useful in light structural and other engineering applications. In the present study, a polyester composite was reinforced with chicken feathers at different weight fractions using the hand lay-up technique. The results demonstrated that chicken feather-reinforced composites immersed in various media have probable applications because of their superior mechanical properties over immersed for reinforced and non-reinforced composites.

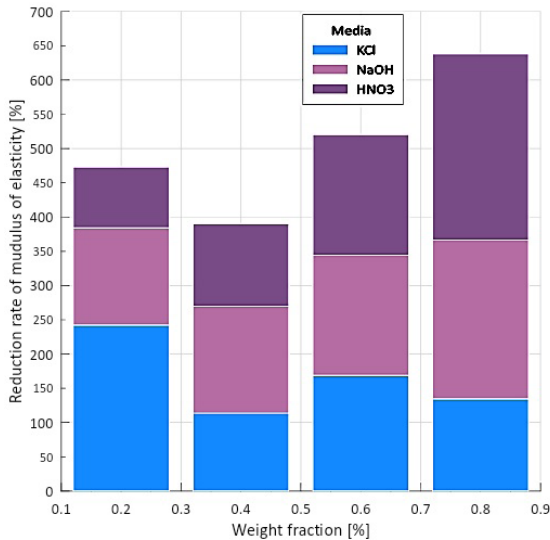


**Fig. 17.** A comparative study for the effect of KCl, NaOH, and HNO<sub>3</sub> media on the percentage rate of creep modulus of elasticity

Polyester composites reinforced with 0.2 wt.% chicken feathers and immersed in the acidic medium had better strain enhancements compared with those immersed in other media and compared with pure polyester and Acidic media have minimal influence on the bonding between the fibres and Up. However, the composite of 0.4 wt.% of chicken feather immersed in the alkali medium showed maximum stress improvement over pure polyester compared with other immersed media. The salt medium improved the modulus of elasticity for the polyester composite at 0.8 wt.% of chicken feathers the most compared with pure polyester and the samples in other immersed media. A literature review revealed that low weight fractions of chicken feather content have resulted in improved mechanical properties of polyester composite in various media. Natural resources have been re-used in a variety of industries as a way of disposal. As a result, the necessity of recycling composites in general and employing them in new applications is emphasized in this study.

#### 4 NOMENCLATURES

- $\sigma_0$  initial stress [MPa]  
 $\sigma(t)$  stress at any time [MPa]  
 $\delta_1$  spring constant [MPa]  
 $\varepsilon_1$  Maxwell element, [-]  
 $\eta_1$  dashpot constant, [MPa·s]  
 $E(t)$  creep modulus in function of time, [MPa]  
 $\varepsilon(t)$  strain in function of time, [-]  
 $t$  time, [s]  
 $\beta$   $\tan^{-1}$  Maxwell element [s]  
 $\varepsilon^-$  the slope of Eq. (4) at ( $t=t_1$ ) [1/s]  
 $L$  gauge length [mm]  
 $e$  Euler's number (2.7)

#### 5 REFERENCES

- [1] Vinodh kumar, S., Prasanth, K., Prashanth, M., Prithivirajan, S., Anil Kumar, P. (2021). Investigation on mechanical properties of chicken feather fibers reinforced polymeric composites. *Materials Today: Proceedings*, vol. 37: p. 3767-3770, DOI:10.1016/j.matpr.2020.10.877.
- [2] Ramesh, M., Palanikumar, K., Reddy, K.H. (2017). Plant fibre based bio-composites: Sustainable and renewable green materials. *Renewable and Sustainable Energy Reviews*, vol. 79, p. 558-584, DOI:10.1016/j.rser.2017.05.094.
- [3] Anandkumar, R., Ramesh Babu, S., Sathyamurthy, R. (2021). Investigations on the mechanical properties of natural fiber granulated composite using hybrid additive manufacturing: A novel approach. *Advances in Materials Science and Engineering*, vol. 2021, art. ID 5536171, DOI:10.1155/2021/5536171.
- [4] Prabhakar, K., Debnath, S., Ganesan, R., Palanikumar, K. (2018). A review of mechanical and tribological behaviour of polymer composite materials. *IOP Conference Series: Materials Science and Engineering*, vol. 344, art ID 012015, DOI:10.1088/1757-899X/344/1/012015.
- [5] Abed, B.H., Jadee, K.J., Battawi, A.A. (2020). Experimental and numerical study on the effect of creep behaviour on epoxy composites reinforced with yttrium oxide powder. *International Journal of Applied Mechanics and Engineering*, vol. 25, no. 4, p. 203-213, DOI:10.2478/ijame-2020-0059.
- [6] Šafarič, R., Fras Zemljič, L., Novak, M., Dugonik, B., Bratina, B., Gubeljak, N., Bolka, S., Strnad, S. (2020). Preparation and characterisation of waste poultry feathers composite fibreboards. *Materials*, vol. 13, no. 21, art. ID. 4964, DOI:10.3390/ma13214964.
- [7] Oladele, I.O., Okoro, A.M., Omotoyinbo, J.A., Khoathane, M.C. (2018). Evaluation of the mechanical properties of chemically modified chicken feather fibres reinforced high density polyethylene composites. *Journal of Taibah University for Science*, vol. 12, no. 1, p. 56-63, DOI:10.1080/16583655.2018.1451103.
- [8] Abed, B.H., Battawi, A.A. (2021). Effect of fish scales on fabrication of polyester composite material reinforcements. *Open Engineering*, vol. 11, no. 1, p. 915-921, DOI:10.1515/eng-2021-0092.

- [9] Reddy, N., Jiang, J., Yang, Y. (2014). Biodegradable composites containing chicken feathers as matrix and jute fibers as reinforcement. *Journal of Polymers and the Environment*, vol. 22, no. 3, p. 310-317, DOI:10.1007/s10924-014-0648-9.
- [10] Amieva, E.J.-C., Velasco-Santos, C., Martínez-Hernández A.L., Rivera-Armenta, J.L., Mendoza-Martínez, A.M., Castaño, V.M. (2015). Composites from chicken feathers quill and recycled polypropylene. *Journal of Composite Materials*, vol. 49, no. 3, p. 275-283, DOI:10.1177/0021998313518359.
- [11] Bharadwaj, M., Claramunt, S., Srinivasan, S. (2017). Modeling creep relaxation of polytetrafluorethylene gaskets for finite element analysis. *International Journal of Materials, Mechanics and Manufacturing*, vol. 5, no. 2, p. 123-126, DOI:10.18178/ijmmm.2017.5.2.302.

# Investigation of Dynamic Behaviour of Four-Leg Hydraulic Support under Double-Impact Load

Yunyue Xie<sup>1</sup> – Qingliang Zeng<sup>2</sup> – Kao Jiang<sup>3</sup> – Zhaosheng Meng<sup>3,\*</sup> – Qinghai Li<sup>3</sup> – Junming Zhang<sup>3</sup>

<sup>1</sup> Shandong University of Science and Technology, Shandong Key Laboratory of Civil Engineering Disaster Prevention and Mitigation, China

<sup>2</sup> Shandong University of Science and Technology, College of Mechanical and Electronic Engineering, China

<sup>3</sup> Shandong University of Science and Technology, State Key Laboratory of Mining Disaster Prevention and Control Co-founded by Shandong Province and the Ministry of Science and Technology, China

*Hydraulic support is the key support equipment for underground coal mining. The frequent impact load during the mining process easily causes damage to the hinge joints and reduces the stability of the hydraulic support. To improve the stability of the hydraulic support, a rigid-flexible coupling numerical model of the support has been developed. The validity of the model is verified through the static loading test. Next, the impact loading test of the hydraulic support is carried out. The force response characteristics of the hinge joints and the vibration response characteristics of the leg system are discussed when both the canopy and goaf shield bear impact load. The results indicate that when only the canopy bears the impact load, the hinge joint of the front leg is the most sensitive (up to 139.4 %). When the impact load acts both on the canopy and goaf shield, the dynamic response of each hinge joint of the hydraulic support (except the rear leg) reaches the peak value. With the backward movement of the impact load on the goaf shield, the hinge joint force presents different pressure-relief characteristics.*

**Keywords:** impact load, four-leg hydraulic support, double-impact, force transmission, numerical simulation

## Highlights

- Taking the four-leg hydraulic support as the research subject, a rigid-flexible coupling numerical model of the support is established to investigate its dynamic behaviour.
- The dynamic response of the four-leg hydraulic support under no-impact, single-impact, and double-impact loads has been compared, proving the necessity of research on the dynamic behaviour of the four-leg support under double-impact loads.
- By applying static load to the canopy, the static force response of the hinge joints and stiffness response of the support are analysed.
- By applying random impact load to the canopy and goaf shield, the dynamic response of the four-leg support under the double-impact load is analysed. This study provides new research ideas and methods for the dynamic performance analysis of other mechanical equipment.

## 0 INTRODUCTION

Coal is the most critical primary energy source in China. Coal resources will still account for more than 54 % of China's energy consumption by 2050. Therefore, in the foreseeable long term, the safe, efficient, and clean mining of coal resources will remain an important topic for the development of China's coal industry [1] to [3].

Hydraulic support is the key support equipment to ensure safe underground coal mining. It is mainly used to support the roof and push the armoured face conveyor during the mining process, thus enabling a safe working space for underground mining. Therefore, the support stability of hydraulic support is one of the key factors that determine safe coal mining [4]. During the normal operation period, the hydraulic support mainly bears the static gravity load coming from the roof. However, in the periodic pressure stage, the violent movement of the roof will produce a strong impact load on the hydraulic

support, deteriorate the stability of the support, reduce the support performance of the hydraulic support, and even damage the hydraulic support. Especially in recent years, with the continuous consumption of shallow coal resources, coal mining engineering has gradually been developed for the deeper parts of the earth, and the mining intensity and mining height have also been significantly improved. These all lead to the increase in the frequency and strength of the impact load acting on the hydraulic support, which puts forward higher requirements for the impact resistance performance of the hydraulic support [5] to [9]. The connection hinge joints of hydraulic support are the most sensitive structure to impact load. Therefore, studying the dynamic response characteristics of the hinge joint of hydraulic support under impact load is helpful in designing high-strength anti-impact support and ensuring the safety of underground mining operations.

Since the support performance of hydraulic support has a great impact on safe and efficient

\*Corr. Author's Address: State Key Laboratory of Mining Disaster Prevention and Control Co-founded by Shandong Province and the Ministry of Science and Technology, Qingdao, China, skdmzs@163.com

mining, scholars throughout the world have carried out much research on it. At the level of the impact load formation mechanism, Wang et al. analysed the energy transformation relationship before and after the basic roof fracture. By establishing the catastrophe mathematical model of the basic roof, the influence of the fracture position on the roof impact load amplitude has been studied [10] and [11]. Though establishing the stope numerical model using UDEC, Liu et al analysed the harmfulness of rock burst under different impact velocities [12]. Tan et al. analysed the rock properties, coal rock height ratio, and other parameters on the occurrence frequency and strength of rock burst and proposed a new impact energy release index (considering time effect) and coal seam impact performance evaluation method. Based on this method, the impact load acting on the hydraulic support system under different geological conditions are obtained [13]. By establishing a two-dimensional plain model of the stope (including the hydraulic support structure) using FLAC, Singh and Singh [14] and [15] and Verma [16] analysed the strata behaviour and support performance in longwall mining. Based on this model, Singh obtained the optimal design criterion for hydraulic support capacity. However, the hydraulic support is regarded as a static support unit in their model, which cannot accurately describe the passive elastic support behaviour of hydraulic support [17]. To analyse the static support performance of hydraulic support, Marcin performed a numerical simulation and laboratory test on a two-legged shield support. By putting 24 small cylinders under the base, 10 strain gauges, and 5 inclinometers on the support in the laboratory test, changes in base pressures, stress values, and geometries of the support during static loading were evaluated. This testing process is well reproduced in the numerical simulation [18]. Lin et al. [19] conducted a static simulation and experiment on a hydraulic support, by changing the contact mode between the pin and shaft hole, the effects of the boundary conditions on the stress distribution are discussed. He concluded that the bonded contact mode is the best way to simulate the experiment results. At the level of dynamic characteristic analysis of hydraulic support, Wang et al. [20] first proposed simulating the hydraulic support leg system by using linear elastic dynamic element and put forward the impact dynamic model of a leg-relief valve system. By introducing the parameters of real hydraulic legs, the dynamic response behaviour of the leg system under impact load is analysed. Based on this elastic equivalent assumption, Liang et al. [21] introduced the rigid-flexible coupling numerical analysis method

to the hydraulic support and discussed the dynamic response characteristics of the hydraulic support. However, in his study, the yield characteristics of the relief valve of the leg system are not considered, and the leg system is regarded as a constant stiffness spring. On this basis, Meng et al. [22] and [23] further analysed the dynamic response of the two-leg hydraulic support under impact load after introducing the yield characteristics of the leg system. They pointed out that the stress state at the equilibrium jack of two-leg support is significantly reduced under the improved simulation scheme. Subsequently, Xie et al. [24] put forward the segmented stiffness characteristics of the hydraulic support leg system, including the two-stage stiffness equivalent method of the leg system. Based on this method, the load of the shield hydraulic support connection joints under the deep well dynamic load is obtained, and the base pressure distribution characteristics of the hydraulic support under this load is discussed [25] and [26]. Hu [27] established the mechanical model of the four-leg hydraulic support based on the D-Alembert principle and discussed the dynamic impact characteristics of the support on the connection hinge joints at different action speeds during its raising process. Ren et al. [28] firstly compared the credibility of the elastic equivalent rigid-flexible coupling numerical simulation method by building a 1:2 impact loading test bed. By applying concentrated impact load to the canopy of the shield support of the experimental test bed and numerical simulation model, respectively, the energy transfer and dissipation characteristics of the two-leg support system are studied. To obtain the adaptability of four-leg hydraulic support with large mining height, Wang et al. [29] applied different impact loads to the canopy and goaf shield respectively, and the evaluation method of the canopy and goaf shield under impact is obtained.

By summarizing the literature, it can be determined that the current studies mainly focused on the formation mechanism of stope impact load or the static performance analysis of the hydraulic support. The few research studies related to the dynamic behaviour of hydraulic support mainly discuss the dynamic response characteristics of two-leg support when a single canopy or goaf shield is subjected to the external load. Due to the randomness of the roof load, the canopy and goaf shield of the hydraulic support may bear the impact loads of both.

However, there is no literature referring to the dynamic response characteristics of four-leg hydraulic support when the canopy and goaf shield are subjected to the impact load both. Therefore, a multi-body

dynamic model of the four-leg hydraulic support based on rigid-flexible coupling is established in this study. By applying the initial static load on the action line of the legs and applying the double-impact point load at different positions of the canopy and goaf shield, the force response characteristics of the hinge joints and the vibration characteristics of the legs are analysed. This study helps to improve the strength characteristic analysis theory of hydraulic support under impact load and provides theoretical support for the structural design and optimization of anti-impact hydraulic support.

## 1 MATERIALS AND METHODS

### 1.1 Definition of Numerical Model for Four-Leg Hydraulic Support

The ZZ 18000/33/72 type four-leg large mining height hydraulic support is chosen as the research prototype (as shown in Fig. 1), where 1 is the canopy, 2 is the front leg, 3 is the base, 4 is the goaf shield, 5 is the rear bar, 6 is the front bar, 7 is the rear leg, a–c are the hinge joints between each part. The working height of the ZZ 18000/33/72 type support ranges from 3.2 m to 7.2 m, and its rated working resistance is 18000 kN. During the working process, the canopy contacts the direct roof and bears the dynamic roof load directly. Then, the canopy transmits these loads to the goaf shield, connection bars and base through the hinge joints. Due to the frequent impact load, the hinge joints tend to bend and fracture easily (see Fig. 1).

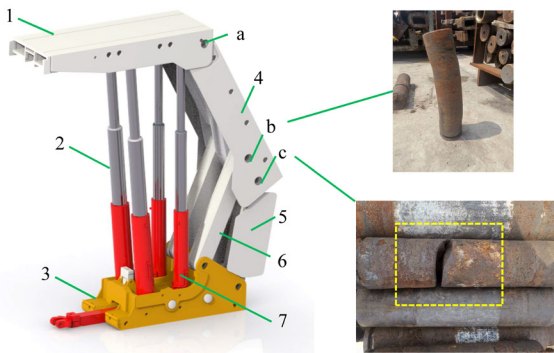


Fig. 1. ZZ 18000/33/72 type four-leg large mining height hydraulic support

In this study, the multi-dynamic software ADAMS is used to establish the rigid-flexible coupling model of the support. The operation height of the support is set to 7.2 m in the simulation model. The base is defined as rigid and bonded to the ground

(the lower bottom surface of the base is constrained); the canopy, goaf shield, and the front and rear bars are defined as flexible using Hypermesh. The friction contact mode is adopted for the connection hinge joints to fully consider the dynamic behaviour (the friction coefficient is set as 0.3). The density, Young's modulus and Poisson's ratio of the structural parts is defined as  $7860 \text{ kg/m}^3$ ,  $2.1 \times 10^{11} \text{ Pa}$  and 0.3, respectively. The front and rear leg system are equivalently replaced using a spring-damper system; the stiffness of the legs are defined in Section 2.2. Based on the above definition, the numerical model of the four-leg support is finished, as shown in Fig. 2.

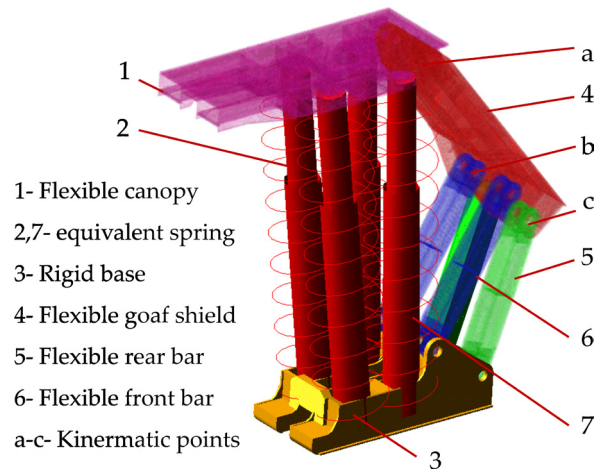


Fig. 2. Rigid-flexible coupling model of the four-leg support

### 1.2 Stiffness Definition of the Leg System

The leg system equipped with the support usually adopts a double-telescopic type hydraulic cylinder. Then it is reasonable to regard the leg system as a series-spring system, as shown in Fig. 3, where 1 is the mobile column, 2 is the enclosed liquid in the second level cylinder, 3 is the second level cylinder, 4 is the action sequence control valve, 5 is the enclosed liquid in the first level cylinder and 6 is the first level cylinder. At the initial time, the leg system rises and supports the direct roof under the action of the pump station ( $p_0$ ). Due to the existence of the action sequence control valve, the pressure of second level cylinder ( $p_2$ ) is significantly lower than that of the first level ( $p_1$ ), which leads to the variable stiffness of the leg system ( $p_2 \leq p_1 < p_0$ ).

This variation process can be divided into three stages. In the first stage, the roof pressure begins to appear ( $p$ ) since the support contact the direct roof. This pressure acting on the leg system is small at

this stage ( $p \leq p_2$ ), and the leg system basically has no displacement, and its stiffness ( $k$ ) is shown as infinite. As time goes on, the pressure acting on the leg increases with the roof settlement ( $p_2 \leq p < p_1$ ). Then the second level cylinder of the leg system starts to retract (the first level cylinder basically has no displacement), and the stiffness of the leg system is represented by the stiffness of the second level cylinder ( $k_2$ ). Finally, with the further settlement of the roof ( $p_1 \leq p$ ), the first and second level cylinders of the leg system will retract both. At this time, the support stiffness shows the series stiffness of the double-telescopic cylinders. Therefore, the stiffness of the leg system can be expressed as follows

$$k = \begin{cases} \infty & (p < p_2) \\ k_2 & (p_2 \leq p < p_1) \\ (k_1^{-1} + k_2^{-1})^{-1} & (p_1 \leq p < p_0) \end{cases} \quad (1)$$

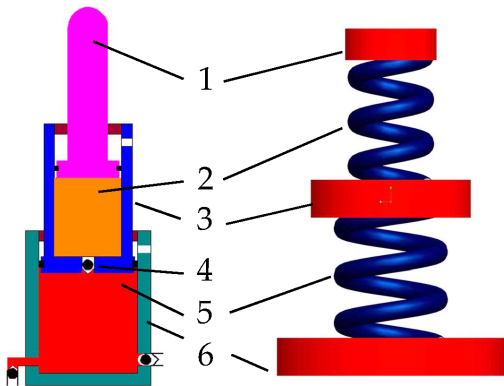


Fig. 3. Stiffness equivalent diagram of the leg system

In Eq. (1),  $k_1$  is the stiffness of the first level cylinder,  $p_0$  is the rated working resistance of column system. For a single-telescopic hydraulic cylinder, its stiffness  $k_s$  can be calculated using Eq. (2).

$$k_s = A\beta/l. \quad (2)$$

In Eq. (2),  $A$  is the effective bearing area of the cylinder,  $\beta$  is the Bulk Modulus of the enclosed liquid ( $1.95 \times 10^9$  Pa),  $l$  is the effective length of the enclosed liquid. Table 1 shows the main parameters of the legs on the ZZ 18000/33/72 type support. According to Eq. (2), the stiffness of the first level and second level of the front leg is  $12.5 \times 10^4$  kN/m and  $6.42 \times 10^4$  kN/m, the stiffness of the first level and second level of the rear leg is  $7.55 \times 10^4$  kN/m and  $3.95 \times 10^4$  kN/m.

Table 1. Main parameters of the legs

Cylinder parameter		Cylinder diameter [mm]	Rod diameter [mm]	Stroke [mm]
Front leg	First level	400	280	1956
	Second level	290	260	2006
Rear leg	First level	320	290	2076
	Second level	230	210	2052

After determining the stiffness of a single double-telescopic leg, a parallel bearing structure is formed between the front and rear legs, and the stiffness of the parallel bearing structure can be obtained using Eq. (3).

$$K_i = \sum_{m=1}^t k_{fm} + \sum_{n=1}^s k_{fn}. \quad (3)$$

In Eq. (3),  $K_i$  is the stiffness of the parallel bearing structure at working period  $i$ ,  $k_{fm}$  is the stiffness of the front leg  $m$ ,  $k_{fn}$  is the stiffness of the rear leg  $n$ ,  $t$  and  $s$  is the number of the front leg and rear leg, respectively ( $t = s = 2$ ). According to Eqs. (2) and (3), the stiffness of the four legs in the second stage and the third stage is 207,400 kN/m and 137,430 kN/m, respectively.

### 1.3 Static Loading Test

A static load test is carried out to test the validity and reliability of the established numerical model. A simulated roof that can move freely along the height direction of the support is arranged on the canopy. To reduce the influence of gravity, the simulated roof is slightly larger than the canopy, and the collision contact mode is set between the simulated roof and the canopy (as shown in Fig. 4). The static load is defined as 18,000 kN, and the loading time is 0.2 s to 1 s.

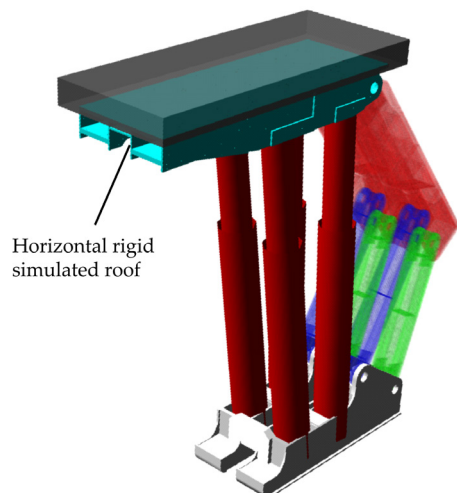


Fig. 4. Static loading test of the four-leg support

### 1.4 Dynamic Loading Test

Considering that the rated setting force of ZZ 18000/33/72 type support is 12,000 kN, two active static loads  $F_1$  and  $F_2$  are used to simulate the setting force during the impact loading test process. The active static load is applied on the symmetrical side near the centreline of the legs. The position of the impact load ( $F_c$  and  $F_g$ ) is selected from the canopy and the goaf shield at equal intervals (as shown in Fig. 5, points X1–X6 and Y1–Y6). The amplitude of the impact load is set to 500 kN and the loading time is 0.01 s ( $F_c = F_g = 500$  kN). When simulating different loading conditions, the impact load acting on the top beam and shield beam is successively applied to X1–X6 and Y1–Y6.

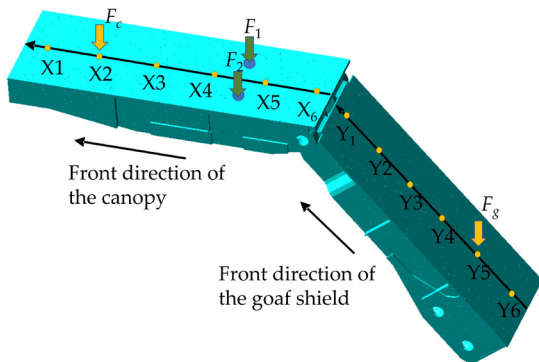


Fig. 5. Stiffness equivalent diagram of the leg system

## 2 RESULTS ANALYSIS AND DISCUSSION

### 2.1 Result Analysis of the Static Loading Test

Under this static load, the response results of the four-leg hydraulic support are shown in Fig. 6. As can be seen, the contact force increased to 18,220 kN in 1.12 s and then remained stable. The contact force is slightly higher than the applied active load, which is caused by the simulated roof gravity. From 0 s to 0.2 s is the self-weight balance period, the hydraulic support reaches the balance state under the gravity load of the canopy, and the length of the leg does not change. The distance between the upper and lower hinge joints of the front leg and the rear leg is 6302.00 mm and 6188.86 mm, respectively. From 0.2 s to 0.52 s is the active initial support (AIS) period; the second level cylinders of the front and rear legs reach the maximum value of this period under the impact force. The maximum AIS force of the front leg and the rear leg is 1313.9 kN and 2087.9 kN, respectively. During this period, since the external load is less than the AIS force of

the leg, the length of the leg shows no displacement. It can be noted from Fig. 6, the front leg retracts 0.07 mm and the rear leg retracts 0.12 mm in this period (Since ADAMS does not allow transient load, this displacement will never be 0). From 0.52 s to 0.71 s is the passive initial support (PIS) period; the second level cylinder of the leg system begins to retract with stiffness  $k_2$ . From 0.71 s to 1.00 s, the lengths of the front leg and rear leg decreases to 6272.7 mm and 6157.0 mm, respectively. The contact force between the roof and the canopy increases to 12,976 kN; the working resistances of the front and rear legs reaches the rated initial support force of 3956 kN and 2532 kN, respectively. The hydraulic support enters the rapid pressure rise (RPR) period. At this time, the first and second cylinder of the leg both retract. During this whole loading process, the front leg retracts 70.33 mm while the rear leg retracts 71.91 mm. Overall, the response of the numerical model meets the expected definition well.

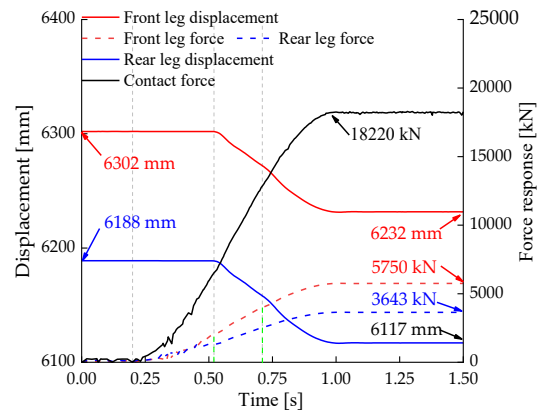


Fig. 6. Static response results of the support

Under this static load, the stiffness characteristic curve of the support is shown in Fig. 7. As can be seen, the hydraulic support model starts to show displacement (about 0.85 mm) in the AIS period. At this stage, the stiffness of the support is  $3.7e^8$  kN/m (near infinity). Then the support enters the PIS period and RPR period gradually, the average stiffness of the support during the two periods is 194,100 kN/m and 120,853 kN/m, respectively. Obviously, the stiffness of the support is less than the parallel stiffness of the four legs. This is due to the introduction of the hinge joints; the overall stiffness of the hydraulic support tends to decrease compared to the parallel stiffness of four legs. Furthermore, since the displacement stage stiffness of the front and rear legs is distributed at different time point (31.2 mm at the front leg and 33.0 mm at the rear leg), the support stiffness does not

show obvious step decrease characteristics but shows a three-stage stiffness distribution that decreases gradually.

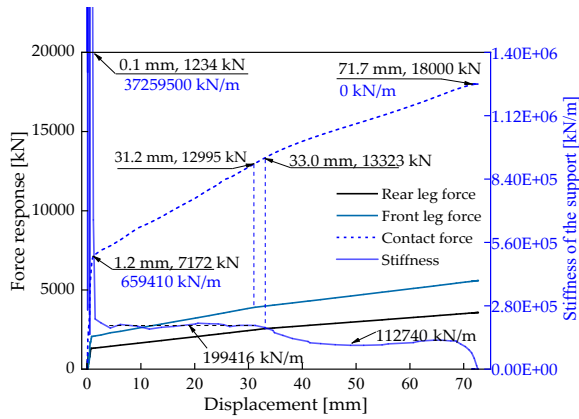


Fig. 7. Stiffness response results of the support

2.2 Dynamic Response of Hinge Joint a

When discussing the influence of impact load on the hydraulic support, to present the calculation results more clearly, X1–X6 (loading position of the canopy) and Y1–Y6 (loading position of the goaf shield) are defined as x-axis and y-axis coordinates to draw the force response surface of each hinge joint. While the dark yellow surface represents the steady-state response force of each hinge joint under the static load of 12,000 kN, the cyan surface represents the transient dynamic response force of each hinge joint when the canopy bears the impact load only, and the blue surface represents the transient dynamic response of each hinge joint when the goaf shield and canopy bear the impact load both. Meanwhile, in to describe the force response difference caused by the impact load clearer, the load variation coefficient  $\lambda$  is introduced to describe the load change rate at each hinge joint before and after impact load.

$$\lambda_z = (F_{Xq}^{Yqz} - F_{Xq}^z) / F_l, \quad 1 \leq q \leq 6, \quad (4)$$

where  $\lambda_z$  is the load variation coefficient of hinge joint  $z$ ,  $F_{Xq}^{Yqz}$  is the transient response force of hinge joint  $k$  when point  $Xq$  of canopy and point  $Yz$  of goaf shield bear the impact load both,  $F_{Xq}^z$  is the steady-state response force of hinge point  $k$ .

The dynamic force response results of hinge joint a are shown in Fig. 8. When the canopy only bears static load, since there is no equilibrium structure between the canopy and goad shield of the four-leg support [21], the canopy load cannot be transmitted to the goaf shield effectively. Therefore, the load act

at hinge joint a is rather small (basically stable at -92 kN). Then the impact load is applied to different positions of the canopy. The response force of hinge joint a decreases nearly linearly as the impact load moves along the canopy from the front end to back end, and the maximum load variation coefficient is about 5.04 %. The single canopy impact load has little influence on the hinge joint a (the slope of cyan surface in Fig. 8 is very small). When the canopy and goaf shield both bear the impact load, by observing the variation coefficient of the blue surface along any Y line, it can be noted that with the impact load of the goaf shield moving downward, the force variation coefficient of hinge joint a basically stabilizes at 5.04 %. That is, the introduction of goaf shield impact load does not influence the load variation coefficient formed by the canopy impact load. As the impact load moves forward to the front end of the canopy and goaf shield at the same time, the force variation coefficient of hinge joint a increases continuously. This load variation coefficient reaches the maximum value of 47.82 % when the impact load is applied at the front ends of both the canopy and goaf shield.

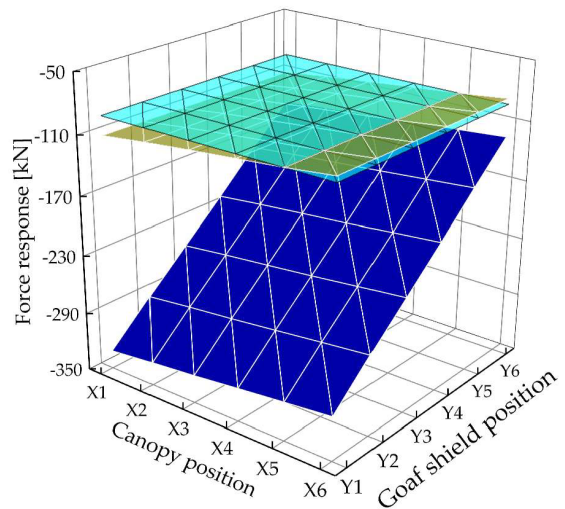


Fig. 8. Force response surface of hinge joint a

2.3 Dynamic Response of Hinge Joint b

The dynamic force response result of hinge joint b is shown in Fig. 9. When only the canopy bears static load, the force response of hinge joint b is stable at -3066 kN. This is much higher than that of hinge joint a, which means that the front bar bears a strong additional load at this time (the load does not come from the roof directly). Then the impact load is applied to the canopy only. As can be seen, the load

at hinge point b increases gradually with the forward movement of  $F_c$ , and the maximum load variation coefficient appears at the front end of the canopy (up to 61.81 %). When  $F_c$  and  $F_g$  are applied to the canopy and goaf shield both, the force response of hinge joint b increasing shows a gradually increasing pressure-relief characteristic as  $F_g$  moves downward. This pressure-relief effect reaches the peak value of -52.04 % when  $F_g$  is applied to the rear end of the goaf shield. By observing the variation coefficient of the blue surface along any  $Y$  line alone, it can be noted that the introduction of  $F_g$  does not significantly affect the variation coefficient that formed by  $F_c$  (basically stable at 52.02 %).

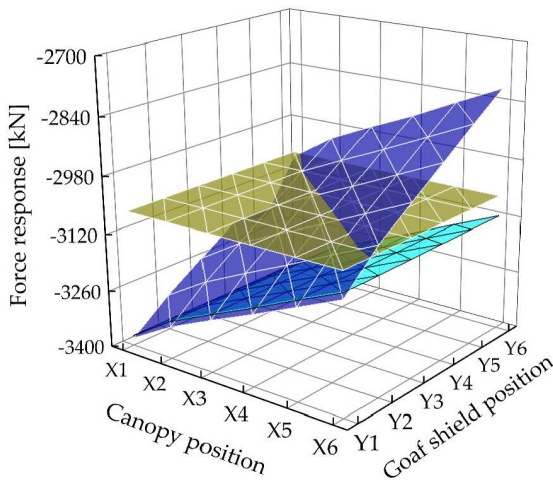


Fig. 9. Force response surface of hinge joint b

## 2.4 Dynamic Response of Hinge Joint c

Fig. 10 shows the force response of hinge joint c. When only the canopy bears the static load, the force response of hinge joint c also bears a large additional load. The force response of hinge joint c is basically stable at 3158 kN, and the force direction is opposite to that of hinge joint b. This additional load will continue to increase as the impact load of  $F_c$  appears and moves forward along the canopy (from 8.71 % to 65.6 %). When the canopy and goaf shield bear the impact load both and the  $F_g$  moves towards the rear end, the additional load at the rear bar shows a rapid attenuation trend. When  $F_g$  is applied to the rear end of the goaf shield, this attenuation trend reaches the maximum value of -95.56 %.

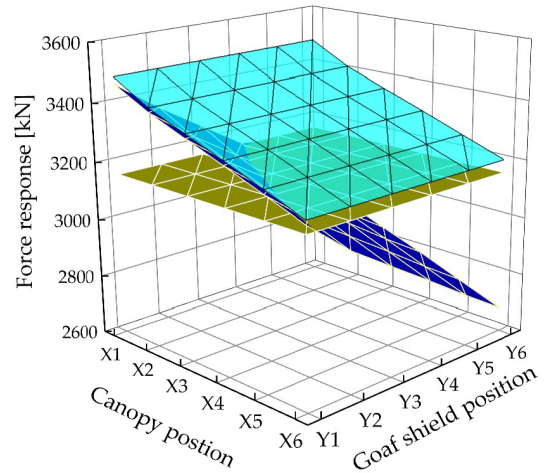
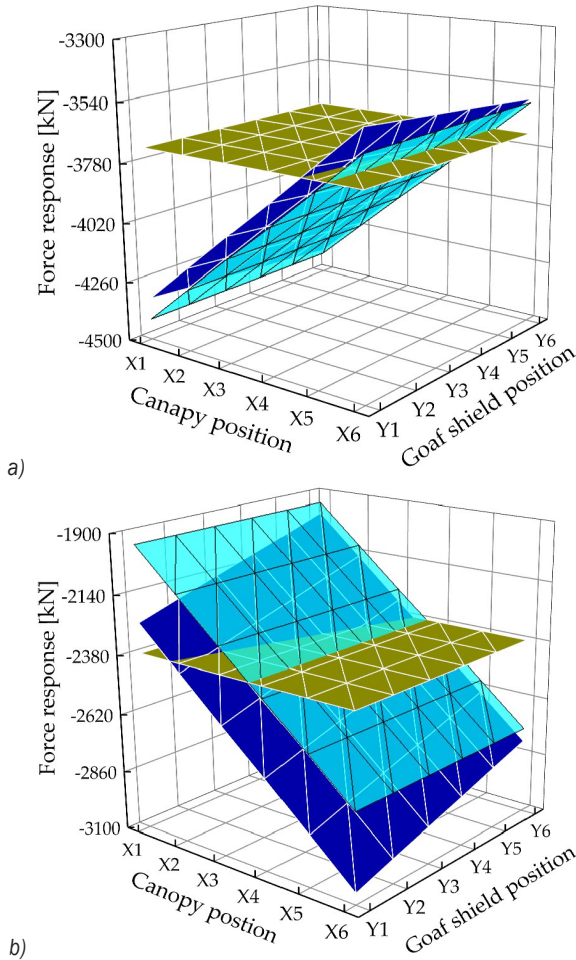


Fig. 10. Force response surface of hinge joint c

## 2.5 Dynamic Force Response of the Legs

The legs are the main bearing structural of the hydraulic support, so that most existing studies believe that the stiffness of the hydraulic support can be approximated to the bearing stiffness of the legs [21]. Therefore, it is of great significance to discuss the force response of the leg system to analyse the overall force transmission characteristics of the support. Fig. 11 shows the force response results of the front and rear legs when the impact load is applied to the support. It can be noted from the figure that when only the canopy bears the static load, the front and rear legs bear 3719.2 kN and 2373.1 kN, respectively. When  $F_c$  moves forward along the canopy direction, the front leg load increases first and then decreases gradually (ranges from 139.34 % to -25.10 %), while the rear leg load decreases first and then increases gradually (ranges from -85.86 % to 73.94 %). Under the action of impact load  $F_c$  on the front end of the canopy, the front leg shows a pressure-increasing trend while the rear leg shows a pressure-relief trend. When  $F_c$  and  $F_g$  are applied to the support both, the front leg releases part of the load and shows pressure-relief characteristics. The maximum load variation coefficient for the front leg is about -17.22 %. The rear leg shows a strong pressure-increasing effect, with the maximum load variation coefficient of 61.26 %, and the maximum load variation occurs at both the front end of the canopy and goaf shield. Obviously, the impact load  $F_g$  has a stronger influence on the rear leg load. Therefore, when the four-leg hydraulic support is in the front tilting bearing attitude, a backpressure structure can be placed at the tail end the goaf shield to improve the support performance of the rear leg.

Then the phenomenon of the rear leg pulling out can be prevented.



**Fig. 11.** Force response surface of the legs; a) front leg; and b) rear leg

### 2.6 Displacement Vibration Analysis of the Legs

When the support is subjected to the impact load, the support will produce large vibration due to the short duration time and severe load change characteristics of impact load. Therefore, the vibration characteristics of the front and rear leg system is discussed separately in this section when the impact load  $F_c$  is applied to the canopy of the support. During the leg vibration characteristic testing process, the 12,000 kN static load is also applied to the canopy firstly, then  $F_c$  is applied to the canopy at 1.5 s. The influence of the action position of  $F_c$  on the vibration characteristics of the leg system is observed, the results are shown in Fig. 12. When  $F_c$  is applied to the front end of the canopy, the displacement vibration effect of the front column

reaches the maximum value of 13.3 ‰ (the difference between the maximum vibration displacement and the stable displacement and then divided by the initial displacement). The maximum displacement amplitude is 81.72 mm. With the backward movement of  $F_c$ , the vibration effect gradually decreases to -1.43 ‰. As the impact load moves backward, the displacement vibration trend of the rear leg is opposite to that of the front leg (gradually increasing from -5.07 ‰ to 8.16 ‰). The maximum displacement amplitude of the rear leg is 50.14 mm. Obviously, the impact load  $F_c$  has a lower influence on the rear leg than that of the front leg.

### 3 CONCLUSIONS

To study the dynamic response of four-leg hydraulic support when the both canopy and goaf shield are subjected to the impacted, the rigid-flexible coupling numerical analysis model of the support is established. The spring-damper system is adopted to replace the leg system. By comparing and analysing the force response and vibration characteristics of the support under double-impact load at different positions, the load variation law of each hinge joint is obtained. The main conclusions are drawn as follows:

- (1) Compared with the two-leg hydraulic support, the sectional stiffness characteristics of the four-leg support are reflected in different bearing period during the bearing process. Therefore, the stiffness of the support shows a gradual three-stage distribution characteristic. Due to the introduction of the stiffness of the hinge joints, the overall stiffness of the four-support shows an attenuation trend relative to the two-leg support.
- (2) When the impact is only applied to the canopy, since there is no equilibrium structure between the canopy and goaf shield of the four-leg support, the dynamic load response of hinge joint b, hinge joint c, and the hinge joints of the legs to the impact load is significantly higher than that of the hinge point a. Among them, the load variation coefficient of the front leg is the most sensitive to the impact load  $F_c$  (up to 139.4 %).
- (3) When the canopy and goaf shield bear the impact load both, the hinge points of the support reach the peak response force (except the rear leg). With the backward movement of the impact load  $F_g$ , the force response of the hinge joints presents different pressure-relief characteristics, and the rear bar shows the strongest pressure-relief characteristics of 95.56 %. Meanwhile, the rear leg shows a strong pressure-rising effect

(the pressure-rising coefficient is about 61.26 %). Therefore, when the four-leg support forms a front-tilting bearing attitude, it is helpful to solve the problem of pulling out the rear leg by applying a certain backpressure at the tail end of the goaf shield.

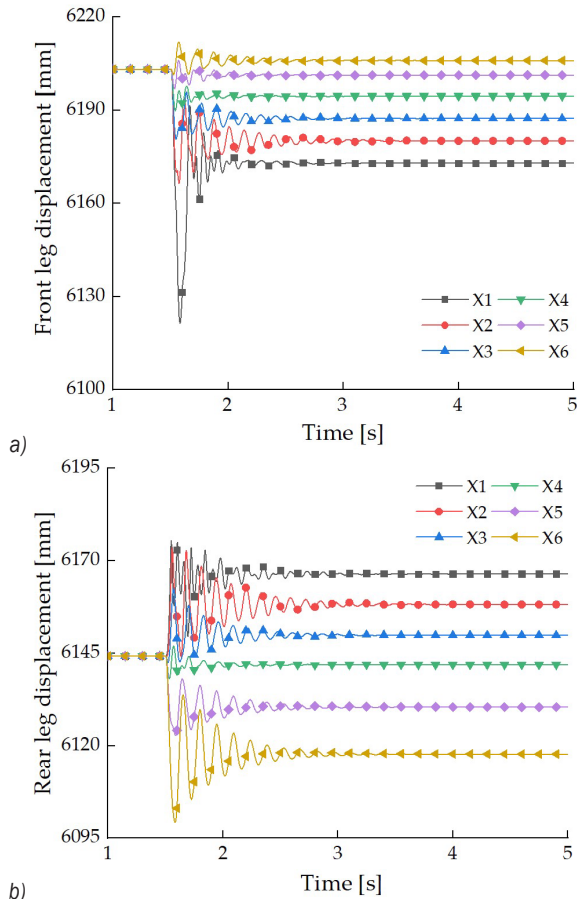


Fig. 12. Vibration response of the legs; a) front leg; and b) rear leg

(4) When the impact load  $F_c$  is applied to the front end of the canopy, the displacement vibration effect of the front leg reaches the strongest (the peak fluctuation reaches 13.3 %). With the backward movement of the impact load, the vibration effect decreases. The further the external impact load is from the leg, the longer stability time of the leg system takes.

#### 4 ACKNOWLEDGEMENTS

This research was funded by the National Natural Science Foundation of China (Grant Nos. 51974170 and 52104164), Natural Science Foundation of Shandong Province (Grant Nos. ZR2020QE103).

The authors are very grateful for the help of editors and reviewers.

#### 5 REFERENCES

- [1] BP Corporation. BP Energy Outlook 2020, from <https://www.bp.com>, accessed on 2021-04-18.
- [2] BP Corporation. Statistical Review of World Energy, from <https://www.bp.com>, accessed on 2021-04-18.
- [3] Jiang, K., Gao, K.D., Wan, L.R. (2020). Effect of gangue distributions on cutting force and specific energy in coal cutting. *Strojnikski vestnik - Journal of Mechanical Engineering*, vol. 66, no. 3, p. 203-212, DOI:10.5545/sv-jme.2019.6461.
- [4] Li, T.D., Wang, J.R., Zhang, K., Zhang, C.H. (2020). Mechanical analysis of the structure of longwall mining hydraulic support. *Science Progress*, vol. 103, no. 3, DOI:10.1177/0036850420936479.
- [5] Mark, C. (2016). Coal bursts in the deep longwall mines of the United States. *International Journal of Coal Science and Technology*, vol. 3, p. 1-9, DOI:10.1007/s40789-016-0102-9.
- [6] Xu, Q.W., Xu, K.L. (2021). Importance-based key basic event identification and evolution mechanism investigation of hydraulic support failure to protect employee health. *Sensors*, vol. 21, no. 21, art. ID 7240, DOI:10.3390/s21217240.
- [7] Ge, X., Xie, J.C., Wang, X.W., Liu, Y., Shi, H.B. (2020). A virtual adjustment method and experimental study of the support attitude of hydraulic support groups in propulsion state. *Measurement*, vol. 158, DOI:10.1016/j.measurement.2020.107743.
- [8] Zhao, G.C., Wang, H., Song, Y.N., Zhang, C.S. (2020). Dynamic characteristics study on the two-stage safety valve used on hydraulic support under impact loading. *Journal of Theoretical and Applied Mechanics*, vol. 58, no. 3, p. 623-635, DOI:10.15632/jtam-pl/116576.
- [9] Wan, L.R., Wang, J.T., Zeng, Q.L., Ma, D.J., Yu, X.H., Meng, Z.S. (2022). Vibration response analysis of the tail beam of hydraulic support impacted by coal gangue particles with different shapes. *ACS Omega*, vol. 7, no. 4, p. 3656-3670, DOI:10.1021/acsomega.1c06279.
- [10] Wang, J.C., Wang, Z.H., Tang, Y.S., Li, M., Chang, K.L., Gong, H., Xu, G.L. (2021). Experimental study on mining-induced dynamic impact effect of main roof in deeply buried thick coal seams with weakly consolidated thin bed rock. *Chinese Journal of Rock Mechanics and Engineering*, vol. 40, no. 12, p. 2377-2391, DOI:10.13722/j.cnki.jrme.2021.0340. (in Chinese)
- [11] Yang, S.L., Wang, J.C., Yang, J.H. (2017). Physical analog simulation analysis and its mechanical explanation on dynamic load impact. *Journal of China Coal Society*, vol. 42, no. 2, p. 335-343, DOI:10.13225/j.cnki.jccs.2016.6004. (in Chinese)
- [12] Li, C., Yin, X.G., Xie, J., Peng, G.Y. (2019). The characteristics of mining induced stress fluctuations in broken rock mass over one kilometer deep coal mine. *Thermal Science*, vol. 23, p. 843-851, DOI:10.2298/TSCI180621119L.
- [13] Tan, Y.L., Liu, X.S., Shen, B.T., Ning, J.G., Gu, Q.H. (2018). New approaches to testing and evaluating the impact capability of coal seam with hard roof and/or floor in coal mines.

- Geomechanics and Engineering*, vol. 14, no. 4, p. 367-376, DOI:10.12989/gae.2018.14.4.367.
- [14] Singh, G.S.P., Singh, U.K. (2009). A numerical modeling approach for assessment of progressive caving of strata and performance of hydraulic powered support in longwall workings. *Computers and Geotechnics*, vol. 36, no. 7, p. 1142-1156, DOI:10.1016/j.compgeo.2009.05.001.
- [15] Singh, G.S.P., Singh, U.K. (2010). Prediction of caving behavior of strata and optimum rating of hydraulic powered support for longwall workings. *International Journal of Rock Mechanics and Mining Sciences*, vol. 47, no. 1, p. 1-16, DOI:10.1016/j.ijrmms.2009.09.001.
- [16] Verma, A.K. (2013). Numerical analysis of an interaction between hydraulic-powered support and surrounding rock strata. *International Journal of Geomechanics*, vol. 13, no. 2, p. 181-192, DOI:10.1061/(ASCE)GM.1943-5622.0000190.
- [17] Rajwa, S., Janoszek, T., Prusek, S. (2020). Model tests of the effect of active roof support on the working stability of a longwall. *Computers and Geotechnics*, vol. 118, no. 103302, DOI:10.1016/j.compgeo.2019.103302.
- [18] Witek M., Prusek S. (2016). Numerical calculations of shield support stress based on laboratory test results. *Computers and Geotechnics*, vol. 72, no. 74-88, DOI:10.1016/j.compgeo.2015.11.007.
- [19] Lin, J.Z., Yang, T.R., Ni, K.X., Han, C.Y., Ma, H., Gao, A., Xiao, C.L. (2021). Effects of boundary conditions on stress distribution of hydraulic support: A simulation and experimental study. *Advances in Mechanical Engineering*, vol. 13, no. 3, DOI:10.1177/16878140211001194.
- [20] Wang, G.F., Zhao, Z.L. (2010). Dynamic analysis of double-telescopic prop against shocking in powered support. *Journal of Mining and Strata Control Engineering*, vol. 15, no. 2, p. 62-65+40, DOI:10.13532/j.cnki.cn11-3677/td.2010.02.009.
- [21] Liang, L.C., Ren, H.W., Zheng, H. (2018). Analysis on mechanical-hydraulic coupling rigidity characteristics of hydraulic powered support. *Coal Science and Technology*, vol. 46, no. 3, p. 141-147, DOI:10.13225/j.cnki.jccs.2015.7021. (In Chinese)
- [22] Meng, Z.S., Zeng, Q.L., Gao, K.D., Kong, S., Liu, P., Wan, L.R. (2018). Failure analysis of super-large mining height powered support. *Engineering Failure Analysis*, vol. 92, p. 378-391, DOI:10.1016/j.engfailanal.2018.04.011.
- [23] Meng Z.S., Zeng, Q.L., Wan, L.R., Wang, C.L. (2018). Supporting performance and canopy adaptability of shield support. *Journal of China Coal Society*, vol. 43, no. 4, p. 1162-1170, DOI:10.13225/j.cnki.jccs.2017.1403. (In Chinese)
- [24] Xie, Y.Y., Meng, Z.S., Zeng, Q.L., Yang, C.X., Gao, K.D. (2020). Analysis of distribution characteristics of study on floor specific pressure of hydraulic support for deep mining based on impact load. *Journal of China Coal Society*, vol. 45, no. 3, p. 982-989, DOI:10.13225/j.cnki.jccs.SJ19.1541. (In Chinese)
- [25] Wan, L.R., Zhang, S., Meng, Z.S., Xie, Y.Y. (2021). Analysis of the protection performance of face guard for large mining height hydraulic support. *Shock and Vibration*, vol. 2021, art. ID 6631017, DOI:10.1155/2021/6631017.
- [26] Zeng, Q.L., Li, Y.Y., Yang, Y. (2021). Dynamic analysis of hydraulic support with single clearance. *Strojniški vestnik - Journal of Mechanical Engineering*, vol. 67, no. 1-2, p. 53-66, DOI:10.5545/sv-jme.2020.6998.
- [27] Hu, X.P. (2020). Cooperative automatic control for the canopy posture of a four-leg hydraulic support. *International Journal of Simulation Modelling*, vol. 19, no. 4, p. 713-724, DOI:10.2507/IJSIMM19-4-C020.
- [28] Ren, H.W., Zhang, D.S., Gong, S.X., Zhou, K., Xi, C.Y., He, M., Li, T.J. (2021). Dynamic impact experiment and response characteristics analysis for 1:2 reduced-scale model of hydraulic support. *International Journal of Mining Science and Technology*, vol. 31, no. 3, p. 347-356, DOI:10.1016/j.ijmst.2021.03.004.
- [29] Wang, D.L., Zeng, X.T., Wang, G.F., Li, R. (2022). Adaptability analysis of four-leg hydraulic support with large mining height under impact dynamic load. *Shock and Vibration*, vol. 2022, p. 1-16, DOI:10.1155/2022/2168871.

# Enhancing the Performance of a Vapour Compression Refrigerator System Using R134a with a CuO/CeO<sub>2</sub> Nano-refrigerant

HudaEIslam Mohamed<sup>1,\*</sup> – Unal Camdali<sup>1</sup> – Atilla Biyikoglu<sup>2</sup> – Metin Actas<sup>3</sup>

<sup>1</sup>Ankara Yildirim Beyazit University, Department of Mechanical Engineering, Turkey

<sup>2</sup>Gazi University, Department of Mechanical Engineering, Turkey

<sup>3</sup>Ankara Yildirim Beyazit University, Department of Energy, Turkey

Most studies report that dispersing nanoparticles into refrigerants and lubricating oils leads to performance improvements in refrigeration systems, due to improvements in the thermal physics properties of a pure refrigerant, which leads to reduced energy consumption. Using nanoparticles in a refrigeration system is associated with many difficulties, such as the cost of preparing and obtaining a stable and homogeneous mixture with less agglomeration and sedimentation. Most current studies focus on the use of metals, metal oxides, and a hybrid of oxides as nanoparticles in refrigeration systems. In this research, nanoparticles were prepared in an inexpensive and easy way as a single oxide and as a mixture consisting of copper and cerium oxides. The results of nanoparticle preparation using X-ray diffraction and scanning electron microscopy prove that the particles of the samples were spherical in shape, with suitable average diameters ranging from 78.95 nm, 79.9 nm, 44.15 nm and 63.3 nm for copper oxide, cerium oxide, the first mixture, and the second mixture, respectively. Cerium oxide has not been used in a refrigeration system; this study preferred the implementation of a theoretical study using Ansys Fluent software to verify the possibility of improving the performance of the refrigeration system. The results confirmed that copper oxide enhanced the coefficient of performance of the refrigeration system by 25 %, and cerium oxide succeeded in improving the performance of the system by a lesser value. The mixture containing a higher percentage of copper oxide yielded better results.

**Keywords:** vapour compression refrigeration system, coefficient of performance, nano-refrigerant, nanoparticles

## Highlights

- The performance vapour compression refrigeration system that works using R134a was studied experimentally and theoretically as a first step without nanoparticles, and the agreement between the experimental and theoretical results was close to 98 %.
- This study provided an inexpensive method for preparing nanoparticles using distilled water, ammonia, copper nitrate, and cerium nitrate.
- Nanoparticles were prepared as follows: CuO, CeO<sub>2</sub>; Mixture 1 consisted of 50 % CuO + 50 % CeO<sub>2</sub>; Mixture 2 consisted of 60 % CuO + 40 % CeO<sub>2</sub>; Mixture 3 consisted of 70 % CuO + 30 % CeO<sub>2</sub>; Mixture 4 consisted of 40 % CuO + 60 % CeO<sub>2</sub>; Mixture 5 consisted of 30 % CuO + 70 % CeO<sub>2</sub>.
- The concept of nanoparticles as a mixture can improve the performance of refrigeration systems.

## 0 INTRODUCTION

The world is facing a major challenge in the energy sector, due to its diminishing resources and a large increase in energy consumption, especially in refrigeration and air conditioners. Various studies have improved the efficiency of thermal systems. This can be accomplished in two ways: first by improving the design of the heat exchanger to include three shell and tube type, plate type, microchannel, and so on, and second by using new kinds of working fluids [1]. In 1873, Maxwell dispersed particles ranging in diameter from millimetres to micrometres into a pure to enhance the thermophysical properties of the fluid; however, this attempt encountered several problems including stability, clogging, and erosion. [2] to [4]. Nanofluids have attracted the attention of many

researchers in various scientific fields in recent years. Researchers used a new concept of working fluids known as “nanofluids” for the first time, which contain particles of less than 100 nm, called “nanoparticles”, to improve the heat transfer characteristics of various fluids. Recently, the concept of nanofluids has been developed to include refrigerants [2] to [4]. A nanofluid is divided into three categories depending on the composition of nanoparticles: (i) mono-nanofluids, which consist of similar nanoparticles, (ii) hybrid nanofluids, which consist of dissimilar nanoparticles, and (iii) hybrid nanofluids, which consist of composite nanoparticles [1]. Four conditions are required for the successful preparation of the nanofluid: (i) the dispersibility of nanoparticles, (ii) the stability of nanoparticles, (iii) the chemical compatibility of nanoparticles, and (iv) the thermal stability of

\*Corr. Author's Address: Ankara Yildirim Beyazit University, Department of Mechanical Engineering, Turkey, hudaabdali973@gmail.com

nanofluids. These conditions will create a nanofluid that has the best heat transfer properties between solid particles and fluids [5]. Practically, there are two methods to prepare the nano-refrigerants: a one-step method and a two-step method. The two-step method is commonly used for preparing nano-refrigerants, in which the nanoparticles are manufactured as a powder and then added to the base fluid, followed by several types of dispersion methods, such as agitation either by ultrasonic or magnetic force, homogenizing, and high shear mixing to disperse nanoparticles inside a mixture. The one-step method is based on condensing vapour nanophase powders into liquid by reducing the pressure and then dissolving them inside the liquid immediately [6].

The literature review is classified into two sections. The first evaluates the performance of the vapour compression refrigeration system based on nano-refrigerant and nano-lubricant, and the second evaluates the basic properties of nano-refrigerant and nano-lubricant such as thermal conductivity, viscosity, specific heat, and density. Vijayakumar et al. [7] evaluated the performance of refrigerators based on nano-lubricants consisting of an aluminium dioxide added to polyol ester oil, and 60 g of R602a was used as a refrigerant. The results showed that the refrigerating effect increased by 6.09 %, the compressor work decreased by 15.78 %, and the coefficient of performance (COP) increased by 20.09 %. Choi et al. [8] evaluated the performance of refrigerators based on nano-lubricants consisting of 0.1 wt.% multi-walled carbon nanotubes (MWCNTs) that were dispersed into the polyol ester oil, and R134a was charged as a refrigerant. The results showed that the power consumption of the compressor decreased by 17 %. Senthilkumar et al. [9] evaluated the performance of a refrigeration system based on nano-lubricants consisting of  $\text{Al}_2\text{O}_3$  and  $\text{SiO}_2$  hybrid nanoparticles at two different concentrations of 0.4 g/l and 0.6 g/l; 40 g and 60 g of R600a were charged as a refrigerant. The results indicated that COP and the refrigerating effect increased by 30 % and 25 % respectively, while the power consumption decreased by 80 W. Senthilkumar et al. [10] evaluated the performance of a vapour compression refrigeration system based on hybrid nano-lubricants consisting of CuO and  $\text{SiO}_2$  at 0.2 g/l and 0.4 g/l concentrations, and 40 g and 60 g of R600a were charged as a refrigerant. The results indicated that the COP improved by 35 % and refrigeration effects by 18 % while the power consumption decreased by 75 W. Senthilkumar and Anderson [11] evaluated the performance of a refrigeration system based on nano-

lubricants consisting of 0 g/l, 0.2 g/l, 0.4 g/l, and 0.6 g/l  $\text{SiO}_2$  mixed with polyol ester oil; 30 g, 40 g, 50 g, 60 g and 70 g of R410A were used as refrigerants. The results indicated that 0.4 g/l  $\text{SiO}_2$  and 40 g refrigerant achieved a high refrigeration effect, decreased compressor work by 80 W, and enhanced COP by 1.7. Senthilkumar et al. [12] evaluated the performance of a refrigeration system based on hybrid nano-lubricants consisting of 0.4 g/l  $\text{ZnO}/\text{SiO}_2$  with 40 g R600a and 0.6 g/l  $\text{ZnO}/\text{SiO}_2$  with 60 g R600a. The results indicated that 0.6 g/l  $\text{ZnO}/\text{SiO}_2$  achieved a high refrigeration effect of 180 W, and enhanced COP by 1.7, while the lower compressor work was 78 W. Senthilkumar et al. [13] evaluated the performance of a vapour compression refrigeration system based on hybrid nano-lubricants consisting of 0.2 g/l, 0.4 g/l and 0.6 g/l  $\text{CuO}/\text{Al}_2\text{O}_3$ , and 70 g of R600a was used as a refrigerant. The results showed that the addition of  $\text{CuO}/\text{Al}_2\text{O}_3$  enhanced COP by 27 % and increased the refrigeration capacity by 20 % while reducing the power consumption by 24 %. Javadi and Saidur [14] evaluated the performance of refrigerators based on nano-lubricants consisting of 0.1 wt.%  $\text{Al}_2\text{O}_3$ . The results indicated that 0.1 wt.%  $\text{Al}_2\text{O}_3$  decreased the power consumption by 2.69 %. Gill et al. [15] evaluated the performance of a domestic refrigerator based on nano-lubricants consisting of 0.2 g/l, 0.4 g/l, and 0.6 g/l  $\text{TiO}_2$  added to Capella D oil as an alternative to R134a. Various charges of liquefied petroleum gas from 40 g to 70 g were used as refrigerants. The results indicated that the refrigeration effect and COP were higher than R134a by approximately 18.74 % to 32.72 % and 10.15 % to 61.49 %, respectively. In addition, the compressor power input was lower than R134a by approximately 3.20 to 18.1. Additionally, the results reported that 40 g liquefied petroleum gas refrigerant with 0.4 g/l  $\text{TiO}_2$  achieved the best energy performance of the refrigerator. Karthick et al. [16] evaluated the performance of a vapor compression refrigeration system based on four samples of nano-lubricant: Sample 1 (mineral oil + 0.02 vol.%  $\text{Al}_2\text{O}_3$  + 0.01 vol.%  $\text{TiO}_2$ ), Sample 2 (mineral oil + 0.01 vol.%  $\text{Al}_2\text{O}_3$  + 0.005 vol.%  $\text{TiO}_2$ ), Sample 3 (mineral oil + 0.05 vol.%  $\text{Al}_2\text{O}_3$ ), and Sample 4 (mineral oil + 0.02 vol.%  $\text{Al}_2\text{O}_3$  + 0.02 vol.%  $\text{ZnO}$ ), and R600a was charged as a refrigerant. The results indicated that COP improved by 14.61 %. All nano-lubricants exhibited a higher COP, which reduces the power consumption. Adelekan et al. [17] Investigated the performance of a domestic refrigerator based on nano-lubricants consisting of 0.2 g/l, 0.4 g/l, and 0.6 g/l  $\text{TiO}_2$ . The safe mass charge of liquefied petroleum gas

was charged as a refrigerant. The results showed that all various concentrations of nanoparticles achieved a reduction in power consumption by 14 %, 9 %, and 8 %, respectively. Mineral oil achieved the highest power consumption whereas 0.2 g/l TiO<sub>2</sub> achieved the lowest. The refrigeration effects based on 0.4 g/l and 0.6 g/l were higher, while those based on 0.2 g/l were lower. Subhedar et al. [18] evaluated the performance of a vapour compression refrigeration system based on nano-lubricants consisting of 0.05 vol.%, 0.075 vol.%, 0.1 vol.%, and 0.2 vol.% Al<sub>2</sub>O<sub>3</sub> mixed with mineral oil, and R134a was charged as a refrigerant. The results indicated that 0.075 vol.% achieved the maximum enhancement in COP of approximately 85 % and saved approximately 27 % compressor power. Additionally, it was reported that 0.075 vol.% was the best concentration. Babarinde et al. [19] investigated the performance of a refrigerator based on nano-lubricants consisting of 0.4 g/l and 0.6 g/l TiO<sub>2</sub> mixed with mineral oil, and R600a was used as a refrigerant as an alternative to R134a. The results indicated that 0.4 g/L TiO<sub>2</sub> achieved the highest COP and lowest power consumption. Selimefendigil and Bingölbali [20] evaluated the performance of a vapour compression refrigeration system based on nano-lubricants consisting of 0.5 vol.%, 0.7 vol.%, 0.8 vol.%, and 1 vol.% TiO<sub>2</sub> mixed with poly alkylene glycol oil, and R134a was used as a refrigerant. The results indicated that 0.5 vol.%, 0.8 vol.%, and 1 vol.% achieved improvements of COP of approximately 1.43 %, 15.72 %, and 21.42 %, respectively; 1 vol % reduced energy consumption by 15 %. Sundararaj and Manivannan [21] investigated the performance of a vapour compression refrigeration system based on nano-lubricants consisting of 0.1 vol. % Au, 0.2 vol.% Au, 0.1 vol.% HAuCl<sub>4</sub>, 0.2 vol.% HAuCl<sub>4</sub>, 0.1 vol.% Au and 0.05 vol.% carbon nanotubes (CNT), 0.2 vol.% Au, and 0.02 vol.% of CNT added to poly alkylene glycol oil, and R134a was used as a refrigerant. The results indicated that 0.2 vol.% Au and 0.02 vol.% CNT achieved the lowest power input compared to other compositions, the greatest cooling capacity, and the maximum value of COP. Therefore, it is preferred to run the system using 0.2 vol.% Au and 0.02 vol.% of CNT as volume fractions. Peyyala et al. [22] investigated the performance of a vapor compression refrigeration system based on nano-lubricants consisting of 0.1 vol.% to 0.2 vol.% Al<sub>2</sub>O<sub>3</sub> mixed with mineral oil, and R410a was used as a refrigerant. The results indicated an increase in the COP value with increasing nanoparticle concentrations, and the maximum value was observed at 0.2 vol.% Al<sub>2</sub>O<sub>3</sub>. Babarinde et al. [23]

investigated the performance of a vapor compression refrigeration system based on nano-lubricants consisting of 0.2 g/l, 0.4 g/l, and 0.6 g/l graphene added to mineral oil, and 50 g to 70 g of R600a which were used as a refrigerant. The results indicated that the nano-lubricant based on 60 g of R600a and 0.2 g/l graphene exhibited the lowest power consumption, and the highest COP. Adelekan et al. [24] evaluated the performance of a domestic refrigerator based on nano-lubricants consisting of 0.1 g/l, 0.3 g/l, and 0.5 g/l TiO<sub>2</sub>, mixed with mineral oil, and 40 g, 60 g, and 80 g of R600a were used as refrigerants. The results showed that the highest COP and refrigerating effects were 4.99 kJ/kg and 290.83 kJ/kg based on 40 g 0.1g/l nano-lubricant. Ajayi et al. [25] evaluated the performance of a vapor compression refrigeration system based on 0.5 g/l Al<sub>2</sub>O<sub>3</sub> mixed with Capella D oil, and 100 g of R134a was used as a refrigerant. The results showed that nano-lubricants achieved a higher refrigeration effect, better performance, and improved energy consumption. Senthilkumar and Anderson [26] evaluated the performance of a vapor compression refrigeration system, based on nano-lubricants consisting of 0.2 g/l, 0.4 g/l, and 0.6 g/l SiO<sub>2</sub>, added to polyol ester oil, and 30 g, 40 g, 50 g, 60 g and 70 g R410A were used as refrigerants. The results indicated that 40 g of R410A and 0.4 g/l of SiO<sub>2</sub> achieved better refrigerating effects and reduced power consumption. This leads to an enhanced COP. Pawale et al. [27] evaluated the performance of a vapor compression refrigeration system based on nano-refrigerant consisting of 0.5 wt.%, and 0.1 wt.% Al<sub>2</sub>O<sub>3</sub>, and a particle size diameter of 50 nm was dispersed into R134a. The results showed that 0.5 wt.% improved the performance; however, the increase in nanoparticle concentration will lead to a decrease the performance of the system. Kumar et al. [28] evaluated the performance of a vapor compression refrigeration system based on nano-refrigerant consisting of (1 g of ZnO / 1 g SiO<sub>2</sub>), (1.5 g of ZnO / 0.5 g of SiO<sub>2</sub>), and (0.5 g of ZnO / 1.5 g of SiO<sub>2</sub>) dispersed into 0.5 kg of R134a. The results showed that COP increased approximately 26 %. Manikandan and Avinash [29] investigated the performance of domestic refrigerators based on nano-refrigerants consisting of CuO, pure nano-CuO, and Ag-doped nano-CuO dispersed into R290. The results indicated that Ag-doped nano-CuO achieved the best performance of the system compared to pure nano-CuO. The COP of Ag-doped nano-CuO increased up to 29 %, while the power consumption of a system reduced up to 28 %. Kundan and Singh [30] evaluated the performance of a vapour compression refrigeration system based on nano-refrigerant

consisting of 0.5 wt.% to 1 wt.%  $\text{Al}_2\text{O}_3$  dispersed into R134a, with a particle size diameter of 20 nm. The results based on volume flow rates of refrigerants showed that 6.5 l/h and 11 l/h achieved improvements of COP from 7.20 % to 16.34 % respectively at 0.5 wt.%  $\text{Al}_2\text{O}_3$ ; however, 1 wt.%  $\text{Al}_2\text{O}_3$  caused a reduction in COP at the same volume flow rates. Nagaraju and Reddy [31] evaluated the performance of a vapour compression refrigeration system based on nano-refrigerants consisting of 0.05 wt.% to 0.8 wt.% CuO particle sizes ranging from 10 nm to 70 nm dispersed into R134a. The results showed that 0.8 wt.% of CuO was the optimal concentration that achieved the highest heat transfer enhancement, enhanced COP, and reduced power consumption. Kumar and Tiwari [32] evaluated the performance of a vapor compression refrigeration system based on R134a / poly alkylene glycol oil, R600a / poly alkylene glycol oil and Cu nanoparticles dispersed into R600a. The results showed that R600a achieved a higher COP and refrigeration effect of approximately 27.12 % and 25 % respectively, while the reduction in power consumption was 1.69 % which was less than that of R134a. Moreover, dispersing 0.5 wt.%, 1 wt.%, and 1.5 wt.% Cu into R600a improved the COP and refrigeration effect compared to pure R600a, and reduced power consumption. Kumar et al. [33] investigated the performance of a vapour compression refrigeration system based on 0.01 vol.% and 0.06 vol.%  $\text{ZrO}_2$ , and a particle size diameter of 20 nm was dispersed into both R134a and R152a. The results indicated an improvement in COP of 33.45 % based on the 0.06 vol.%  $\text{ZrO}_2$ -R152a nano-refrigerant. The application of R152a as a refrigerant was environmentally beneficial due to its properties such as zero ozone depletion potential and very low global warming potential. Mahdi et al. [34] evaluated the performance of a vapour compression refrigeration system based on a nano-refrigerant consisting of 0.01 vol.% and 0.02 vol.%  $\text{Al}_2\text{O}_3$ , and a diameter of 20 nm to 30 nm was dispersed into R134a. The results showed that the rising nanoparticle concentration caused the improvement of COP by 3.33 % to 12 %, respectively, and the reduction of power consumption was nearly 1.6 % and 3.3 %, respectively. Singh [35] evaluated the performance of a vapor compression refrigeration system based on 0.2 vol. %, 0.4 vol. %, and 0.6 vol. %  $\text{TiO}_2$ , and a particle size diameter of 30 nm to 50 nm was dispersed into R134a. The results showed that the nano-refrigerant based on 0.4 vol.% of  $\text{TiO}_2$  achieved an improvement of COP of by approximately 11.1 % at 20 °C, 25 °C, and 30 °C evaporator temperatures. Additionally, an increase or

decrease in power consumption has not been observed, which shows that nanoparticles were completely dissolved in the refrigerant.

Thermal conductivity is the most important of the thermophysical properties of nano-refrigerants due to its effects on the boiling and convective heat transfer coefficients. This explains why most researchers focus on studying thermal conductivity. Recently, interest in the study of viscosity has begun to appear to extend to other thermophysical properties to form a clear idea of the heat transfer properties [4]. Kedzierski et al [36] evaluated the thermophysical properties of nano-lubricants based on nanoparticle size diameters of 127 nm and 135 nm of  $\text{Al}_2\text{O}_3$  and ZnO respectively mixed with polyol ester oil at atmospheric pressure with temperatures ranging from 288 K to 318 K, and various mass fractions of  $\text{Al}_2\text{O}_3$ , and ZnO were used. The results showed that increasing nanoparticle concentrations led to increased viscosity, density, and thermal conductivity but decreased viscosity and density with increased temperature. Sanukrishna and Prakash [37] evaluated the thermal conductivity and viscosity of nano-lubricants based on 0.07 vol.% to 0.8 vol.%  $\text{TiO}_2$  mixed with poly alkylene glycol oil at temperatures ranging from 20 °C to 90 °C. They found that increasing nanoparticle concentrations led to increasing these parameters; in contrast, they decreased with increasing temperature. Zawawi et al. [38] evaluated the thermal conductivity and dynamic viscosity of nano-lubricants based on 0.02 vol.% to 0.1 vol.%  $\text{Al}_2\text{O}_3/\text{SiO}_2$ ,  $\text{Al}_2\text{O}_3/\text{TiO}_2$ , and  $\text{TiO}_2/\text{SiO}_2$  mixed with poly alkylene glycol oil I at temperatures ranging from 303 K to 353 K. The results showed that 0.1 vol. %  $\text{Al}_2\text{O}_3/\text{TiO}_2$  poly alkylene glycol oil enhanced the viscosity by 20.50 % at 303 K, while 0.1 vol. %  $\text{Al}_2\text{O}_3 / \text{SiO}_2$  poly alkylene glycol oil improved the thermal conductivity by 2.41 % at 303 K.

As per previous studies the addition of nanoparticles into the refrigerant or lubricant oil in a vapour compression refrigeration system was conducted to improve the COP and thermophysical properties of the fluid as a metal, metal oxide, and hybrid nanoparticles. This research presents a new concept of nanoparticles as a single oxide and as a mixture that was prepared an inexpensive and easy way using, distilled water, ammonia, copper nitrate, and cerium nitrate. The nanoparticles were prepared as follows: CuO,  $\text{CeO}_2$ : Mixture 1 consisted of 50 % CuO + 50 %  $\text{CeO}_2$ ; Mixture 2 consisted of 60 % CuO + 40 %  $\text{CeO}_2$ ; Mixture 3 consisted of 70 % CuO + 30 %  $\text{CeO}_2$ ; Mixture 4 consisted of 40 % CuO + 60 %  $\text{CeO}_2$ ; and Mixture 5 consisted of 30 % CuO + 70

% CeO<sub>2</sub>. The application of nanoparticles in a vapour compression refrigeration system is challenging due to factors such as high cost, instability, and agglomeration. Fortunately, the method of preparation used in this research used materials from which nanoparticles are prepared can be commonly found in all chemistry laboratories. Therefore, the cost barrier, which is one of the major obstacles to using nanoparticles, is broken. Consequently, the desired increases in the thermal conductivity achieved by these nano particles can be obtained at a reasonably affordable cost.

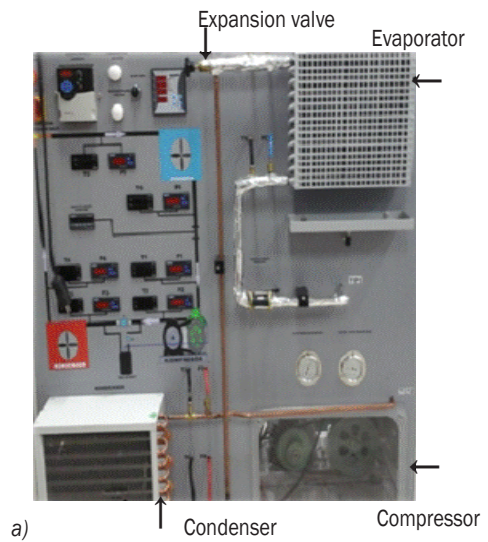
1 MATERIALS AND METHODS

This section is divided into three parts. In the first part, an experiment was conducted on a vapour compression refrigeration system using R134a as a refrigerant and SUNISO as a mineral oil of a compressor, and the coefficient of performance was calculated based on the change in the enthalpy of the refrigerant. Thereafter, Ansys Fluent software version 19.0 was used to calculate the coefficient of performance theoretically to make a comparative study between an experiment and theoretical results. In the second part, seven types of nanoparticles were prepared, and the preparation process will be explained in detail later, Finally, in the third part, the nanoparticles were added to the refrigeration system to verify their effect on the COP of the system.

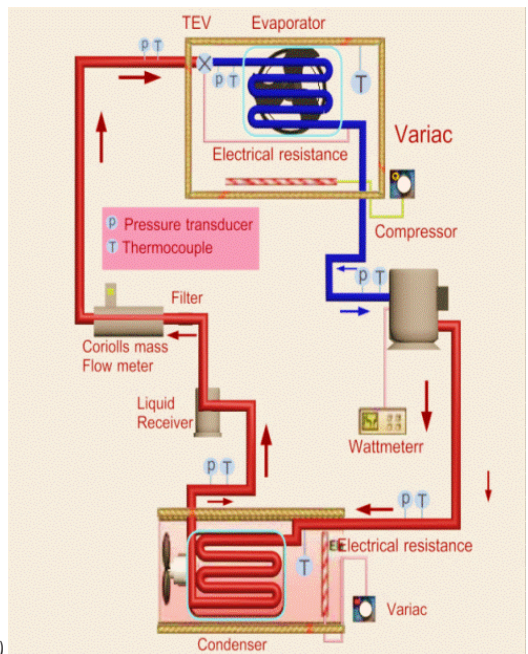
1.1 Experimental Work

An experiment was carried out in a laboratory under normal conditions at Yildiz Technical University in Istanbul, Turkey. The system was charged with refrigerant R134a and compressor oil. Digital meters were used to monitor the temperatures and pressures at the inlets and exits of a compressor, a condenser, and an evaporator. A digital wattmeter was used to monitor power consumption, and a digital flow meter was used to monitor the mass flow rate of R134a. Heat loss to the surroundings and the changes in the kinetic and potential energy were neglected. Every experiment was conducted three times to obtain the highest accuracy and steady-state performance. Table 1 shows the technical details of the experimental system. An experimental set up and its schematic diagram are presented in Fig. 1. The experiment consists of a compressor, condenser, evaporator, and expansion valve.

No	Components	Characteristics
1	Compressor	Bitzer compressor 1/2 HP
2	Condenser	Air cooled condenser 1/2 HP
3	Evaporator	Emersion coil 1/3 HP
4	Expansion valve	Automatic expansion valve
5	Voltage rating	220V AC voltage supply
6	Suction line	3/8 inch copper pipe
7	Discharge line	1/4 inch copper pipe
8	Frequency rating	51 Hz
9	Defrost unit	Automatic
10	Door type	Single closed door



a)



b)

Fig. 1. a) Experimental work and b) corresponding schematic diagram of the experiment

Table 1. Technical details of the experimental system

**1.1.1 Experimental Procedure**

Using the Engineering Equation Solver (EES), the temperatures and pressure were measured at the inlet and outlet of the evaporator, condenser, and compressor to read the enthalpy of R134a. This software aids in determining the enthalpy of the gas and the change in the gas phase, where two states of the gas cycle were recorded in the system, specifically superheated vapour enthalpy ( $h_1, h_2$ ) at the inlet and the exit of the compressor, superheated vapour enthalpy ( $h_3$ ) at the inlet of the condenser, compressed liquid enthalpy ( $h_4$ ) at the exit of the condenser, compressed liquid enthalpy ( $h_5$ ) at the inlet of the evaporator, and superheated vapour enthalpy ( $h_6$ ) at the exit of the evaporator. The listed governing equations have been employed for analysis [33]. Characteristics of R134a utilized in the experimental setup are given in Table 2.

$$\dot{W} = \dot{m}(h_2 - h_1), \tag{1}$$

$$Q_{\text{evaporator}} = \dot{m}(h_6 - h_5), \tag{2}$$

$$Q_{\text{condenser}} = \dot{m}(h_3 - h_4), \tag{3}$$

$$COP = \frac{(h_6 - h_5)}{(h_2 - h_1)}. \tag{4}$$

**Table 2.** Characteristics of R134a [39]

No	Characteristics	
1	Name	1,1,1,2 tetrafluoroethene
2	Chemical formula	CF <sub>3</sub> CFH <sub>2</sub>
3	Molecular weight	102.03 g/mol
4	Composition	pure
5	ASHRAE safety classification	A1
6	Ozone depletion potential	zero
7	Lifetime in the atmosphere	13
8	Critical temperature	101.1 °C
9	Critical pressure	4.06.3 MPa
10	Normal boiling point NBP	-26.4 °C
11	Saturated vapor pressure at 20 °C	774.3 kPa
12	Latent heat of vaporization	198.6 kJ/kg
13	Liquid density	1294.8 kg/m <sup>3</sup>
14	Vapor density	14.43 kg/m <sup>3</sup>
15	Liquid Cp	1.341 kJ/(kg °C)
16	Vapor Cp	0.90 kJ/(kg °C)
17	Liquid thermal conductivity at 25 °C	0.0824 W/(m K)
18	Vapor thermal conductivity at 25 °C	0.0145 W/(m K)
19	Liquid viscosity at 25 °C	0.202 mPa s
20	Vapor viscosity at 25 °C	0.012 mPa s

**1.1.2 Simulation of Vapor Compression Refrigeration System**

Ansys Fluent version 19.0 software was chosen to make the mathematical model of the refrigeration system based on the real dimensions of the condenser and the evaporator and these two parts of the system were chosen to study the effect of average the temperature of each of them on the performance of the refrigeration system. The stages of designing the mathematical model were as follows: 1) Geometry, where the evaporator and condenser were drawn based on the real dimensions using a solid works program, and the drawn models were exported to Ansys Fluent, where the solid works helped to draw quickly and accurately; 2) Mesh, where the tubes of the evaporator and condenser were divided into many elements and nodes, and the change in the number of elements stops when the temperature inside the tube does not change and is close to the experimental value. The equations that were used to calculate the theoretical temperatures and pressures and the amount of heat absorbed and rejected are the continuity, momentum, and energy equations. The dimensions of the condenser and evaporator and their theoretical models are shown in Table 3 and Fig 2.

As shown in Fig. 2, the evaporator and condenser are designed so that the thermal gradient of the pipes appears at any point of entry. Also shown in the design is the gradient in the pressure and gradient in velocity to determine the velocity, pressure, and temperature of the refrigerant (R134a) while rotating inside the tubes. The colours shown in the drawing indicate that red gives the highest reading, blue the lowest reading, and the colours between red and blue are between the highest and the lowest in all cases of gradation, whether it is temperature, pressure, or velocity.

**1.2 Preparation of Nanoparticles**

The nanoparticles were prepared with nitrates, distilled water, and ammonia. A specified amount of copper nitrate was weighed in the case of preparing copper oxide and dissolving it in a specified amount of distilled water or deionized water. Similarly, a specified amount of cerium nitrate was weighed, in the case of preparing cerium oxide; and dissolving it in a specified amount of distilled water or deionized water. Distilled water is considered one of the cheapest and best solvents for all materials laboratories. As for preparing the mixture, specific quantities of both copper nitrate and cerium nitrate are weighed and dissolved in a specific amount of distilled water to

**Table 3.** Dimensions of condenser and evaporator

NO	Condenser Measurements	Dimensions	NO	Evaporator Measurements	Dimensions
1	Length	35 cm	1	Length	33 cm
2	Width	17 cm	2	Width	10 cm
3	Height	28 cm	3	Height	28 cm
4	Diameter of copper tube inside the condenser	0.25 inch	4	Diameter of copper tube inside the evaporator	0.25 inch
5	The twists and copper tube inside a condenser	18	5	The twists and copper tube inside an evaporator	18
6	Distance between one tube and another	5 cm	6	Area of evaporator	0.12 cm <sup>2</sup>
7	Area of condenser	0.177 cm <sup>2</sup>	7	Number of tubes	18
8	length of the tube inside the condenser	7.2 m	8	Fan speed	1300 rpm
9	The thickness of aluminium plate	0.3 mm	9	Air velocity	638 m/s
10	Number of plates	600	10	Evaporator type	emersion coil
11	Single plate dimensions	35 cm × 17 cm × 34 cm	11	Distance between one tube and another	3 cm
12	Fan speed	1300 rpm	12	Length of the tube inside the evaporator	6.48 m
13	Air velocity	638 m/s			
14	Condenser type	Air cooler			

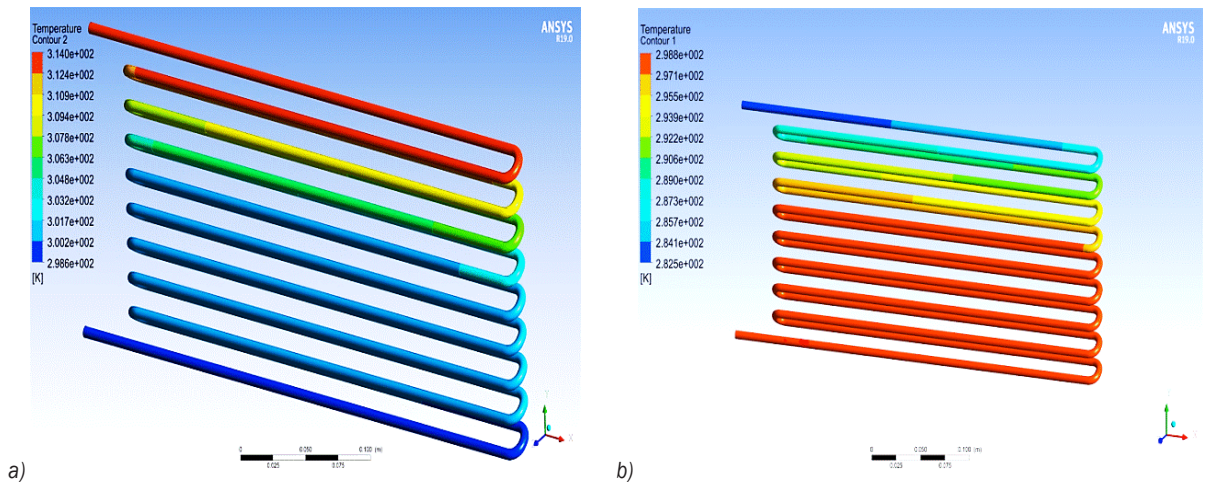


**Fig. 2.** a) Theoretical model of condenser, and b) theoretical model of evaporator without nanoparticles

begin preparation for the reaction until the oxide is obtained. The preparation process of the reaction is briefly described in the following steps:

1. Heating until 80 °C for 1 hour with a constant mixing speed of 375 rpm;
2. Adding ammonia at a constant temperature of 60 °C and a constant mixing speed of 375 rpm to reach Ph = 10 ± 1
3. Raising the temperature to 90 °C until copper oxide is deposited;
4. Cooling the solution to room temperature;
5. Filtration;
6. Drying in an electric oven at 110 °C for 1 hour;
7. Milling;
8. Screening; and
9. Packing.

According to the equations below, the nanoparticles were prepared as indicated clearly in Table 4 and their physical and chemical properties are shown in Table 5.

$$M = \frac{W}{M_w}, \tag{5}$$

$$C = \frac{n}{v}, \tag{6}$$

where  $M$  is mole [g/mol],  $W$  weight [g],  $M_w$  molecular weight [mol],  $C$  mole concentration [mol/l],  $n$  number of moles [-], and  $v$  volume [l].

Table 4 shows that the weights of substances involved in the reaction have been converted to moles by dividing the weight by the molecular weight as

indicated in Eq. (5) then the molar concentration was calculated as indicated in Eq. (6) by dividing the number of moles by the volume of the solvent in litres.

Note that the molecular weights of the reactants were as follows:

$$\text{Cu}(\text{NO}_3)_2 \cdot 3\text{H}_2\text{O} = 241.606$$

$$\text{Ce}(\text{NO}_3)_3 \cdot 6\text{H}_2\text{O} = 434.22$$

$$\text{CuO} = 79.5$$

$$\text{CeO}_2 = 172.12$$

**Table 4.** The quantities obtained from the mixtures

Mixture number	Percentages		Molar concentration		The Quantity [g]
	CuO [%]	CeO <sub>2</sub> [%]	Cu(NO <sub>3</sub> ) <sub>2</sub> · 3H <sub>2</sub> O	Ce(NO <sub>3</sub> ) <sub>3</sub> · 6H <sub>2</sub> O	
1	50	50	0.20867	0.09673	12.67
2	60	40	0.250408	0.07753	11.44
3	70	30	0.300075	0.05834	10.97
4	40	60	0.16694	0.11622	13.07
5	30	70	0.125687	0.135569	13.85

**Table 5.** Nanoparticles properties [40]

No	Nanoparticles	M <sub>w</sub> [g/mol]	ρ [kg/m <sup>3</sup> ]	K [W/(mK)]	C <sub>p</sub> [J/(kgK)]
1	CuO	79.55	6320	32.9	536
2	CeO <sub>2</sub>	172.1	6100	11.7	352
3	50 % CuO + 50 % CeO <sub>2</sub>	125.8	6210	22.3	444
4	60 % CuO + 40 % CeO <sub>2</sub>	116.5	6232	24.4	462
5	70 % CuO + 30 % CeO <sub>2</sub>	107.3	6254	26.5	481
6	40 % CuO + 60 % CeO <sub>2</sub>	135.1	6188	20.1	426
7	30 % CuO + 70 % CeO <sub>2</sub>	144.3	6166	18.0	407

where  $M_w$  is molar mass [g/mol],  $K$  is thermal conductivity [W/(m K)],  $\rho$  is density [kg/m<sup>3</sup>], and  $C_p$  specific heat [J/(kg K)].

### 1.3 Mathematical Models

After completing the geometry and mesh stages that are referred to in Section 1.1.2, the refrigeration system for this study is ready to receive the nanoparticles. This stage is called “setup” where the multiphase is used as the best model for the solution. The properties of both R134a are entered in the liquid and gaseous phase, and the nanoparticles with the proportions specified for it depending on the nanofluid equations and dealing with nanoparticles and R134a based on becoming one homogeneous material as shown below.

$$K_{eff} = kbf \left( \frac{kp + 2kbf - 2(kp - kbf)\phi}{kp + 2kbf - (kp - kbf)\phi} \right), \quad (7)$$

where  $K_{eff}$ ,  $Kbf$ , and  $kp$  are the thermal conductivities of the nano-refrigerant, base refrigerant in the liquid phase and particle, respectively, and  $\phi$  is the particle volume fraction:

$$\mu_{nr} = \mu_r \frac{1}{(1-\phi)^{2.5}}, \quad (8)$$

where  $\mu_{nr}$  and  $\mu_r$  are the dynamic viscosities of the nano-refrigerant and refrigerant, respectively.

The density and specific heat of the nano-refrigerant are shown in Eqs. (9) and (10).

$$\rho_{eff} = (1-\phi)\rho_f + \phi\rho_{np}, \quad (9)$$

$$C_{pmf} = \frac{(1-\phi)(\rho cp)bf + \phi(\rho cp)np}{(1-\phi)\rho bf + \phi\rho np}, \quad (10)$$

where  $\phi$ ,  $\rho bf$ ,  $\rho_{np}$ ,  $np$ ,  $cp$  are volume fraction of nanoparticles, density of base fluid, density of nanoparticles, specific heat of base refrigerant, and specific heat of nanoparticles, respectively, [41] and [42].

A multiphase model solves the momentum, continuity, and energy equations for the mixture, and solves the equation of volume fraction for the secondary phases [43] and [44]. A continuity equation for the volume fraction of one (or more) of the phases. For the  $q$ <sup>th</sup> phase, this equation has the following form:

$$\frac{1}{\rho_q} \left[ \frac{\partial}{\partial t} (\alpha_q \rho_q) + \nabla \cdot (\alpha_q \rho_q \vec{v}_q) \right] = S_{\alpha_q} + \sum_{\rho=1}^n (\dot{m}_{\rho q} - \dot{m}'_{\rho q}), \quad (11)$$

where  $\dot{m}_{\rho q}$  is the mass transfer from phase  $\rho$  to  $q$  phase,  $-\dot{m}'_{\rho q}$  the mass transfer from phase  $q$  to phase  $\rho$ . A single momentum equation is solved throughout the domain; it is dependent on the volume fractions of all phases through the properties  $\rho$  and  $\mu$ .

$$\frac{\partial}{\partial t} (\rho \vec{v}) + \nabla \cdot (\rho \vec{v} \vec{v}) = -\nabla \rho + \nabla \cdot \left[ \mu (\nabla \vec{v} + \nabla \vec{v}^T) \right] \rho \vec{g} + \vec{F}. \quad (12)$$

The energy equation, is also shared among the phases

$$\frac{\partial}{\partial t} (\rho E) + \nabla \cdot (\vec{v} \cdot (\rho E + P)) = \nabla \cdot (K_{eff} \nabla T) + S_h. \quad (13)$$

The amount of nanoparticles that was added to R134a was 2.6 g, while the amount of R134a was 1039 g, as this was the amount that the system was operating within the first part of the experiment to

become a mass fraction of 0.25 wt.%. The theoretical results obtained by adding a quantity of nanoparticles are presented and their effects on the performance of the refrigeration system are discussed in the discussion section.

## 2 RESULTS AND DISCUSSION

This section is divided into three parts; the first part includes a discussion of the results obtained by conducting an experiment on a vapor compression refrigeration system and comparing these results with a simulation that was done using Ansys Fluent 19.0 software program and calculating the accuracy rate. The second part includes discussing the results obtained from the preparation of nanoparticles by presenting nanoparticle screening tests using X-ray diffraction (XRD) and scanning electron microscope (SEM) methods. The third part includes discussing the results obtained from the theoretical study where nanoparticles were introduced to a vapour

compression refrigeration system to investigate their effects on the coefficient of performance of the system.

### 2.1 Comparison of Experimental and Theoretical Results of a Vapor Compression Refrigeration System

A theoretical model was designed for the evaporator and condenser with specifications similar to the experimental system; the results obtained were illustrated graphically to show the effects of the average temperature of both the evaporator and condenser on  $COP$ , and  $W_{comp}$  as shown in Fig. 3. The  $COP$  at varying evaporator temperatures is presented in Fig 3a; an increase in evaporator temperatures causes an increase in  $COP$  due to an increase in the refrigeration effect because of increase in both the enthalpy difference and mass flow rate of R134a through the evaporator, and a decrease in compressor work. The power consumption at varying evaporator temperatures is presented in Fig.

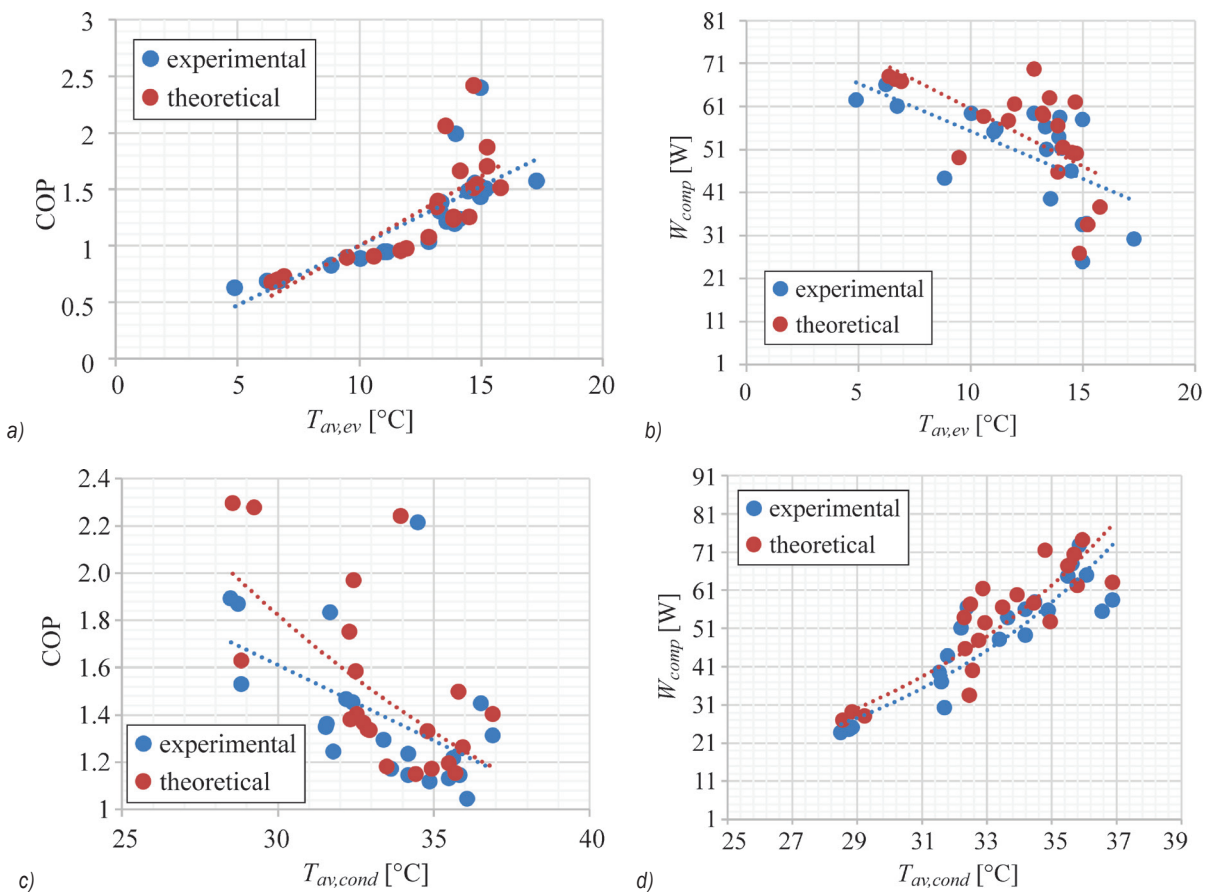


**Fig. 3.** a) The effect of  $T_{av,ev}$  on  $COP$  b) the effect of  $T_{av,ev}$  on the power consumption  $W_{comp}$  c) The effect of  $T_{av,cond}$  on  $COP$ , and d) The effect of  $T_{av,cond}$  on the power consumption  $W_{comp}$

3b; an increase in evaporator temperatures causes a decrease in power consumption, due to an increase in suction temperature, which causes an increase in both vaporization pressure and density suction vapor entering the compressor, which leads to an increased mass flow rate of R134a through the compressor for a given piston displacement and decreased power consumption. The effects of the average temperature of the condenser on the COP are presented in Fig. 3c; it decreases as the condenser temperature increases due to a decrease in the refrigeration effect and an increase in compressor work. Increased condenser temperatures cause an increase in the heat rejection, due to the rise in enthalpy difference and mass flow rate of R134a through the condenser. In contrast, the increase in condenser temperature will cause an increase in power consumption, as presented in Fig. 3d. To achieve high accuracy, the experiment was divided into several cases, in which each case included five experiments. Each experiment was repeated three times. The experiment which gave the most convergence with the theoretical value calculated using Ansys Fluent was chosen to then capture all these points to be plotted with the average

temperatures of the evaporator and condenser. As shown by the results and in agreement with previous studies, our results confirmed the increase in COP with the temperature of the evaporator and its decrease with the increase in temperature of the condenser, as well the decrease in energy consumption with an increase in the average temperature of the evaporator and increased with increasing the average temperature of the condenser

## 2.2 Characterization of Nanoparticles

Nanoparticle characterization was carried out at the Huazhong University of Science and Technology in China on September 24, 2019, by using XRD analysis and SEM images. The results of the nanoparticles are presented below in Fig. 4. The XRD pattern was scanned from 20 deg to 80 deg and the XRD profile confirmed the nanocrystalline nature of CuO. The characteristic diffraction peak was observed, and all of the peaks agreed in position and intensity with the database standard (JCPDS 00-045-0937) of the face-centred cubic CuO crystal with the fluorite structure. The absence of additional diffraction peaks confirms

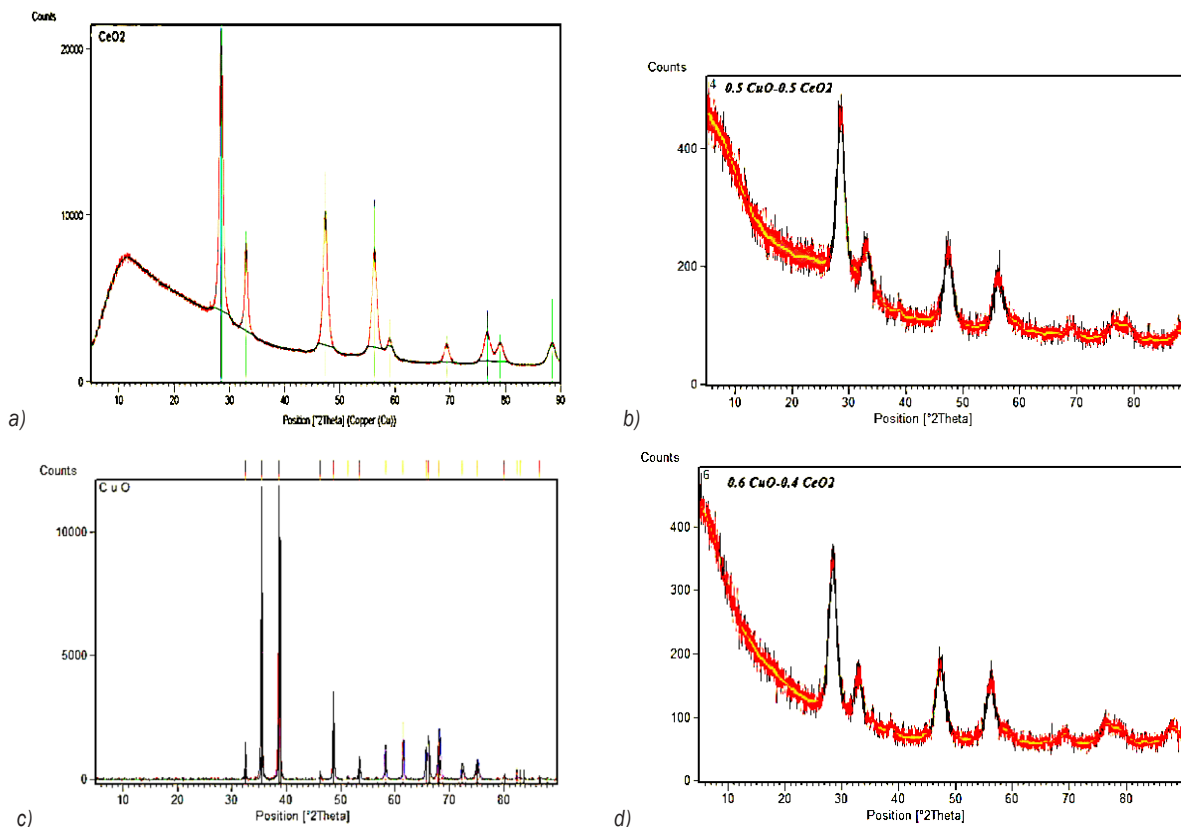


Fig. 4. XRD Pattern of a) pure CuO, b) pure CeO<sub>2</sub>, c) 0.5 % CuO, 0.5 % CeO<sub>2</sub>, and d) 0.6 % CuO, 0.4 % CeO<sub>2</sub> nanoparticles

the nanocrystalline nature and purity of the samples. The XRD pattern of  $\text{CeO}_2$  was scanned from 20 deg to 80 deg, and the XRD profile confirmed the nanocrystalline nature of  $\text{CeO}_2$ . The characteristic diffraction peak was observed, and all of the peaks agreed in position and intensity with the database standard (JCPDS 00-004-0593) of the face-centred cubic  $\text{CeO}_2$  crystal with the fluorite structure. The absence of additional diffraction peaks confirms the nanocrystalline nature and purity of the samples. The SEM images proved that the particles of the samples were approximately spherical in shape and the particle sizes of  $\text{CuO}$ ,  $\text{CeO}_2$ , 0.5 %  $\text{CuO}$  + 0.5 %  $\text{CeO}_2$ , and 0.6 %  $\text{CuO}$  + 0.4 %  $\text{CeO}_2$  were observed to be 78.95 nm, 79.9 nm, 44.15 nm, and 63.3 nm, respectively, based on the SEM images, as shown in Fig. 5. This research succeeded in preparing nanoparticles with suitable diameters. Cerium oxide was used for the first time to determine its effect on the performance of refrigeration system. It is expected that this study will open the door to future research to reveal new properties of cerium oxide as a mixture with copper

oxide; in particular, the mixture consisting of both oxides was prepared by the same method in this experiment as a homogeneous substance

### 2.3 The Results Obtained from Adding Nanoparticles Theoretically into a Vapor Compression Refrigeration System

The results obtained from adding  $\text{CuO}$  are illustrated in Fig. 6 to show the effects of the average temperature of the evaporator on the  $COP$ , and  $W_{comp}$ . As it appears from the results, the addition of 0.25 wt.%  $\text{CuO}$  caused an increase in the temperature of the evaporator at its entrance and exit, which led to a rise in both the  $COP$  and the amount of heat absorbed inside the evaporator and thus a decrease in the amount of energy consumed by the compressor. This conclusion is consistent with previous studies, and the main reason for the occurrence of these changes is the high thermal conductivity of the refrigerant due to its mixture with  $\text{CuO}$ , which records an average thermal conductivity of 20 W/(mK) to 40 W/(mK). The addition of the

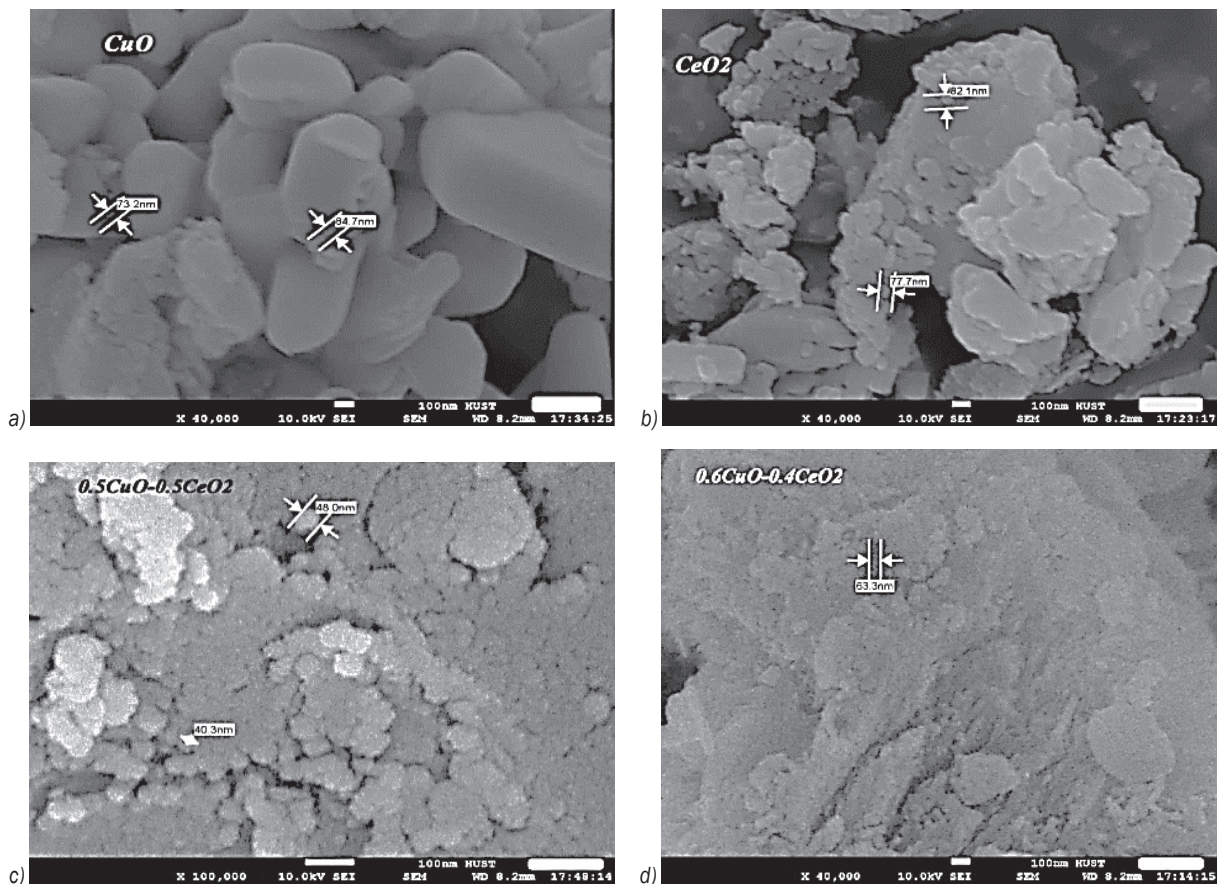
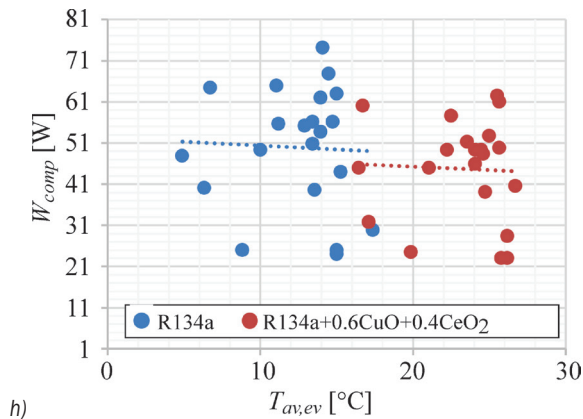
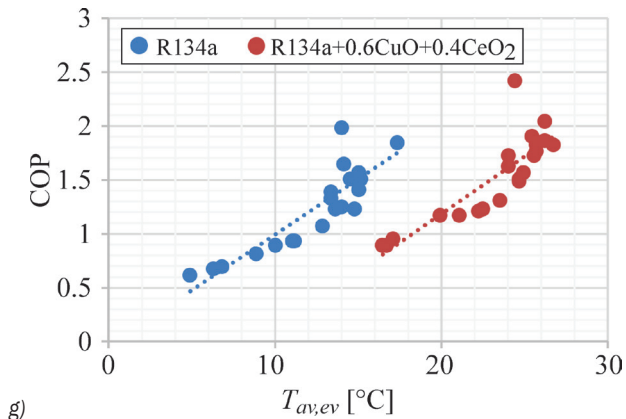
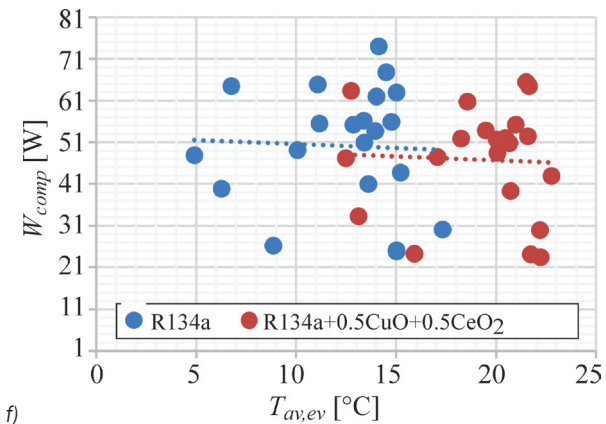
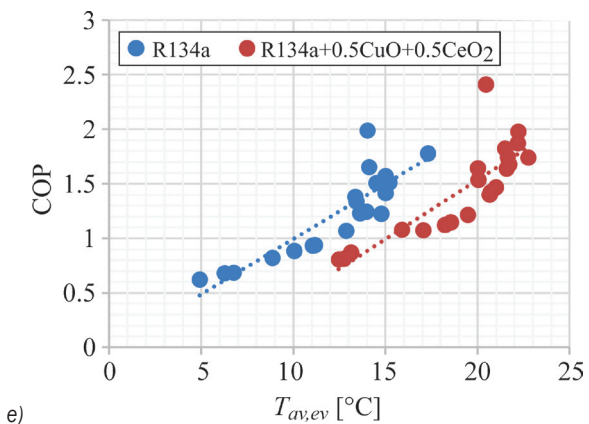
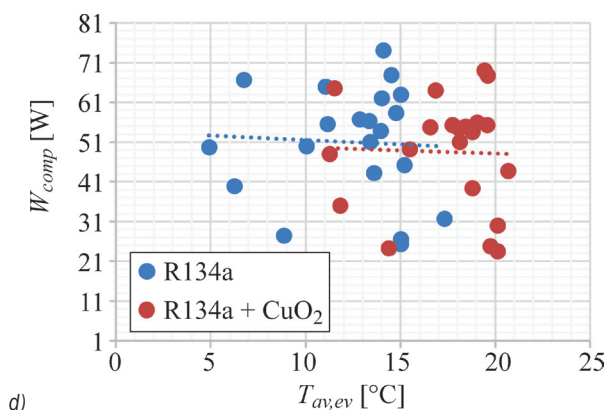
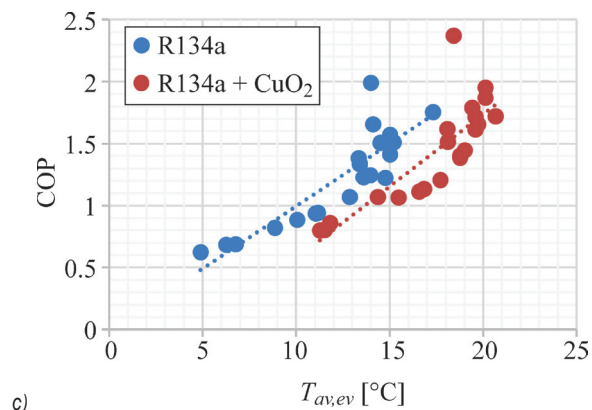
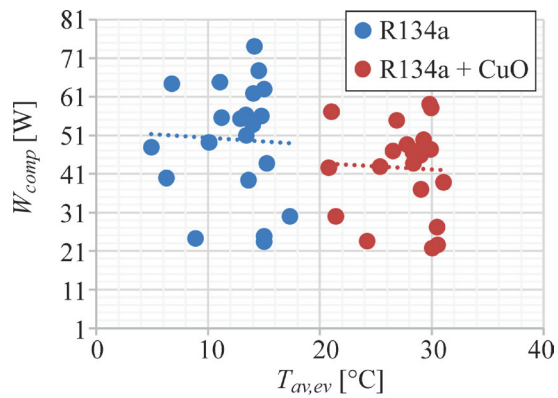
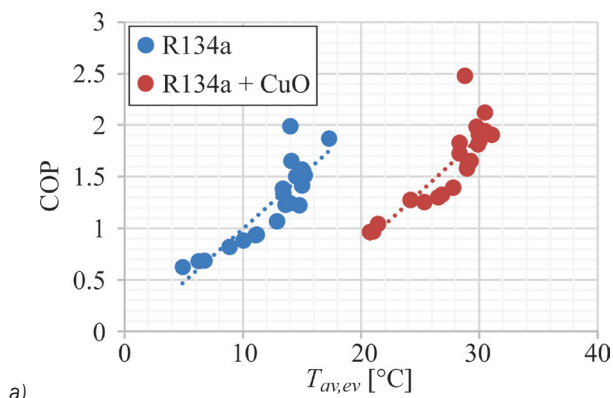


Fig. 5. a) spherical  $\text{CuO}$ , b) spherical  $\text{CeO}_2$ , c) spherical 0.5 %  $\text{CuO}$  + 0.5 %  $\text{CeO}_2$ , and d) spherical 0.6 %  $\text{CuO}$  + 0.4 %  $\text{CeO}_2$



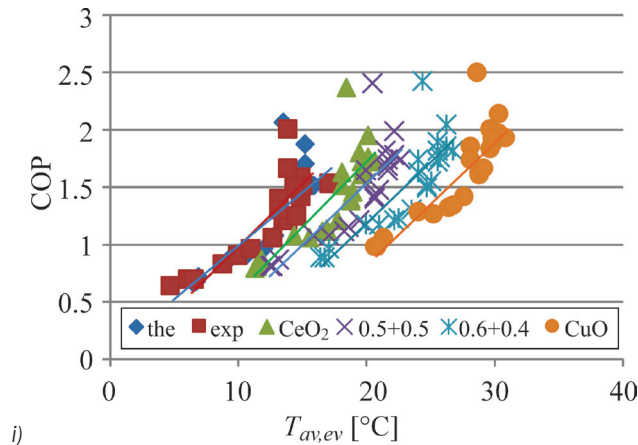


Fig. 6. The effect of  $T_{av,ev}$  on  $COP$  and  $W_{comp}$  at constant mass fraction and comparing of the results of a vapor compression refrigeration system with nano and without nanoparticles

same amount of  $CeO_2$  caused an increase in the temperature of the evaporator at its entrance and exit, which led to a rise in both  $COP$  and the amount of heat absorbed inside the evaporator and thus a decrease in the amount of energy consumed inside the compressor. The main reason for the occurrence of these changes is the high thermal conductivity of the refrigerant due to its mixture with  $CeO_2$ , where it records an average thermal conductivity of 11.7 W/(mK). The addition of the same amount of 0.5 %  $CuO$  with 0.5 %  $CeO_2$  caused an increase in the temperature of the evaporator at its entrance and exit, which led to a rise in both  $COP$  and the amount of heat absorbed inside the evaporator and thus a decrease in the amount of energy consumed inside the compressor. The main reason for the occurrence of these changes is the high thermal conductivity of the refrigerant due to its mixture with nanoparticles. The addition of the same amount of 0.6 %  $CuO$  with 0.4 %  $CeO_2$  caused an increase in the temperature of the evaporator at its entrance and exit, which led to a rise in both the  $COP$  and the amount of heat absorbed inside the evaporator thus a decrease in the amount of energy consumed inside the compressor. The main reason for the occurrence of these changes is the high thermal conductivity of the refrigerant due to its mixture with nanoparticles. Since the most important factor in improving the performance of the refrigeration system after adding the nanoparticles is the temperature of the evaporator, all the results were plotted so that the effect of the average evaporator temperature on the  $COP$  of the system at a specific amount of nanoparticles is shown. Nagaraju and Reddy [32] proved that adding copper oxide to R134a improved the  $COP$  of the refrigeration system to

a degree close to what was found in this study, and the method in which nanoparticles are prepared, the shape, diameter, and quantity added to the refrigerants play an important role in determining the result.

### 3 CONCLUSION

A new concept of nanoparticles was introduced in this research to open the door to answering many questions in the future, because cerium oxide was used with copper oxide as one material consisting of a mixture of both oxides. The results obtained for copper oxide agreed with previous studies, where copper oxide succeeded in improving the performance of the refrigeration system and increased  $COP$  by 25 %, and cerium oxide succeeded in improving the performance of the system by a lesser value. For the mixture, the results confirmed that the mixture containing a higher percentage of copper oxide gave better results. The door remains open for more experimental studies on the use of cerium oxide as a single oxide or as a mixture with other oxides to study its effect on the performance of the vapor compression refrigeration system and whether the refrigeration system will work safely. In addition, more experiments needed to study the effect of the mixtures mentioned in this research on the stability of nanoparticles with refrigerants and lubricant oils, as the problem of stability is one of the greatest obstacles to the application of nanoparticles in the refrigeration systems.

### 4 FUTURE WORK

In this study the method of preparing nanoparticles was simple and affordable and produced two types

of oxides and five types of mixtures. Subsequently, the field of research remains open. This method succeeds in obtaining other oxides, especially oxides with high thermal conductivity, because the cost of nanoparticles increases as their thermal conductivity increases. Nevertheless, the theoretical results in this research encourage researchers to move forward with experimental studies. This study recommends conducting experiments to verify the behaviour of cerium oxide in refrigeration systems and to monitor its behaviour at different temperatures for the evaporator, especially because the results of this research show that cerium oxide improved the performance of the refrigeration system due to its good thermal conductivity. This study recommends mixing materials that have been prepared with other refrigerants and compressor lubricant oils to study their effect on the thermophysical properties of refrigerants and oils. Since the problem of the stability of nanoparticles with refrigerants is so important, a hybrid consisting of oxides was recently used to solve this problem. The mixture prepared from oxide succeed in obtaining better results, especially since the mixture consisting of 50% copper oxide and 50 % cerium oxide has already been mixed with R134a in the lab using the ultrasonic machine only for one hour; the result was a stable mixture for a whole day

## 5 ACKNOWLEDGMENTS

I would like to thank Yildiz Technical University in Istanbul Turkey, where the first part of this research was carried out in Mechanical Engineering Laboratories under the supervision of Dr Ahamet Salim. I take an opportunity to express my sincere thanks and gratitude to Dr Jassim M. H. Alkurdhani who helped me to prepare the nanoparticles and showed me a different way to achieve my goal, and Dr Yusuf Bedeli who provided me with the laboratory so that I could prepare the nanoparticles. I also extend my thanks to Huajong University in China and Gazi University in Ankara/Turkey for their help in examining and identifying the properties of the nanoparticles.

## 6 REFERENCES

- [1] Bhattad, A., Sarkar, J., Ghosh, P. (2017). Improving the performance of refrigeration systems by using nanofluids: A comprehensive review. *Renewable and Sustainable Energy Reviews*, vol. 82, p. 3656-3669, DOI:10.1016/j.rser.2017.10.097.
- [2] N. Abu-Libde, N., Redouane, F., Aissa, A., Mebarek-Oudina, F., Almuhtady, A., Jamshed, W., Al-Kouz, W. (2021). Hydrothermal and entropy investigation of Ag/MgO/H<sub>2</sub>O hybrid nanofluid natural convection in a novel shape of porous cavity. *Applied Sciences*, vol. 11, no. 4, art. ID 1722, DOI:10.3390/app11041722.
- [3] Hussien, A.A., Al-Kouz, W., Yusop, N.M., Abdullah, M.Z., Janvekar, A.A. (2019). A brief survey of preparation and heat transfer enhancement of hybrid nanofluids. *Strojniški vestnik Journal of Mechanical Engineering*, vol. 65, no. 7-8, p. 441-453, DOI:10.5545/sv-jme.2019.6077.
- [4] Nair, V., Tailor, P.R., Parekh, A.D. (2016). Nanorefrigerants: A comprehensive review on its past, present and future. *International Journal of Refrigeration*, vol. 67, p 290-307, DOI:10.5545/sv-jme.2019.6077.
- [5] Majgaonkar, A.S. (2016). Use of nanoparticles in refrigeration systems: A literature review paper. *16<sup>th</sup> International Refrigeration and Air Conditioning Conference*, p. 1-10.
- [6] Celen, A., Çebi, A., Aktas, M., Mahian, O., Dalkilic, A.S., Wongwises, S. (2014). A review of nanorefrigerants: Flow characteristics and applications. *International Journal of Refrigeration*, vol. 44, p. 125-140, DOI:10.1016/j.ijrefrig.2014.05.009.
- [7] Vijayakumar, M., Rohith Ambadi, S., Selvakumar, P., Mathan, P. (2021). An analysis of household refrigerator using Polyester - Aluminum oxide Nano lubrication, *Materials Today: Proceedings*, In Press, DOI:10.1016/j.matpr.2021.04.377.
- [8] Choi, T.J., Kim, D.J. Jang, S.P., Par, S., Ko, S. (2021). Effect of polyolester oil-based multi walled carbon-nanotube nanolubriant on the coefficient of performance of refrigeration systems. *Applied Thermal Engineering*, vol. 192, art. ID 116941, DOI:10.1016/j.applthermaleng.2021.116941.
- [9] Senthilkumar, A., Abhijith, E.P., Jawhar, C.A.A., Jamshid, (2021). Experimental investigation of Al<sub>2</sub>O<sub>3</sub>/SiO<sub>2</sub> hybrid nanolubriant in R600a vapour compression refrigeration system. *Materials Today: Proceedings*, vol. 45, p. 5921-5924, DOI:10.1016/j.matpr.2020.08.779.
- [10] Senthilkumar, A., Abhishek, P.V., Adithyan, M., Arjun, A. (2021). Experimental investigation of CuO/SO<sub>2</sub> hybrid nano-lubricant in R600a vapour compression refrigeration system. *Materials Today: Proceedings*, vol. 45, p. 6083-6086, DOI:10.1016/j.matpr.2020.10.178.
- [11] Senthilkumar, A., Anderson, A. (2021). Experimental investigation of SiO<sub>2</sub> nanolubriant for R410A vapour compression refrigeration system. *Materials Today: Proceedings*, vol. 44, p. 3613-3617, DOI:10.1016/j.matpr.2020.09.659.
- [12] Senthilkumar, A., Sahaluddeen, P.A.M., Noushad, M.N., Musthafa, E.K.M. (2021). Experimental investigation of ZnO/SiO<sub>2</sub> hybrid nano-lubricant in R600a vapours compression refrigeration system. *Materials Today: Proceedings*, vol. 45, p. 6087-6093, DOI:10.1016/j.matpr.2020.10.180.
- [13] Senthilkumar, A., Anderson, A., Sekar, M. (2021). Performance analysis of R600a vapour compression refrigeration system using CuO/Al<sub>2</sub>O<sub>3</sub> hybrid nanolubriant. *Applied Nanoscience*, p 1-17, DOI:10.1007/s13204-021-01936-y.
- [14] Javadi, F.S., Saidur, R. (2021). Thermodynamic and energy efficiency analysis of a domestic refrigerator using Al<sub>2</sub>O<sub>3</sub>

- nano-refrigerant. *Sustainability*, vol. 12, no. 10, art. ID 5659, DOI:10.3390/su13105659.
- [15] Gill, J., Singh, J., Ohunakin, O.S., Adelekan, D.S. (2019). Energy analysis of a domestic refrigerator system with ANN using LPG/TiO<sub>2</sub>-lubricant as replacement for R134a. *Journal of Thermal Analysis and Calorimetry*, vol. 135, p. 475-488, DOI:10.1007/s10973-018-7327-3.
- [16] Karthick, M., Karupiah, S.K., Kanthan, V. (2020). Performance investigation and exergy analysis of vapor compression refrigeration system operated using R600a refrigerant and nanoadditive compressor oil. *Thermal Science*, vol. 24, no. 5, p. 2977-2989, DOI:10.2298/TSCI180527024M.
- [17] Adelekan, D.S., Ohunakin, O.S., Gill, J., Atayero, A.A., Diarra, C.D., Asuzu, E.A. (2019). Experimental performance of a safe charge of LPG refrigerant enhanced with varying concentrations of TiO<sub>2</sub> nano-lubricant in a domestic refrigerator. *Journal of Thermal Analysis and Calorimetry*, vol. 136, p. 2439-2448, DOI:10.1007/s10973-018-7879-2.
- [18] Subhedar, D.G., Patel, J.Z., Ramani, B.M. (2020). Experimental studies on vapour compression refrigeration system using Al<sub>2</sub>O<sub>3</sub>/mineral oil nano-lubricant. *Australian Journal of Mechanical Engineering*, p. 1-6, DOI:10.1080/14484846.2020.1784558.
- [19] Babarinde, T.O., Akinlabi, S.A., Madyira, D.M. (2019). Experimental investigation of R600a/TiO<sub>2</sub>/mineral oil as a drop-in replacement for R134a/POE oil in a household refrigeration system. *International Journal of Ambient Energy*, vol. 43, no. 1, p. 539-545, DOI:10.1080/01430750.2019.1653983.
- [20] Selimefendigil, F., Bingölbali, T. (2019). Experimental investigation of nano compressor oil effect on the cooling performance of a vapor compression refrigeration system. *Journal of Thermal Engineering*, vol. 5, no. 1, p. 100-104, DOI:10.18186/thermal.513023.
- [21] Sundararaj, S., Manivannan, R. (2020). Comparative energetic and exergetic analysis of vapour compression refrigeration system with Au, HAuCl<sub>4</sub> and CNT nanoparticles. *AIP Conference Proceedings*, vol. 2270, art. ID 110038, DOI:10.1063/5.0019669.
- [22] Peyyala, A., Sri, M.N.S. Sudheer, N.V.V.S., KUMAR, K.Ch.K. (2020). Experimental investigation on effect of nano lubrication in a VCRS using R410a refrigerant with Al<sub>2</sub>O<sub>3</sub> nano particles. *International Journal of Mechanical and Production Engineering Research and Development*, vol. 10, no. 3, p. 1761-1768.
- [23] Babarinde, T.O., Akinlabi, S.A., Madyira, D.M., Ekundayo, F.M. (2020). Enhancing the energy efficiency of vapour compression refrigerator system using R600a with graphene nanolubricant. *Energy Reports*, vol. 6, p. 1-10, DOI:10.1016/j.egy.2019.11.031.
- [24] Adelekan, D.S., Ohunakin, O.S., Gill, J., Atiba, O.E., Okokpuijea, I.P., Atayero, A.A. (2019). Experimental investigation of a vapour compression refrigeration system with 15nm TiO<sub>2</sub>-R600a nano-refrigerant as the working, *Procedia Manufacturing*, vol. 35, p.1222-1227, DOI:10.1016/j.promfg.2019.06.079.
- [25] Ajayi, O.O., Ukasoanya, D.E., Ogbonnaya, M., Salawu, E.Y., Okokpuije, I.P., Akinlabi, S.A., Akinlabi, E.T., Owoloye, F.T. (2019). Investigation of the effect of R134a/Al<sub>2</sub>O<sub>3</sub> nanofluid on the performance of a domestic vapour compression refrigeration system. *Procedia Manufacturing*, vol. 35, p. 112-117, DOI:10.1016/j.promfg.2019.05.012.
- [26] Senthilkumar, A., Anderson, A. (2020). Experimental investigation of SiO<sub>2</sub> nanolubricants for R410A vapours compression refrigeration system. *Materials Today: Proceeding*, vol. 44, p. 3613-3617, DOI:10.1016/j.matpr.2020.09.659.
- [27] Pawale, K.T., Dhupal, A.H., Kerkal, G.M. (2017). Performance analysis of VCRS with nano-refrigerant. *International Research Journal of Engineering and Technology*, p. 1031-1037.
- [28] Kumar, G.S., Deepika, P., Kumar, M.N., Kumar, B.M., Kumar, K.N. (2018). Performance analysis of VCRS using nanorefrigerants. *International Research Journal of Engineering and Technology*, vol. 5, no. 3, p. 3869-3872.
- [29] Manikanden, V.S., Avinash, A. (2019). An experimental insight into the effects of silverdoped cupric oxide nanoparticles on the performance of hydrocarbon refrigeration system. *SN Applied Sciences*, vol 1, art. ID 1462, DOI:10.1007/s42452-019-1528-7.
- [30] Kundan, L., Singh, K. (2020), Improved performance of a nanorefrigerant-based vapor compression refrigeration system: A new alternative. *Proceedings of the Institution of Mechanical Engineers, Part A: Journal Power and Energy*, vol. 235, no. 1, p. 106-123, DOI:10.1177/0957650920904553.
- [31] Nagaraju, M., Reddy, V.M. (2018), Experimental refrigeration test of R134a mixed with mineral oil and (CuO) nanoparticle. *International Journal of Scientific Research in Science, Engineering and Technology*, vol. 4, no. 4, p. 288-293.
- [32] Kumar, A.S., Tiwari, A.C. (2019). An experimental investigation of VCRS using R134a/R600a/PAG oil/ Nano-Cu as working fluid. *International Journal of Innovative Research in Technology*, vol. 6, no. 7, p. 116-120.
- [33] Kumar, V.P.S., Baskaran, A., Subaramanian, K.M. (2016). A performance study of Vapour compression refrigeration system using ZrO<sub>2</sub> nano particle with R134a and R152a. *International Journal of Scientific and Research Publications*, vol. 6, no. 12, p. 410-421.
- [34] Mahdi, Q.S., Theeb, M.A., Saed, H. (2017). Enhancement on the performance of refrigeration system using the nano-refrigerant. *Journal of Energy and Power Engineering*, vol. 11, p. 237-243, DOI:10.17265/1934-8975/2017.04.004.
- [35] Singh, P.P.P. (2017). *Experimental investigation of Vapour compression refrigeration system by comparing the results procured after using pure refrigerant R134a with and without titanium oxide nanoparticle*. MSc Thesis, University of Punjab, Punjab, p. 1-52.
- [36] Kedzierski, M.A., Brignoli, R., Quine, K.T., Brown, J.S. (2017). Viscosity, density, and thermal conductivity of aluminum oxide and zinc oxide nanolubricants. *International Journal of Refrigeration*, vol. 74, p. 3-11, DOI:10.1016/j.ijrefrig.2016.10.003.
- [37] Sanukrishna, S.S., Prakash, M.J. (2018). Experimental studies on thermal and rheological behaviour of TiO<sub>2</sub>-PAG nanolubricant for refrigeration system. *International Journal of Refrigeration*, vol. 86, p. 356-372, DOI:10.1016/j.ijrefrig.2017.11.014.

- [38] Zawawi, N.N.M., Azmi, W.H., Redhwan, A.A.M., Sharif, M.Z., Samykano, M. (2018). Experimental investigation on thermo-physical properties of metal oxide composite nanolubricants. *International Journal of Refrigeration*, vol. 89, p. 11-21, DOI:10.1016/j.ijrefrig.2018.01.015.
- [39] Makhnatch, P., Babiloni, A.M., López-Belchí, A., Khodabandeh, R. (2019). R450A and R513A as lower GWP mixtures for high ambient temperature countries: Experimental comparison with R134a. *Energy*, vol. 166, p. 223-235, DOI:10.1016/j.energy.2018.09.001.
- [40] Thermaltest Instruments (2018). From <https://thermtest.com/what-is-thermal-conductivity>, accessed on 2021-10-26.
- [41] Alawi, O.A., Sidik, N.A.C. (2014). Influence of particle concentration and temperature on the thermophysical properties of CuO/R134a nanorefrigerant. *International Communications in Heat and Mass Transfer*, vol. 58, p.79-84, DOI:10.1016/j.icheatmasstransfer.2014.08.038.
- [42] Duggal, M., Sharma, A., Dondapati, R.S., Usurumarti, P.R. (2016). Enhancement of thermo-hydraulic performance of evaporators using nanorefrigerants. *3<sup>rd</sup> International Conference on Electrical, Electronics, Engineering Trends, Communication, Optimization and Sciences*, p. 669-674.
- [43] Hernández, D.C., Nieto-Londoño, C., Zapata-Benabithe, Z. (2016). Analysis of working nanofluids for a refrigeration system, *DYNA*, vol. 83, p. 176-183, DOI:10.15446/dyna.v83n196.50897.
- [44] ANSYS, Inc. (2013). *Ansys fluent 19.0, Theory Guide*, Canonsburg.

# Indices to Evaluate the Performance of Force Transmission and Constraint for Parallel Mechanisms

Tie Zhang\* – Yachao Cao – Guangcai Ma

South China University of Technology, School of Mechanical and Automotive Engineering, China

*The force transmission and constraint ability significantly influence the performance of parallel mechanisms (PMs), such as force dexterity, overall rigidity and accuracy. The transmission wrench screw (TWS) transmits the force between the actuator and end-effector, and the constraint wrench screw (CWS) resists structural deformations. They significantly influence the manipulability to transmit force and the consistency to resist deformations. In this study, two new indices are proposed to evaluate their manipulability and consistency. The indices are notable for their unit homogeneity, frame independence, and measurement facility without interference. By taking three PMs with different mobility properties as examples, the effectiveness of the two indices for evaluating the manipulability to transmit force and the consistency to resist deformations is verified. Based on the indices, the configuration of a 3-CRU (C a cylindrical joint, R a revolute joint, and U a universal joint) PM with optimal force transmission and constraint ability is constructed.*

**Keywords:** force transmission manipulability, force constraint consistency, transmission wrench screw, constraint wrench screw, parallel mechanism

## Highlights

- Two new indices with advantages are proposed to evaluate their manipulability and consistency.
- The corresponding formulas are derived under different transmission and constraint matrices.
- Simulations of three different PMs are carried out to verify the effectiveness of the two indices.
- The structural configuration of the 3-CRU PM whose TMI and CCI remain maximal is constructed.

## 0 INTRODUCTION

Parallel mechanisms (PMs) have been wide industrial applications due to their merits such as high load-to-weight ratio [1], compact structure [2], good accuracy [3] and dynamic performance [4]. Performance evaluation helps to measure the practical value of PMs before their application. In general, the performance evaluation indices are based on the Jacobian matrix and power to describe the motion and force performance as a whole evaluation index system. The determinant value of the Jacobian matrix as the force transmission index was adopted first by Denavit et al. [5]. Subsequently, performance indices based on the Jacobian matrix were proposed, such as manipulability measure [6], global conditioning index [7], and so on. However, both Merlet [8] and Wang et al. [9] pointed out that these indices are not suitable for the PMs with both rotational and translational degrees of freedom (DoFs). In 1932, the concept of transmission angle was first proposed by Alt [10]. The standardized form of transmission index was put forward by Sutherland and Roth [11], and then it was improved by Tsai and Lee [12]. Furthermore, an input and output transmission index [13] was introduced to describe the motion/force transmission performance of parallel manipulators. A general and systematic method described the motion/force transmissibility of

redundantly actuated and over-constrained PMs [14]. Moreover, a modified output transmission index based on an equivalent transmission wrench screw was defined to evaluate the transmissibility of high-speed articulated-platform parallel robots [15].

Highly dynamic handling tasks cannot work properly without good force transmission and constraint performance. Many scholars have extensively studied the force performance of PMs. A new method based on pressure angle describes the force transmission and constraint properties of Delta PM [16]. Wang et al. [17] proposed a new index to assess the relationship between input and output forces. Static actuation force sensitivity was defined to measure the variation of driving forces with the manipulability of external force of the end-effector [18]. Utenov et al. [19] analysed the mapping from the constraint loads in the links to the distributed dynamic loads. Liang and Takeda [20] presented a new transmission index for force constraint evaluation based on the concept of pressure angle. It is widely known that a transmission wrench screw (TWS) transmits the motion and force between actuator and end-effector and a constraint wrench screw (CWS) resists structural deformations. They significantly influence the manipulability to transmit force and the consistency to resist deformations. However, most force transmission indices vary with the coordinate

\*Corr. Author's Address: South China University of Technology, School of Mechanical and Automotive Engineering, 381 Wushan Road, Tianhe District, Guangzhou, China, merobot@scut.edu.cn

frame, which may result in biased measure for the same PM due to the selection of different reference coordinate frames. Furthermore, the existing indices only measure the transmissibility of single limb but not a whole PM, and some of them are not homogeneous. However, relatively little literature on force constraint and the consistency to resist deformations could be found.

In this paper, a generalized approach to analysing and evaluating the manipulability to transmit force and the consistency to resist deformations of PM is put forward, in which two indices, namely the force transmission manipulability index (TMI) and the force constraint consistency index (CCI), are proposed. These two indices could be used independently or be used as an auxiliary index together with other performance evaluation indices to measure the force transmission and constraint performance of moving platforms in the process of design, motion planning and control of PMs.

This paper is organized as follows: in Section 1, the force balance is analysed, and two indices, namely TMI and CCI, are proposed. In Section 2, a generalized method to evaluate the manipulability to transmit force and the consistency to resist deformations of PM is proposed. The transmission matrix and the constraint matrix are firstly nondimensionalized, and the calculation formulas of TMI and CCI are presented respectively under three different compositions of transmission matrix and constraint matrix, with the frame invariance of the two indices being also proved. In Section 3, the distributions of TMI and CCI of the PMs with different mobility properties in the chosen spatial workspace are discussed, and the manipulability to transmit force and the consistency to resist deformations are analysed, based on which the configuration of a 3-CRU PM with optimal force transmission and constraint ability is constructed firstly. Section 4 summarizes three merits of the two indices, while Section 5 gives some additional remarks.

1 METHODS MANIPULABILITY TO TRANSMIT FORCE AND CONSISTENCY TO RESIST DEFORMATIONS

When the moving platform moves with constant velocity, the external six-dimension generalized force  $\mathbf{W}$  applied to the moving platform should balance with the actuated transmission force  $\mathbf{W}_F$  transmitted to the moving platform by actuated joint from each branch and the structural constraint force  $\mathbf{W}_C$  of PM in the equilibrium state of forces. For an  $n$ -DoF non-

redundant actuated PM with  $n$  actuated joints, the force balance equation is

$$\mathbf{W} = \mathbf{W}_F + \mathbf{W}_C. \tag{1}$$

In the process of force transmission, actuated transmission force  $\mathbf{W}_F$  is the resultant force of TWS transmitted to the moving platform through all branches, as shown in Fig. 1. Force diagrammatic sketch of PM, and  $\mathbf{W}_F$  can be denoted as

$$\mathbf{W}_F = \sum_{i=1}^n \mathbf{S}_{ai} = \sum_{i=1}^n f_i (\mathbf{s}_{f,i}; \mathbf{r}_{f,i} \times \mathbf{s}_{f,i} + h_{f,i} \mathbf{s}_{f,i}), \tag{2}$$

$i = 1, 2, \dots, n,$

where  $f_i$  is the magnitude of TWS  $\mathbf{S}_{ai}$  in terms of force,  $\mathbf{s}_{f,i}$  is the unit direction vector of  $\mathbf{S}_{ai}$  of the  $i$ th limb,  $\mathbf{r}_{f,i}$  is the vector of the force acting point in the global coordinate system, and  $h_{f,i}$  is the pitch of  $\mathbf{S}_{ai}$ .

In the process of force constraint, it is known that CWS is generated by mechanical structure. Assuming that there are  $C_i$  CWSs of each branch, as presented in Fig. 1. Force diagrammatic sketch of PM, the structural constraint force  $\mathbf{W}_C$  can be expressed as

$$\mathbf{W}_C = \sum_{i=1}^n \sum_{j=1}^{C_i} \mathbf{S}_{c,i,j} = \sum_{i=1}^n \sum_{j=1}^{C_i} c_{i,j} \left( \begin{matrix} \mathbf{s}_{c,i,j}; \\ \mathbf{r}_{c,i,j} \times \mathbf{s}_{c,i,j} + h_{c,i,j} \mathbf{s}_{c,i,j} \end{matrix} \right), \tag{3}$$

$i = 1, 2, \dots, n; \quad j = 1, 2, \dots, C_i,$

where  $c_{i,j}$  is the magnitude of CWS  $\mathbf{S}_{c,i,j}$  in terms of force;  $\mathbf{s}_{c,i,j}$  is the unit direction vector of  $\mathbf{S}_{c,i,j}$ ,  $\mathbf{r}_{c,i,j}$  is the vector of the force acting point in the global coordinate system, which is introduced as the physical centre of the passive end joint in the  $i$ th limb, and  $h_{c,i,j}$  is the pitch of  $\mathbf{S}_{c,i,j}$ .

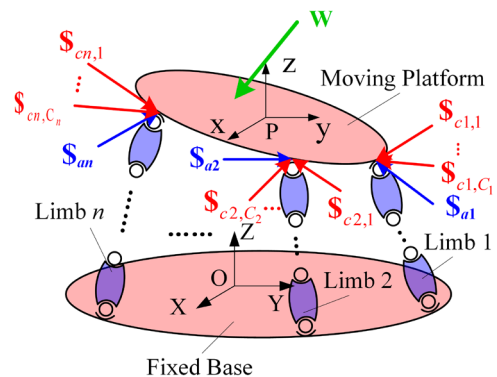


Fig. 1. Force diagrammatic sketch of PM

Eqs. (2) and (3) are respectively rewritten as

$$\mathbf{W}_F = \mathbf{Tf}, \tag{4}$$

$$\mathbf{W}_C = \mathbf{Rc}, \tag{5}$$

where  $\mathbf{f}=[f_1 \dots f_n]^T$  denotes the magnitude of the  $n$ -dimension force applied by the actuated joint to the moving platform through the branches,  $\mathbf{T}$  is the termed transmission matrix [21], and

$$\mathbf{T} = \begin{bmatrix} \mathbf{s}_1 & \mathbf{r}_1 \times \mathbf{s}_1 + h_1 \mathbf{s}_1 \\ \vdots & \vdots \\ \mathbf{s}_n & \mathbf{r}_n \times \mathbf{s}_n + h_n \mathbf{s}_n \end{bmatrix}_{n \times 6}^T. \quad (6)$$

$\mathbf{c}=[c_{1,1} \dots c_{1,C_1} \dots c_{n,1} \dots c_{n,C_n}]^T$  indicates the magnitude of  $6-n$  dimensional force to resist deformation through the structure of PM when the mechanism is subjected to forces in non-DoF direction.  $\mathbf{R}$  is the termed constraint matrix [21] and

$$\mathbf{R} = \begin{bmatrix} \mathbf{s}_{1,1} & \mathbf{r}_{1,1} \times \mathbf{s}_{1,1} + h_{1,1} \mathbf{s}_{1,1} \\ \vdots & \vdots \\ \mathbf{s}_{1,C_1} & \mathbf{r}_{1,C_1} \times \mathbf{s}_{1,C_1} + h_{1,C_1} \mathbf{s}_{1,C_1} \\ \vdots & \vdots \\ \mathbf{s}_{n,1} & \mathbf{r}_{n,1} \times \mathbf{s}_{n,1} + h_{n,1} \mathbf{s}_{n,1} \\ \vdots & \vdots \\ \mathbf{s}_{n,C_n} & \mathbf{r}_{n,C_n} \times \mathbf{s}_{n,C_n} + h_{n,C_n} \mathbf{s}_{n,C_n} \end{bmatrix}_{(6-n) \times 6}^T. \quad (7)$$

Obviously, the transmission force  $\mathbf{W}_F$  depends on the structure of branches and their geometrical arrangement and the constraint force  $\mathbf{W}_C$  on the stiffness of the PM (mainly its Young’s modulus as well as the lengths and sections of the elements). It should be pointed out that, although the producers of  $\mathbf{W}_F$  and  $\mathbf{W}_C$  are different, they can still exist simultaneously when the moving platform moves at a uniform velocity, which results in the aggregation of the two matrices in Eq. (1). Each row of these two matrices is just a force or a moment. The force and moment are simply combined into a sum screw according to spinor algebra.

**1.1 Force Transmission Manipulability Index**

From Eq. (6), it can be seen that transmission matrix  $\mathbf{T}$  is composed of TWS, which transmits the forces between actuators in joint space and the end-effectors in operational space. In order to evaluate the sensitivity of mutual disturbance in the process of force transmission,  $\mathbf{T}$  is decomposed by means of singular value decomposition (SVD). Assuming  $\mathbf{T}$  is homogeneous,

$$\mathbf{T} = \mathbf{U}\mathbf{\Sigma}\mathbf{V}^T, \quad (8)$$

where  $\mathbf{U}$  and  $\mathbf{V}$  are respectively  $n \times n$  and  $6 \times 6$  orthogonal matrices,  $\mathbf{\Sigma} = [\mathbf{\Sigma}_1 \mathbf{O}]_{n \times 6}$ , and  $\mathbf{\Sigma}_1 = \text{diag}(\sigma_1, \sigma_2, \dots, \sigma_n)$ , whose diagonal elements are arranged in the order of  $\sigma_1 \geq \sigma_2 \geq \dots \geq \sigma_n > 0$ .  $\sigma_1, \sigma_2, \dots, \sigma_n$  denote the singular values of  $\mathbf{T}$ .  $\mathbf{O}$  denotes zero matrix.

Post-multiply both sides of Eq. (8) by matrix  $\mathbf{V}^{-T}\mathbf{\Sigma}^+$ , then

$$\mathbf{T}\mathbf{V}^{-T}\mathbf{\Sigma}^+ = \mathbf{U}, \quad (9)$$

where  $\mathbf{\Sigma}^+$  is the pseudo inverse matrix of the diagonal matrix  $\mathbf{\Sigma}$ , and  $\mathbf{\Sigma}^+ = \begin{bmatrix} \mathbf{\Sigma}_1^{-1} \\ \mathbf{O} \end{bmatrix}_{6 \times n}$  with

$$\mathbf{\Sigma}_1^{-1} = \text{diag}(1/\sigma_1, 1/\sigma_2, \dots, 1/\sigma_n).$$

Rewrite matrix  $\mathbf{V}^{-T}\mathbf{\Sigma}^+$  as

$$\mathbf{V}^{-T}\mathbf{\Sigma}^+ = (\tilde{\mathbf{v}}_1/\sigma_1 \quad \dots \quad \tilde{\mathbf{v}}_n/\sigma_n), \quad (10)$$

where  $\tilde{\mathbf{v}}_n$  represents the  $n^{\text{th}}$  column of matrix  $\mathbf{V}^{-T}$ .

From the physical meaning of SVD, it can be seen that  $f_n = \|\tilde{\mathbf{v}}_n/\sigma_n\|$ . Combined with Eq. (4), the following equation exists:

$$\mathbf{W}_F = \mathbf{T}\mathbf{f} = \mathbf{T} \begin{pmatrix} f_1 \\ \vdots \\ f_n \end{pmatrix} = \mathbf{T} \begin{pmatrix} \|\tilde{\mathbf{v}}_1/\sigma_1\| \\ \vdots \\ \|\tilde{\mathbf{v}}_n/\sigma_n\| \end{pmatrix}. \quad (11)$$

Then, the “elastic” ratio  $\Gamma$  can be defined as the 2-norm ratio of  $\mathbf{f}$  to  $\mathbf{W}_F$ , that is,

$$\Gamma = \frac{\|\mathbf{W}_F\|}{\|\mathbf{f}\|} = \frac{1}{\sqrt{\sum_{i=1}^n 1/\sigma_i^2}}. \quad (12)$$

The physical meaning of  $\Gamma$  is the “elastic” length after  $\mathbf{f}$  in joint space is rotation-, scaling- and projection-transformed into  $\mathbf{W}_F$  in operational space, which reflects the manipulability of actuated force. Thus, it can be called as force transmission manipulability ratio.  $\Gamma$  ranges from 0 to  $\Gamma_{\max}$ . When all  $\sigma_i$  are equal each other,  $\Gamma$  equals to the maximum, and the force transmission manipulability behaves the best; When  $\Gamma$  is close to 0, the force transmission manipulability behaves the worst and then force transmission singularity may occur.

To normalize the ratio, by comparing and measuring  $\Gamma$  in different poses intuitively, force transmission manipulability index (TMI) is defined as

$$\rho_\Gamma = \Gamma/\Gamma_{\max}. \quad (13)$$

The closer  $\rho_\Gamma$  gets to 1, the less distortion  $\mathbf{f}$  has, which means that the TWSs exerted on the moving platform have no distortion and that the manipulability

of transmission force is excellent. When  $\rho_\Gamma$  approaches zero,  $\mathbf{f}$  extends or shrinks to infinity after the transformation, and actuation singularity is encountered.

**1.2 Force Constraint Consistency Index**

Constraint matrix  $\mathbf{R}$  is composed of CWS, which counterbalances the external forces and resists deformations. The SVD and relevant derivation process of the homogeneous constraint matrix  $\mathbf{R}$  is similar to  $\mathbf{T}$ , and the force constraint consistency ratio can be expressed as

$$\Omega = \frac{\|\mathbf{W}_c\|}{\|\mathbf{c}\|} = \frac{1}{\sqrt{\sum_{i=1}^{6-n} 1/\sigma_i^2}}. \tag{14}$$

Force constraint consistency index (CCI) is expressed as

$$\rho_\Omega = \Omega/\Omega_{\max}. \tag{15}$$

The closer  $\rho_\Omega$  is to 1, the more stable  $\mathbf{c}$  is, which means that the CWSs exerted on the moving platform have less “elastic” change and basically keep consistent, and that the consistency of force constraint is excellent. When  $\rho_\Omega$  is near to zero,  $\mathbf{c}$  extends or shrinks to infinity after the transformation, and constraint singularity is encountered.

**2 SOLUTION OF FORCE TRANSMISSION MANIPULABILITY RATIO AND CONSTRAINT CONSISTENCY RATIO**

To calculate  $\Gamma_{\max}$  and  $\Omega_{\max}$ ,  $\mathbf{T}$  and  $\mathbf{R}$  need to be solved first. In this section, the corresponding calculation models of  $\Gamma_{\max}$  and  $\Omega_{\max}$  are discussed based on the possible composition of the transmission matrix  $\mathbf{T}$  and constraint matrix  $\mathbf{R}$  presented in Table 1. Then,  $\rho_\Gamma$  and  $\rho_\Omega$  in six cases are respectively derived.

**Table 1.** The possible composition of the transmission matrix and constraint matrix

	Transmission matrix $\mathbf{T}$	Constraint matrix $\mathbf{R}$
Only composed of linear force vectors	Section 2.2.1	Section 2.3.1
Only composed of force couples	Section 2.2.2	Section 2.3.2
Composed of both linear force vectors and force couples	Section 2.2.3	Section 2.3.3

**2.1 Homogenization of Transmission Matrix and Constraint Matrix**

When  $\mathbf{T}$  and  $\mathbf{R}$  are composed of only linear force vectors or both linear force vectors and force couples, the dimensions of the left three columns and the right three columns elements of  $\mathbf{T}$  and  $\mathbf{R}$  are different. Therefore, these two matrices should be homogenized before SVD.

**2.1.1 Homogeneous Transmission Matrix**

The three right column elements of  $\mathbf{T}$  are multiplied by a characteristic length  $L_\xi$  [22] to unify the dimension. In this case, the homogeneous transmission matrix  $\mathbf{T}_h$  is

$$\mathbf{T}_h = [\mathbf{T}_1 \quad \mathbf{T}_2/L_\xi], \tag{16}$$

where  $\mathbf{T}_1 = [\mathbf{s}_1 \dots \mathbf{s}_n]^T$ , and  $\mathbf{T}_2 = [(\mathbf{r}_1 \times \mathbf{s}_1) \dots (\mathbf{r}_n \times \mathbf{s}_n)]^T$ , the isotropy condition for  $\mathbf{T}_h$  is

$$\mathbf{T}_h^T \mathbf{T}_h = \begin{bmatrix} \mathbf{T}_1^T \mathbf{T}_1 & (\mathbf{T}_1^T \mathbf{T}_2)/L_\xi \\ (\mathbf{T}_2^T \mathbf{T}_1)/L_\xi & (\mathbf{T}_2^T \mathbf{T}_2)/L_\xi^2 \end{bmatrix} = \sigma_\xi^2 \mathbf{I}, \tag{17}$$

where  $\sigma_\xi > 0$  is a nondimensional scalar and  $\mathbf{I}$  is a 6×6 identity matrix. When  $\mathbf{T}_h$  is isotropic, the singular values of  $\mathbf{T}_h$  are identical. At this time, the PM has at least one configuration in the whole workspace [21]. Furthermore, if  $\mathbf{T}_h$  does not satisfy the isotropy condition, i.e., the PM cannot reach an isotropy configuration, it is necessary to seek a configuration over the whole workspace in which the condition number reaches the minimum.

Based on the Frobenius norm, the condition number of  $\mathbf{T}_h$  is calculated as [23]

$$\kappa(\mathbf{T}_h) = \|\mathbf{T}_h\|_F \|\mathbf{T}_h^{-1}\|_F = \frac{1}{6} \sqrt{\text{tr}(\mathbf{T}_h^T \mathbf{T}_h) \text{tr}[(\mathbf{T}_h^T \mathbf{T}_h)^{-1}]}. \tag{18}$$

To solve  $L_\xi$ ,  $\kappa^2(\mathbf{T}_h)$  is minimized. Thus, the objective function subjected to the corresponding geometric constraints is

$$\min_x \kappa^2(\mathbf{T}_h). \tag{19}$$

The design vector  $\mathbf{x}$  is related to configuration variables  $\Phi$  of end-effector and  $L_\xi$ , namely  $\mathbf{x} = [\Phi \ L_\xi]$ . Therefore, the above solution can be represented as

$$\begin{aligned} & \underset{\mathbf{x}}{\text{minimize}} \quad \kappa^2(\mathbf{T}_h) \\ & \text{subject to} \quad \Phi \in \mathbf{S} \end{aligned}, \tag{20}$$

where  $\mathbf{S}$  denotes the workspace of the PM.

By computing the optimization problem, the characteristic length  $L_\xi$  can be obtained, thus obtaining

the homogeneous transmission matrix  $\mathbf{T}_h$ . For the sake of simplicity, the dimensionless coefficient of transmission matrix and constraint matrix here are derived only by taking the linear force vector as an example. When the matrix is composed of both linear force vectors and force couples, the deduction process is similar.

**2.1.2 Homogeneous Constraint Matrix**

Similarly, to unify the dimension of  $\mathbf{R}$ , a characteristic length  $L_\eta$  is calculated by

$$\begin{aligned} & \underset{x}{\text{minimize}} \quad \kappa^2(\mathbf{R}_h) \\ & \text{subject to} \quad \Phi \in \mathbf{S} \end{aligned} \quad (21)$$

where  $\kappa(\mathbf{R}_h) = \frac{1}{6} \sqrt{\text{tr}(\mathbf{R}_h^T \mathbf{R}_h) \text{tr}[(\mathbf{R}_h^T \mathbf{R}_h)^{-1}]}$  and  $\mathbf{R}_h$  is represented by  $L_\eta$ .

**2.2 Calculation Formula of TMI**

**2.2.1 Transmission Matrix Composed of linear Force Vectors**

When  $\mathbf{T}$  is only composed of linear force vectors, the dimensionless transmission matrix  $\mathbf{T}_h$  is

$$\mathbf{T}_h = \begin{bmatrix} \mathbf{s}_1 & (\mathbf{r}_1 \times \mathbf{s}_1) / L_\xi \\ \vdots & \vdots \\ \mathbf{s}_n & (\mathbf{r}_n \times \mathbf{s}_n) / L_\xi \end{bmatrix}^T. \quad (22)$$

The trace of matrix  $\mathbf{T}_h^T \mathbf{T}_h$  is solved as  $\text{tr}(\mathbf{T}_h^T \mathbf{T}_h) = \sum_{i=1}^n \sigma_i^2 = n + \sum_{i=1}^n \frac{1}{L_\xi^2} (\mathbf{r}_i \times \mathbf{s}_i)^2$ . When  $\sigma_i^2 = k/n$ , the transmission manipulability ratio  $\Gamma$  achieves the maximum  $\sqrt{k/n}$ . Therefore, TMI can be calculated by

$$\rho_\Gamma = \frac{n}{\sqrt{(n + \sum_{i=1}^n \frac{1}{L_\xi^2} \|\mathbf{r}_i \times \mathbf{s}_i\|^2) \sum_{i=1}^n \frac{1}{\sigma_i^2}}}. \quad (23)$$

**2.2.2 Transmission Matrix Composed of Force Couples**

When  $\mathbf{T}$  is only composed of force couples, TMI can be calculated as

$$\rho_\Gamma = \sqrt{\frac{n}{\sum_{i=1}^n \frac{1}{\sigma_i^2}}}. \quad (24)$$

**2.2.3 Transmission Matrix Composed of Linear Force Vectors and Force Couples**

When  $\mathbf{T}$  is composed of  $m$  linear force vectors and  $n-m$  force couples, TMI is

$$\rho_\Gamma = \frac{n}{\sqrt{(n + \sum_{i=1}^m (\frac{1}{L_\xi^2} \|\mathbf{r}_i \times \mathbf{s}_i\|^2) \sum_{i=1}^n \frac{1}{\sigma_i^2}}}. \quad (25)$$

**2.3 Calculation Formula of CCI**

**2.3.1 Constraint Matrix Composed of Linear Force Vectors**

When  $\mathbf{R}$  is only composed of linear force vectors, CCI can be calculated as

$$\rho_\Omega = \frac{6-n}{\sqrt{\left( \sum_{i=1}^{6-n} C_i + \sum_{i=1}^{6-n} \sum_{j=1}^{C_i} \frac{1}{L_\eta^2} (\mathbf{r}_{i,j} \times \mathbf{s}_{i,j})^2 \right) \sum_{i=1}^{6-n} 1/\sigma_i'^2}}. \quad (26)$$

It should be noted that there are  $\sum_{i=1}^n \sum_{j=1}^{6-C_i} j$  ( $j=1, 2, \dots, 6-C_i$ ,  $i=1, 2, \dots, n$ ) CWSs. The  $6-n$  DoFs of the moving platform are constrained by these CWSs, that is  $\text{rank}(\mathbf{R}_h) = 6-n$ . It is only necessary to pick up  $6-n$  linearly independent screws from these  $\sum_{i=1}^n \sum_{j=1}^{6-C_i} j$  CWSs to compose the constraint matrix.

**2.3.2 Constraint Matrix Composed of Force Couples**

When  $\mathbf{R}$  is only composed of force couples, CCI can be obtained as

$$\rho_\Omega = \frac{6-n}{\sqrt{\sum_{i=1}^{6-n} C_i \sum_{i=1}^{6-n} 1/\sigma_i'^2}}. \quad (27)$$

**2.3.3 Constraint Matrix Composed of Linear Force Vectors and Force Couples**

When  $\mathbf{R}$  is composed of  $\sum_{i=1}^n m_i$  linear force vectors and  $\sum_{i=1}^n (C_i - 2m_i)$  force couples, CCI can be calculated as

$$\rho_\Omega = \frac{6-n}{\sqrt{\left( \sum_{i=1}^{6-n} C_i + \sum_{i=1}^{6-n} (\frac{1}{L_\eta^2} \|\mathbf{r}_{i,j} \times \mathbf{s}_{i,j}\|^2) \right) \sum_{i=1}^{6-n} 1/\sigma_i'^2}}. \quad (28)$$

### 2.4 Frame Invariance of TMI and CCI

Assuming that the transmission force is expressed by  $\mathbf{W}_F$  in a coordinate system  $\{O\}$ , in another coordinate system  $\{O'\}$ , the same transmission force is represented by  $\mathbf{W}'_F$ . The relationship between the forces in different coordinate frame can be expressed as

$$(\mathbf{W}'_F)^T = \mathbf{Ad}_g \mathbf{W}_F^T, \tag{29}$$

where  $\mathbf{Ad}_g$  is transformation matrix.

Then  $\mathbf{W}'$  can be calculated by

$$(\mathbf{T}')^T = \mathbf{Ad}_g \mathbf{T}^T \mathbf{Ad}_g^{-1}. \tag{30}$$

By rewriting Eq. (8) into the form of column vector, namely

$$\sigma_i \mathbf{v}_i^T = \mathbf{T}^T \mathbf{u}_i^T \quad i = 1, 2, \dots, n, \tag{31}$$

and pre-multiplying both sides of Eq. (31) by the matrix  $\mathbf{Ad}_g$ , it can be obtained as

$$\sigma_i (\mathbf{v}'_i)^T = \mathbf{Ad}_g \mathbf{T}^T \mathbf{Ad}_g^{-1} (\mathbf{u}'_i)^T, \tag{32}$$

where  $(\mathbf{v}'_i)^T = \mathbf{Ad}_g \mathbf{v}_i^T$  and  $(\mathbf{u}'_i)^T = \mathbf{Ad}_g \mathbf{u}_i^T$ . In other words, vectors  $\mathbf{v}_i^T$  and  $\mathbf{u}_i^T$  in the frame  $\{O\}$  are transformed into  $(\mathbf{v}'_i)^T$  and  $(\mathbf{u}'_i)^T$  in the frame  $\{O'\}$ , respectively.

Substituting Eq. (30) into Eq. (32) yields

$$\sigma_i (\mathbf{v}'_i)^T = (\mathbf{T}')^T (\mathbf{u}'_i)^T. \tag{33}$$

Comparing Eq. (31) with Eq. (33), it can be seen that the singular values of  $\mathbf{T}'$  and  $\mathbf{T}$  are identical in different coordinate frames. The coordinate transformation of the transmission matrix does not affect its singular value. In the same way, it can be proved that constraint matrix  $\mathbf{R}$  also has this property. From Eqs. (12) and (13), it can be seen that neither TMI nor CCI varies with the reference coordinate frame. This property is called the frame invariance of TMI and CCI.

### 3 MANIPULABILITY OF TRANSMISSION FORCE AND CONSISTENCY OF CONSTRAINT FORCE ANALYSIS OF PMS WITH DIFFERENT MOBILITY PROPERTIES

In this section, TMI and CCI for several typical PMs will be calculated to illustrate the usage of the two indices as well as the manipulability to transmit force and the consistency to resist deformations of the PMs.

### 3.1 4-URU Three-Translational and One-Rotational PM with Mixed-Motion

The sketch of 4-URU PM [24] are shown in Fig. 2. The mobility properties are three translational DoFs and one rotational DoF around the z-axis. The rotation angle of the moving platform around z-axis is represented by  $\alpha$ . The horizontal revolute joint of the universal joint  $A_i$  is actuated.

The moving platform of the 4-URU PM is exerted by four constraint couples from four branches, and the constraint matrix is

$$\mathbf{R}_0 = [\mathbf{s}_{r1}^T \quad \mathbf{s}_{r2}^T \quad \mathbf{s}_{r3}^T \quad \mathbf{s}_{r4}^T], \tag{34}$$

where  $\mathbf{s}_{ri}(i=1,2,3,4)$  denotes the direction vectors of the constraint couples, which are in parallel with the plane of the moving platform.

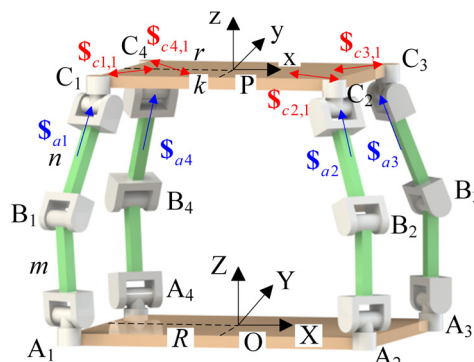


Fig. 2. Sketch of 4-URU PM

Since the four constraint couples are all in one plane,  $\mathbf{R}_0(:,3) = \mathbf{0}$ . In addition, only two force couples are linearly independent based on the dependence of screw system [25]. That is to say,  $\mathbf{s}_{r3}^T$  and  $\mathbf{s}_{r4}^T$  can be linearly represented by  $\mathbf{s}_{r1}^T$  and  $\mathbf{s}_{r2}^T$ . Therefore, the constraint matrix is rewritten as

$$\mathbf{R}_h = \begin{bmatrix} \mathbf{R}_0(1,1:2) \\ \mathbf{R}_0(2,1:2) \end{bmatrix}. \tag{35}$$

Obviously,  $\mathbf{R}_h$  is homogeneous matrix.

When the actuated joints are locked, the transmission matrix is

$$\mathbf{T}_0 = \begin{bmatrix} \mathbf{r}_{a1} \times \mathbf{s}_{a1} & \mathbf{s}_{a1} \\ \mathbf{r}_{a2} \times \mathbf{s}_{a2} & \mathbf{s}_{a2} \\ \mathbf{r}_{a3} \times \mathbf{s}_{a3} & \mathbf{s}_{a3} \\ \mathbf{r}_{a4} \times \mathbf{s}_{a4} & \mathbf{s}_{a4} \end{bmatrix}^T, \tag{36}$$

where  $\mathbf{r}_{ai}$  represents the vector of acting point of TWS  $\mathbf{S}_i^a$  in fixed coordinate frame  $\{O\}$ .  $\mathbf{s}_{ai}$  denotes the direction vectors of the transmission forces.

From the mobility of the PM, the homogeneous transmission matrix can be written as

$$\mathbf{T}_h = [\mathbf{T}_p/L_\xi \quad \mathbf{T}_o], \quad (37)$$

where  $\mathbf{T}_p = \begin{bmatrix} \mathbf{T}_0(1,3) \\ \mathbf{T}_0(2,3) \\ \mathbf{T}_0(3,3) \\ \mathbf{T}_0(4,3) \end{bmatrix}$  and  $\mathbf{T}_o = \begin{bmatrix} \mathbf{T}_0(1,4:6) \\ \mathbf{T}_0(2,4:6) \\ \mathbf{T}_0(3,4:6) \\ \mathbf{T}_0(4,4:6) \end{bmatrix}$ .

The condition number of  $\mathbf{T}_h$  is calculated based on Eq. (18), i.e.,

$$\kappa(\mathbf{T}_h) = \|\mathbf{T}_h\|_F \|\mathbf{T}_h^{-1}\|_F = \frac{1}{4} \sqrt{\text{tr}(\mathbf{T}_h^T \mathbf{T}_h) \text{tr}[(\mathbf{T}_h^T \mathbf{T}_h)^{-1}]}. \quad (38)$$

To obtain the minimum values of  $\kappa(\mathbf{T}_h)$  and  $L_\xi$  of the isotropic configuration, the problem becomes

$$\begin{aligned} & \underset{\mathbf{x}}{\text{minimize}} && \kappa^2(\mathbf{T}_h) \\ & \text{subject to} && \Phi \in \mathbf{S} \end{aligned} \quad (39)$$

To determine the optimum solution of problem (39), the structure parameters of the 4-URU PM are given as  $R=500$  mm,  $r_1=400$  mm,  $r_2=300$  mm,  $m=700$  mm and  $n=800$  mm, the initial design vector  $\mathbf{x}$  including both  $\Phi$  and  $L_\xi$  is assigned as  $\mathbf{x}_{\text{init}}=[100 \ 100 \ 1200 \ 300]^T$  and the ‘‘interior-point’’ algorithm is adopted, thus obtaining  $\mathbf{x}_{\text{opt}}=[-25.37 \ 207.72 \ 893.57 \ 723.14]^T$ . The fourth element denotes the characteristic length, i.e.,  $L_\xi=723.14$  mm. By using this value to homogenize the transmission matrix, the minimum condition number is calculated as  $\kappa_{\text{min}}=1.00$ , which means that the characteristic length is available.

By respectively substituting Eqs. (37) and (35) into Eqs. (27) and (23), the equations of TMI and CCI can be deduced as

$$\rho_\Gamma = \frac{4}{\sqrt{(4 + \sum_{i=1}^4 \frac{1}{L_\xi^2} \mathbf{T}_0(i,3)^2) \sum_{i=1}^n \frac{1}{\sigma_i^2}}}, \quad (40)$$

$$\rho_\Omega = \frac{\sqrt{2}}{\sqrt{\sum_{i=1}^2 1/\sigma_i'^2}}, \quad (41)$$

where  $\sigma_i$  and  $\sigma'$  are singular values of matrix  $\mathbf{T}_h$  and  $\mathbf{R}_h$ , respectively.

Based on Eqs. (40) and (41), the distributions of TMI and CCI in the chosen spatial workspace are obtained when the rotation angle of the moving platform around z-axis is  $0^\circ$ , as shown in Fig. 3. The values of TMI and CCI are presented in Table 2. The maximum and minimum of TMI are computed as 0.43

and 0, and the maximum and minimum of CCI are 1 and 0.02, respectively.

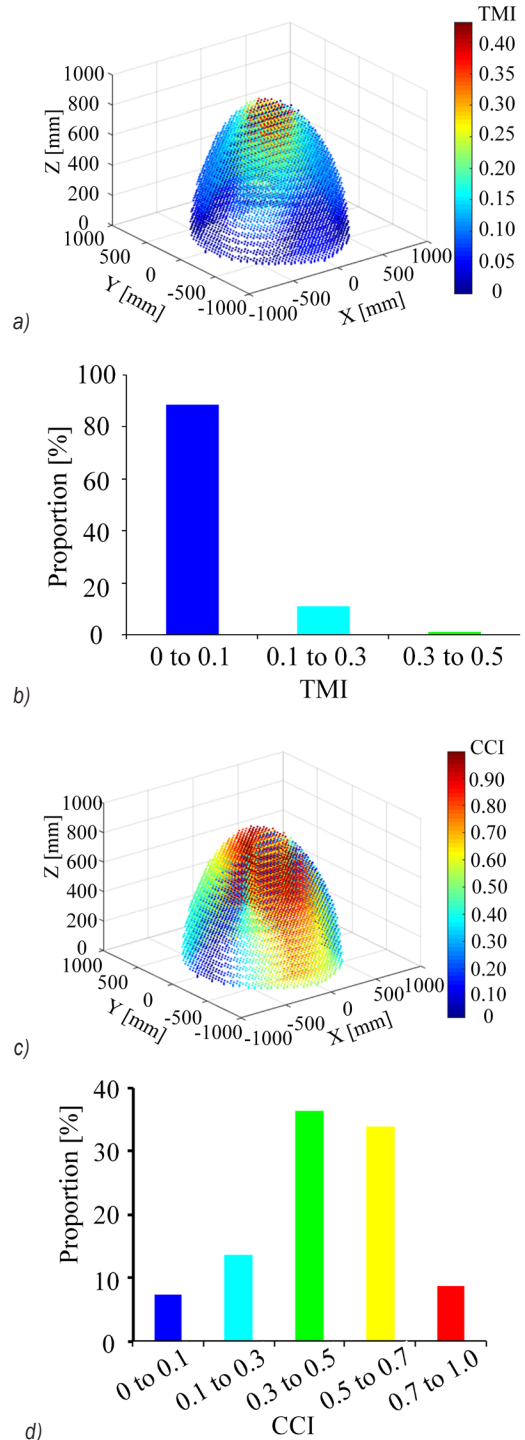
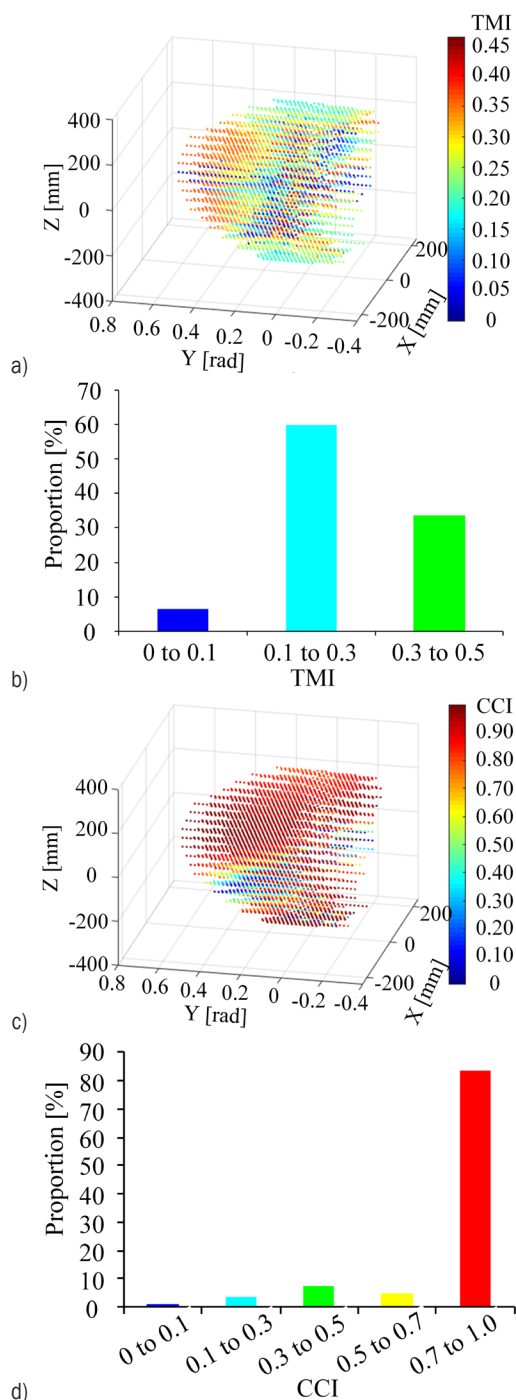


Fig. 3. a) Distribution of the TMI of 4-URU PM when  $\alpha=0^\circ$ , b) proportion of TMI values in each interval, c) distribution of the CCI of 4-URU PM when  $\alpha=0^\circ$ , and d) proportion of CCI values in each interval



**Fig. 4.** a) Distribution of the TMI of 4-URU PM when  $z_p=900$  mm, b) proportion of TMI values in each interval, c) distribution of the CCI of 4-URU PM when  $z_p=900$  mm, and d) proportion of CCI values in each interval

Fig. 3a illustrates that the closer the centre point P of the moving platform to z-axis, the larger the TMI and the less “elastic” variation of the TWSs applied to the moving platform. On the whole, the majority of

TMI in the chosen spatial workspace is less than 0.1 (see Fig. 3b), meaning that the manipulability of the TWSs is sharply changed and is nearly close to the singularity when  $\alpha=0^\circ$ . However, CCI is more than 0.5 in most areas of the chosen spatial workspace (see Figs. 3c and d), meaning that the CWSs exerted on the moving platform have less “elastic” variation when the moving platform moves in translational direction. The consistency of the CWS to resist the deformations is moderate.

**Table 2.** The values of the proposed parameters of 4-URU PM when  $\alpha=0^\circ$

	TMI	CCI
Maximum	0.43	1
Minimum	0	0.02
Proportion of each interval	0 to 0.1	88.34 %
	0.1 to 0.3	10.79 %
	0.3 to 0.5	0.87 %
	0.5 to 0.7	0
	0.7 to 1.0	0

**Table 3.** The values of the proposed parameters of 4-URU PM when  $z_p=900$  mm

	TMI	CCI
Maximum	0.46	1
Minimum	0	0
Proportion of each interval	0 to 0.1	6.40 %
	0.1 to 0.3	59.95 %
	0.3 to 0.5	33.64 %
	0.5 to 0.7	0
	0.7 to 1.0	0

Fig. 4 shows the distributions of TMI and CCI in the chosen spatial workspace when the translational DoF of the moving platform along z-axis is fixed ( $z_p = 900$  mm). The corresponding values of TMI and CCI are presented in Table 3. The maximum of TMI is 0.46 and the minimum is 0. The maximum of CCI is 1 and the minimum is 0. As shown in Fig. 4a, the larger the angle along y-axis, the larger the TMI and the less the “elastic” variation of the TWSs exerted on the moving platform. Moreover, as shown in Fig. 4b, most TMI values in the chosen spatial workspace vary from 0.1 to 0.5. Consequently, by comparing Fig. 3. with Fig. 4, it can be seen that the manipulability variation of the TWSs with  $0^\circ$  of the rotation angle of the moving platform around z-axis is less than that with fixed translational DoF of the moving platform along z-axis. In addition, CCI is more than 0.7 in most areas of the chosen spatial workspace (see Figs. 4c and d), which means that, when the moving platform moving

along z-axis is fixed, the CWSs exerted on the moving platform is of less distortion and the consistency of force constraint behaves well.

### 3.2 2-UPR+SPR Two-Rotational and One-Translational PM with Parasitic Motion

The 2-UPR+SPR (P a prismatic joint; S a spherical joint.) PM possesses two rotational DoFs round x-axis and y-axis and one translational DoF along z-axis, which is well known as the positioning module of the Exechon parallel machine tool [26]. The rotation angle of the moving platform around x-axis and y-axis are represented by  $\alpha$  and  $\beta$ , respectively. The sketch is established as presented in Fig. 5. The prismatic joint  $B_i$  is actuated.

The equations of TMI and CCI is

$$\rho_r = \frac{3}{\sqrt{(3 + \sum_{i=1}^3 \sum_{j=1}^2 \frac{1}{L_\xi^2} \mathbf{T}_0(i, j)^2) \sum_{i=1}^3 \frac{1}{\sigma_i^2}}}, \quad (42)$$

$$\rho_\Omega = \frac{3}{\sqrt{(3 + \sum_{i=1}^3 \frac{1}{L_\eta^2} \mathbf{R}_0(i, 3)^2) \sum_{i=1}^3 \frac{1}{\sigma_i^2}}}, \quad (43)$$

where the characteristic length  $L_\xi = 353.55$  and  $L_\eta = 483.80$  according to the computing analysis.

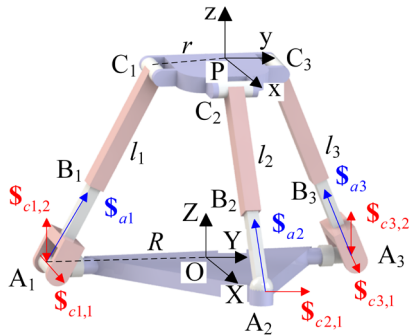


Fig. 5. Sketch of 2-UPR+SPR PM

Fig. 6 shows the distributions of TMI and CCI of 2-UPR+SPR PM in the chosen spatial workspace. The corresponding values of TMI and CCI are presented in Table 4. The computed TMI ranges from 0.36 to 1.00, and the computed CCI ranges from 0.26 to 0.62. As shown in Figs. 6a and b, TMI is more than 0.7 in most areas of the workspace, and the TWSs exerted on the moving platform are of less distortion, which means that the manipulability of transmission force is moderate.

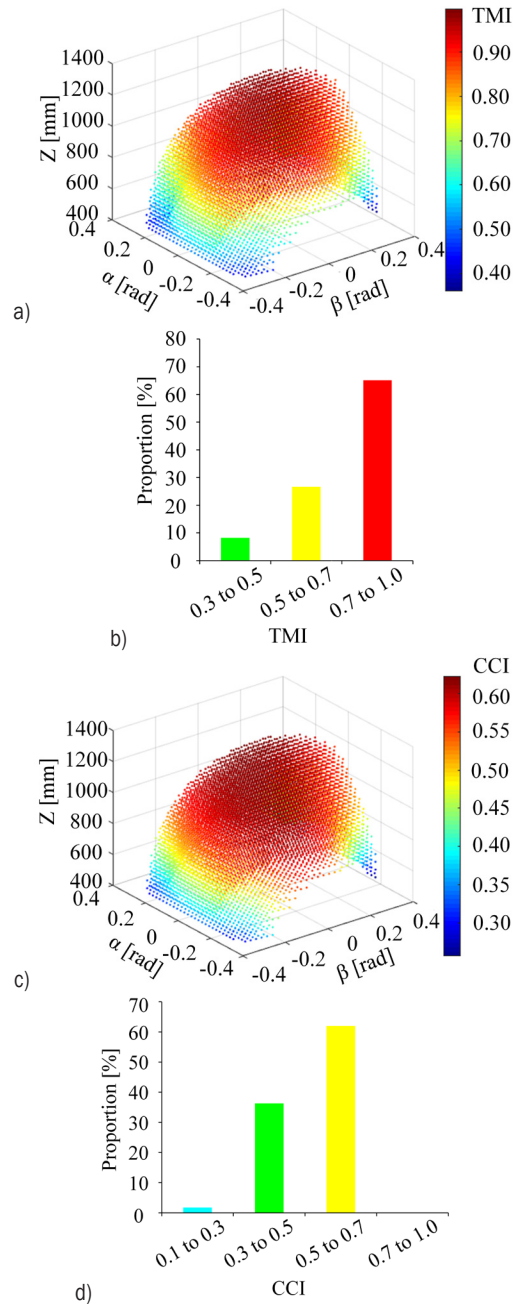


Fig. 6. a) Distribution of the TMI of 2-UPR+SPR PM, b) proportion of TMI values in each interval, c) distribution of the CCI of 2-UPR+SPR PM, and d) proportion of CCI values in each interval

Similar with TMI, the majority of CCI is up to 0.50 (see Figs. 6c and d), and the CWSs exerted on the moving platform are also of less “elastic” variation, meaning that the consistency of force constraint is moderate. Furthermore, due to the parasitic motion of the mechanism [27], that is, during its rotation around x-axis and y-axis, the moving platform translates along x-axis and y-axis at the same time. Thus, the

translation DoFs along x-axis and y-axis are not constrained, which brings great difficulty to the control algorithm of the PM. In addition, the existence of the parasitic motion also makes the kinematics calibration of PM very difficult. Parasitic motion is an inherent characteristic of PM and cannot be compensated by its own control system, so that it is often minimized via structural optimization design.

### 3.3 3-CRU Three-Translational PM with Pure Motion

Fig. 7 shows the sketch of a 3-CRU PM [28] with three translational DoFs. The translation of the cylindrical joint  $A_i$  is actuated.

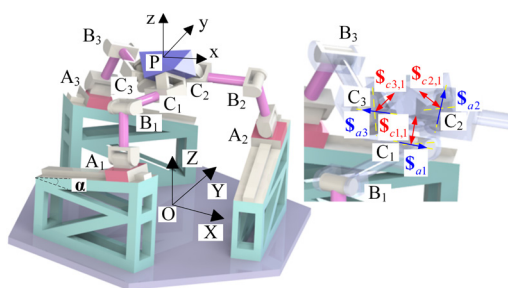


Fig. 7. Sketch of 3-CRU PM

properties of the PM determine that the revolute joint connected with the platform is an inactive joint (The inactive joint reduces the over-constraint of the PM). Thus, the constraint force couple also remains constant, namely, the constraint matrix remains constant. From above-mentioned analysis, it can be found that the transmission linear force vector is only related to the angle  $\alpha$  between the slide rail and the base plane. In addition to  $\alpha$ , the transmission force couple also depends on the angle  $\beta$  between the edge of the platform and the axis of the R joint  $B_i$ . Fig. 8 illustrates these two angles.

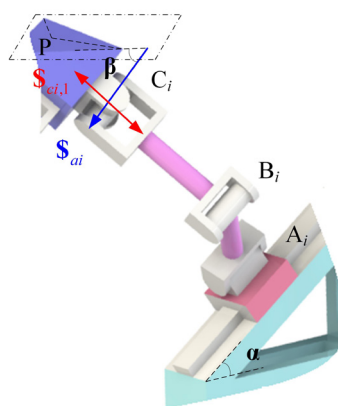


Fig. 8.  $\alpha$  and  $\beta$  of the  $i$ th branch

Then, TMI and CCI can respectively be calculated by

$$\rho_r = \frac{\sqrt{3}}{\sqrt{\sum_{i=1}^3 1/\sigma_i^2}} \quad (44)$$

$$\rho_\Omega = \frac{\sqrt{3}}{\sqrt{\sum_{i=1}^3 1/\sigma_i'^2}} \quad (45)$$

Table 4. The values of the proposed parameters of 2-UPR+SPR PM

	TMI	CCI	
Maximum	0.36	0.26	
Minimum	1.00	0.62	
Proportion of each interval	0 to 0.1	0	
	0.1 to 0.3	0	
	0.3 to 0.5	8.21 %	36.28 %
	0.5 to 0.7	26.67 %	61.97 %
	0.7 to 1.0	65.12 %	0

The direction of TWS is parallel with the slide rail and remains constant [28], that is, the transmission matrix remains constant. In addition, the direction of constraint force couple is perpendicular to both axes of the universal joint  $C_i$ . The kinematic and constraint

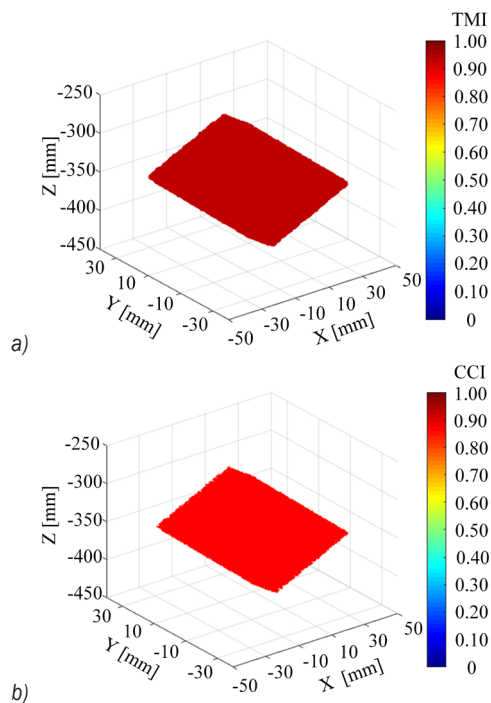
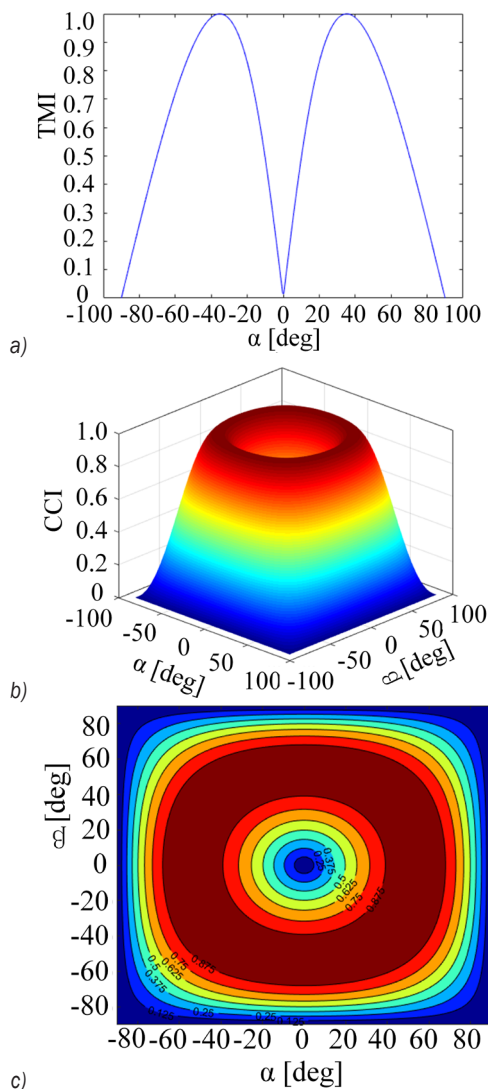


Fig. 9. a) Distribution of the TMI of 3-CRU PM when  $\alpha = 25^\circ$  and  $\beta = 30^\circ$ , and b) distribution of the CCI of 3-CRU PM when  $\alpha = 25^\circ$  and  $\beta = 30^\circ$

When  $\alpha=25^\circ$  and  $\beta=30^\circ$ , the distributions of TMI and CCI in the chosen spatial workspace can be obtained, as shown in Fig. 9. The workspace of 3-CRU PM is a regular hexahedron. The TMI and CCI of 3-CRU PM remain constant with values of 0.93 and 0.86, respectively. TMI is close to the maximum, which means that the TWSs exerted on the moving platform are almost same as that in the joint space when  $\alpha=25^\circ$ . However, although CCI is slightly smaller than TMI, the distortion of CWSs exerted on the platform does not change that much. Angles  $\alpha$  and  $\beta$  have influence on the force transmission manipulability and force constraint consistency of 3-CRU PM. Fig. 10 illustrates the relationship among TMI, CCI,  $\alpha$  and  $\beta$ .



**Fig. 10.** a) Relationship between TMI and  $\alpha$ ,  
 b) relationship between CCI and  $\alpha$  as well as  $\beta$ ,  
 c) contour of the relationship between CCI and  $\alpha$  as well as  $\beta$

In Fig. 10a, TMI has a rapid increase with  $\alpha$  when  $\alpha \in [0^\circ, 35.26^\circ]$ . When  $\alpha=35.26^\circ$ , the index reaches the maximum and the TWSs exerted on the moving platform have no distortion, which means that the manipulability of transmission force is excellent. From Figs. 10b and c, it can be determined that the curved surface is on  $\alpha=0^\circ$  and  $\beta=0^\circ$  symmetry. When  $\alpha \in [39.00^\circ, 68.00^\circ]$  and  $\beta \in [39.00^\circ, 68.00^\circ]$ , CCI is more than 0.88. That is to say, the CWSs exerted on the moving platform have less distortion. It should be noted that TMI and CCI equal to 1 and reach the maximum at the same time when  $\alpha=35.26^\circ$  and  $\beta=45^\circ$ , which means that the transmission force vector and constraint force couple both have no “elastic” variation. The manipulability of transmission force and the consistency of constraint force are excellent and do not vary with the pose. The structural configuration of the PM corresponding to this case is presented in Fig. 11.

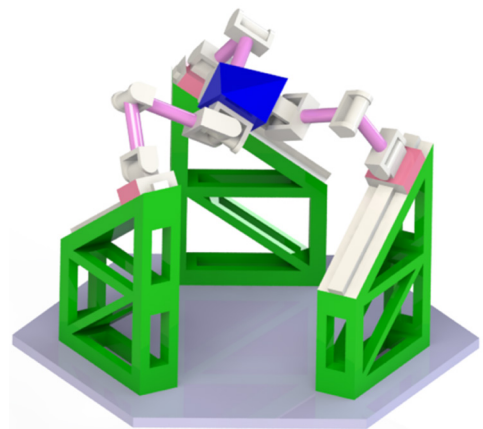


**Fig. 11.** Structural configuration of the 3-CRU PM when TMI=1 and CCI=1

#### 4 MERITS OF TMI AND CCI

In summary, as compared with some other evaluation indices based on Jacobian matrix, the proposed indices TMI and CCI have the following merits:

TMI and CCI are dimensionless and frame-independent, so that the biased measure for the same PM caused by the selection of different reference coordinate frames can be avoided.

TMI and CCI range from 0 to 1, which results in intuitive measurement and comparison without interference from other factors of the PM (i.e., different rod lengths).

The proposed index CCI evaluates the quality of constraint force of lower-mobility PMs. In most cases, researchers only consider the mobility

property of the lower-mobility PM. That is to say, as long as the movement in the direction of non-mobility is constrained, the quality of the constraint is often ignored. The proposed CCI could evaluate the consistency of constraint force to resist deformation, achieving a more comprehensive evaluation of lower-mobility PMs.

## 5 CONCLUSIONS

Two new indices, TMI and CCI, are proposed to evaluate the manipulability to transmit force and the consistency to resist deformations, with the corresponding formulas being derived respectively under the conditions that the transmission matrix and constraint matrix are composed of linear force vectors, force couples, or both. These two indices stand out with the merits of unit homogeneity, frame independence and measurement facility without interference. Then, TMI and CCI are applied to 4-URU PM with mixed-motion PM, 2-UPR+SPR PM with parasitic motion and pure translational 3-CRU PM. The manipulability of transmission force and the consistency of constraint force of these PMs are evaluated. Moreover, the structural configuration of the 3-CRU PM whose TMI and CCI remain maximal is constructed for the first time, which means that the TWS and CWS exerted on the moving platform both have no distortion and achieve best manipulability and consistency in the whole workspace.

## 6 ACKNOWLEDGEMENTS

This work was supported by Science and Technology Planning Project of Guangdong Province, China (Grant No. 2019B040402006); Science and Technology Major Project of Zhongshan city, China (Grant No. 2018A10018).

## 7 REFERENCES

- [1] Merlet, J. (2006). *Parallel robots (Solid Mechanics and Its Applications, Vol. 2)*. Springer-Verlag, Dordrecht.
- [2] Mei, J., Zang, J., Ding, Y., Xie, S., Zhang, X. (2017). Rapid and automatic zero-offset calibration of a 2-DOF parallel robot based on a new measuring mechanism. *Strojniški vestnik - Journal of Mechanical Engineering*, vol. 63, no. 12, p. 715-724, DOI:10.5545/sv-jme.2017.4529.
- [3] Cheng, G., Gu, W., Yu, J., Tang, P. (2011). Overall structure calibration of 3-UCR parallel manipulator based on quaternion method. *Strojniški vestnik - Journal of Mechanical Engineering*, vol. 57, no. 10, p. 719-729, DOI:10.5545/sv-jme.2010.167.
- [4] Cheng, G., Xu, P., Yang, D., Li, H., Liu, H. (2013). Analyzing kinematics of a novel 3CPS parallel manipulator based on Rodrigues parameters. *Strojniški vestnik - Journal of Mechanical Engineering*, vol. 59, no. 5, p. 291-300, DOI:10.5545/sv-jme.2012.727.
- [5] Denavit, J., Hartenberg, R., Razi, R., Uicker, J. (1965). Velocity, acceleration, and static-force analyses of spatial linkages. *Journal of Applied Mechanics-Transactions of the ASME*, vol. 32, no. 4, p. 903-910, DOI:10.1115/1.3627334.
- [6] Yoshikawa, T. (1985). Manipulability of robotic mechanisms. *The International Journal of Robotics Research*, vol. 4, no. 2, p. 3-9, DOI:10.1177/027836498500400201.
- [7] Gosselin, C., Angeles, J. (1991). A global performance index for the kinematic optimization of robotic manipulators. *Journal of Mechanical Design*, vol. 113, no. 3, p. 220-226, DOI:10.1115/1.2912772.
- [8] Merlet, J. (2006). Jacobian, manipulability, condition number and accuracy of parallel robots. *Journal of Mechanical Design*, vol. 128, no. 1, p. 199-206, DOI:10.1115/1.2121740.
- [9] Wang, J., Liu, X., Wu, C. (2009). Optimal design of a new spatial 3-DOF parallel robot with respect to a frame-free index. *Science in China Series E Technological Sciences*, vol. 52, p. 986-999, DOI:10.1007/s11431-008-0305-4.
- [10] Alt, H. (1932). Der übertragungswinkel und seine bedeutung für das konstruieren periodischer getriebe. *Werkstattstechnik*, vol. 26, p. 61-64.
- [11] Sutherland, G., Roth, B. (1973). A transmission index for spatial mechanisms. *Journal of engineering for industry-Transactions of the ASME*, vol. 95, no. 2, p. 589-597, DOI:10.1115/1.3438195.
- [12] Tsai, M., Lee, H. (1994). Generalized evaluation for the transmission performance of mechanisms. *Mechanism and Machine Theory*, vol. 29, no. 4, p. 607-618, DOI:10.1016/0094-114X(94)90098-1.
- [13] Wang, J., Wu, C., Liu, X. (2010). Performance evaluation of parallel manipulators: motion/force transmissibility and its index. *Mechanism and Machine Theory*, vol. 45, no. 10, p. 1462-1476, DOI:10.1016/j.mechmachtheory.2010.05.001.
- [14] Liu, H., Huang, T., Kecskeméthy A, Chetwynd, D., Li, Q. (2017). Force/Motion transmissibility analyses of redundantly actuated and overconstrained parallel manipulators. *Mechanism and Machine Theory*, vol. 109, p. 126-138, DOI:10.1016/j.mechmachtheory.2016.11.011.
- [15] Meng, Q., Xie, F., Liu, X., Takeda, Y. (2020). Screw theory-based motion/force transmissibility analysis of high-speed parallel robots with articulated platforms. *Journal of Mechanisms and Robotics-Transactions of the ASME*, vol. 12, no. 4, p. 041011, DOI:10.1115/1.4046031.
- [16] Brinker, J., Corves, B., Takeda, Y. (2018). On the motion/force transmissibility and constrainability of Delta parallel robots. *Computational Kinematics. Mechanisms and Machine Science*, p. 340-348, DOI:10.1007/978-3-319-60867-9\_39.
- [17] Wang, C., Zhao, T., Li, E., Zhao, Y., Bian, H. Zhu, B. (2021). A novel index to evaluate the mapping of parallel mechanisms from internal to external wrenches. *Mechanism and Machine Theory*, vol. 155, art. ID 104058, DOI:10.1016/j.mechmachtheory.2020.104058.
- [18] Wang, X., Guo, W., Han, Y. (2020). A new index of static actuation force sensitivity of mechanisms based on unified forward Jacobian matrix. *Journal of Mechanisms and*

- Robotics-Transactions of the ASME*, vol. 12, no. 6, p. 1-30, DOI:10.1115/1.4046976.
- [19] Utenov, M., Sobh, T., Baigunchekov, Z., Zhilkibayeva, S., Patel, S. (2018). Analytical method for determination of internal forces of mechanisms and manipulators. *Robotics*, vol. 7, no. 3, art. ID 53, DOI:10.3390/robotics7030053.
- [20] Liang, X., Takeda, Y. (2019). Transmission index of a class of parallel manipulators with 3-RS(SR) primary structures based on pressure angle and equivalent mechanism with 2-SS chains replacing RS chain. *Mechanism and Machine Theory*, vol. 139, p. 359-378, DOI:10.1016/j.mechmachtheory.2019.04.018.
- [21] Angeles, J. (2006). *Fundamentals of Robotic Mechanical Systems: Theory, Methods, and Algorithms*. Springer Verlag, Berlin.
- [22] Angeles, J., López-Cajún, C.S. (1992). Kinematic isotropy and the conditioning index of serial robotic manipulators. *International Journal of Robotics Research*, vol. 11, no. 6, p. 560-571, DOI:10.1177/027836499201100605.
- [23] Chablat, D., Angeles, J. (2007). On the kinetostatic optimization of revolute-coupled planar manipulators. *Mechanism and Machine Theory*, vol. 37, no. 4, p. 351-374, DOI:10.1016/S0094-114X(01)00081-7.
- [24] Liu, Y., Xu, Y., Lyu, Y., Song, W. (2019). Kinematic performance analysis and scale optimization of a fully symmetric 4-URU parallel mechanism. *Journal of Mechanical Transmission*, vol. 29, no. 4, p. 35-40.
- [25] Huang, Z., Zhao, Y., Zhao, T. (2014). *Advanced Spatial Mechanism* (2nd ed). High Education Press, Beijing. (in Chinese)
- [26] Neumann, K. (2008). Adaptive in-jig high load Exechon machining & assembly technology. *Aerospace Manufacturing and Automated Fastening Conference & Exhibition*, p.08AMT-0044.
- [27] Tang, T., Zhao, Y., Zhang, J., Jin, Yan. (2015). Conceptual design and workspace analysis of an Exechon-inspired parallel kinematic machine. Ding, X., Kong, X., Dai, J. (eds.), *Advances in Reconfigurable Mechanisms and Robots II*. Springer, Berlin, p. 445-453, DOI:10.1007/978-3-319-23327-7\_39.
- [28] Zhao, Y., Cao, Y., Kong, X., Zhao, T. (2018). Type synthesis of parallel mechanisms with a constant Jacobian matrix. *Journal of Mechanisms and Robotics-Transactions of the ASME*, vol. 12, no. 6, art. ID 061011, DOI:10.1115/1.4040962.

# Optimization of Friction Stir Welding Operation Using Optimal Taguchi-based ANFIS and Genetic Algorithm

An-Le Van<sup>1</sup> – Trung-Thanh Nguyen<sup>2,\*</sup>

<sup>1</sup>Nguyen Tat Thanh University, Faculty of Engineering and Technology, Vietnam

<sup>2</sup>Le Quy Don Technical University, Faculty of Mechanical Engineering, Vietnam

The friction stir welding (FSW) process is an effective approach to producing joints of superior quality. Unfortunately, most published investigations primarily addressed optimizing process parameters to boost product quality. In the current work, the FSW operation of an aluminium alloy has been considered and optimized to decrease the specific welding energy (SWE) and enhance the jointing efficiency (JE) as well as micro-hardness at the welded zone (MH). The parameter inputs are the rotational speed ( $S$ ), welding speed ( $f$ ), depth of penetration ( $D$ ), and tool title angle ( $T$ ). The optimal adaptive neuro-based-fuzzy inference system (ANFIS) models were utilized to propose the welding responses in terms of the FSW parameters, while the Taguchi method was applied to optimize the ANFIS operating parameters. The neighbourhood cultivation genetic algorithm (NCGA) was employed to determine the best solution. The obtained results indicated that the optimal values of the  $S$ ,  $f$ ,  $D$ , and  $T$  are 560 rpm, 90 mm/min, 0.9 mm, and 2 deg, respectively. The SWE is decreased by 17 %, while the JE and MH are improved by 2.3 % and 6.4 %, respectively, at the optimal solution. The optimal ANFIS models for the welding responses were adequate and reliably employed to forecast the response values. The proposed optimization approach comprising the orthogonal array-based ANFIS, Taguchi, and NCGA could be effectively and efficiently utilized to save experimental costs as well as human efforts, produce optimal predictive models, and select optimum outcomes. The observed findings contributed significant data to determine optimal FSW parameters and enhance welding responses.

**Keywords:** friction stir welding; energy efficiency; jointing efficiency; micro-hardness; NCGA

## Highlights

- FSW operating parameters, including the rotational speed, welding speed, depth of penetration, and tool title angle were considered.
- The specific welding energy was minimized, while the jointing efficiency and micro-hardness at the welded zone were maximized.
- Optimal orthogonal array-based ANFIS models for welding performances were developed.
- An efficient optimization approach comprising the ANFIS, Taguchi, and NCGA was proposed.

## 0 INTRODUCTION

The friction stir welding (FSW) operation is an effective and efficient solid-state joining process in which the tool plastically deforms the material and mixes it to produce strong welds. The FSW process is widely employed to avoid the porosity, hot crack, and large deformation due to non-material melting, as compared to the other fusion welding processes. Moreover, this technology does not require material, such as shielding gas, electrodes, and filling materials, for generating welded joints. Consequently, the FSW operation could be efficiently and effectively applied to produce high quality joints for different materials with similar and/or dissimilar thicknesses.

Many attempts have been executed to improve the mechanical properties of the joints for different FSW operations, in which the conventional welding responses are the ultimate tensile strength ( $TS$ ), yield strength ( $YS$ ), elongation ( $EL$ ), welding force ( $WF$ ), welding temperature ( $WT$ ), micro-hardness at the welded zone ( $MH$ ), and grain size ( $GS$ ). The ratio

between shoulder and pin diameters ( $R$ ) of 4, the rotational speed ( $S$ ) of 100 rpm, the welding speed ( $f$ ) of 100 mm/min were utilized to improve the  $TS$  and  $EL$  of the AA6082-AA5754 joint [1]. The pin square, the  $S$  of 1400 rpm, the  $f$  of 1.75 mm/s, and the axial force ( $AF$ ) of 7.5 KN were applied to enhance the  $TS$ ,  $MH$ , and  $YS$  of the AA7075 weld [2]. The optimal data of the  $f$ ,  $S$ , and  $T$  were 25 mm/min, 1250 rpm, and 1 deg, respectively, which could be used to obtain the  $TS$  of 6.06 MPa for the composite joint [3]. Shojaeefard et al. stated that the optimal values of the  $S$  and  $f$  for the FSW operation of AA5083 were 1345 rpm and 60.0 mm/min, respectively [4]. For the welded magnesium alloy, the  $S$  was found to be the most effective contribution, followed by the  $f$  and the  $AF$  [5]. The  $S$  of 1550 rpm, the  $T$  of 4 deg, and octagonal pin were applied to boost the  $TS$  and  $EL$  of the aluminium alloy weld [6]. Gou et al. emphasized that the maximum  $TS$  and  $MH$  for the AA6061-T6 could be obtained at the  $D$  of 0.45 mm [7]. Saju and Narayanan revealed that the highest mechanical properties of the AA5052-AA6061 weld were achieved with the  $D$  of 0.6 mm [8]. The  $TS$  of 2.6 KN and the  $MH$  of 70.45 HV

for the dissimilar AA5083-C10100 weld were obtained at the  $S$  of 1250 rpm, depth of penetration ( $D$ ) of 1.9 mm, and dwell time ( $DT$ ) of 12.5 s, respectively [9]. Elyasi et al. emphasized that the  $T$  of 2 deg could be applied to improve the  $TS$  and  $MH$  of the AA1100 weld [10]. Farzadi et al. indicated that the  $S$  of 513 rpm, the  $f$  of 95 mm/min, the shoulder diameter ( $SD$ ) of 16.1 mm and the  $D$  of 5 mm could be applied to maximize the  $TS$  of the AA7075 weld [11]. The  $S$  of 900 rpm,  $f$  of 60 mm/min,  $SD$  of 18 mm, and  $D$  of 5 mm were employed to enhance the  $TS$ ,  $MH$ , and  $GS$  for the AA5083-AA6063 weld [12].

Palanivel et al. indicated that the  $S$  of 1000 rpm, the  $f$  of 60 mm/min, and the partial impeller pin were applied to improve the  $TS$  of AA6351-AA5083 joint [13]. The vertical force model of the FSW operation of AZ31 magnesium alloy was developed with the aid of an artificial neural network (ANN) [14]. Rajendran et al. revealed that the defect-free welds were obtained using the  $T$  of 1 deg to 3 deg [15]. The  $S$  of 1005 rpm,  $f$  of 20 mm/min, and  $T$  of 3 deg were utilized to increase the  $TS$  of the AA2219 joint [16]. The  $TS$  of 167 MPa, the  $YS$  of 145 MPa, and the  $EL$  of 8.3 % for the 6063-T6 joint were achieved using optimum outcomes [17]. The maximum  $TS$  (135.83 MPa) and  $EL$  (4.35 %) of the AA6061-A5083 joint were produced at the  $T$  of 1.11 deg, the  $S$  of 1568 rpm, and the  $f$  of 39.53 mm/min, respectively [18]. Boukraa et al. indicated that the  $WT$  and dissolution time were enhanced by 13.44 % and 46.5 %, respectively, at the optimal solution for the AA2195-T8 joint [19]. Sathesh et al. revealed that the taper cylindrical pin geometry, the  $S$  of 1045 rpm, the  $f$  of 1.5 mm/s, and the  $AF$  of 4.87 kN were applied to improve the  $TS$ ,  $YS$ , and  $EL$  for the AZ91C Mg alloy joint [20]. The distribution of the  $WT$  on the AZ80A Mg Alloy joint was analysed by Sevel et al., in which the authors stated that the  $S$  was named as the best contribution, followed by the  $f$  and  $AF$ , respectively [21]. The empirical models of the  $TS$ ,  $EL$ , and percentage reduction in area were developed in terms of the  $S$ ,  $f$ , and  $SD$  for the carbon steel weld [22]. A simulation model was developed to investigate the impacts of the  $S$  and pin geometry on the  $WT$  for the AZ80A Mg alloy weld, in which the authors stated that the maximum  $WT$  was obtained by means of distinctive geometries [23].

As a result, different FSW processes with various materials have been considered and optimized to enhance welding performances. However, the shortcomings of published works can be listed as follows.

Quality indicators are primary considerations of the aforementioned works. The impacts of FSW

factors on energy consumption have not been analysed.

The energy consumption model regarding the FSW parameters has not been developed.

The selection of optimal FSW parameters for decreasing energy consumed and improving the welding quality (e.g., ultimate tensile strength and elongation) has not been addressed.

To overcome these challenges, the FSW operation of the AA6061 has been considered and optimized to decrease the specific welding energy ( $SWE$ ) and enhance the jointing efficiency ( $JE$ ) as well as micro-hardness at the welded zone ( $MH$ ). The optimal Taguchi-based ANFIS models were utilized to propose FSW performances regarding the  $S$ ,  $f$ ,  $D$ , and  $T$ . The optimal outcomes are selected with the aid of the NCGA.

The scientific contributions of the current study can be expressed as follows.

The developed optimizing method comprising the Taguchi method, ANFIS, and NCGA can be considered an effective and efficient approach to solving complicated optimization issues and selecting optimal outcomes. The developed approach possesses various advantages, including low experimental costs, decreased human efforts, and easy implementation. The developed technique could be effectively and efficiently employed to optimize not only welding operations but also other machining processes.

The impacts of the FSW parameters on the FSW responses have been thoroughly analysed. The obtained knowledge can help machine operators comprehend the physical insights in the FSW operation of the AA6061.

The analysed outcomes of the current study can be effectively and efficiently utilized as significant references for future investigations and developing expert systems regarding FSW processes.

## 1 OPTIMIZING FRAMEWORK

Traditionally, the primary aim of the FSW process is to produce the welds with superior quality, as seen in factors such as ultimate tensile strength, elongation, micro-hardness at the weld nugget zone, yield strength, and grain size. Unfortunately, the rise of energy cost and environmental legislation requires manufacturers to decrease energy consumed, welding noise/fumes, and wastage. In this investigation, three technological responses, including the  $SWE$ ,  $JE$ , and  $MH$ , are listed as important indicators.

The profile of the power consumed for the FSW process is shown in Fig. 1, in which three operating

phases, including the plunge, dwell, and welding states are depicted. For the plunge phase, the workpieces are tightly clamped on the fixture, while the rotating tool is inserted into the joint line of plates. For the dwell phase, the rotational motion of the welding tool is kept in its position to plasticize the material around the pin. For the welding phase, the linear motion of the tool is performed to produce the weld in the solid state.

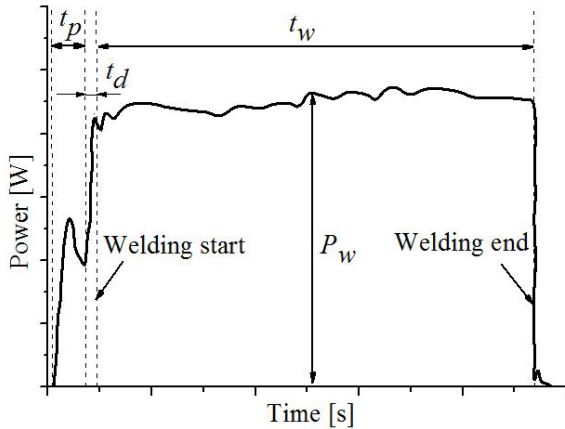


Fig. 1. The profile of the power consumption

The *SWE* value is calculated as:

$$SWE = \frac{P_w}{f}, \quad (1)$$

where  $P_w$  and  $f$  are the power consumed in the welding time and welding speed, respectively.

The *JE* value is computed as:

$$JF = \frac{UTS_w}{UTS_b}, \quad (2)$$

where  $UTS_w$  and  $UTS_b$  denote the ultimate tensile strength of the weld and base material, respectively.

The *MH* value is computed as:

$$MH = \frac{\sum_{i=1}^n MH_i}{n}, \quad (3)$$

where  $MH_i$  and  $n$  denotes the micro-hardness at the  $i^{th}$  position and the number of measuring points, respectively.

The schematic of the FSW operation with the four process parameters is shown in Fig. 2. The welding tool and materials used are considered fixed conditions. Four key process parameters, including the  $S$ ,  $f$ ,  $D$ , and  $T$  are listed as optimizing inputs (Table 1). The ranges of the  $S$  and  $f$  are primarily selected based on the specifications of the machine tool and recommendations of the manufacturer of the welding

tool. The levels of the  $D$  and  $T$  are determined using the configuration of the machine tool and the knowledge of the previous publications. The highest and lowest values of process parameters were tested by means of experimental trials to ensure machinability. These values are confirmed by company experts and welding handbooks.

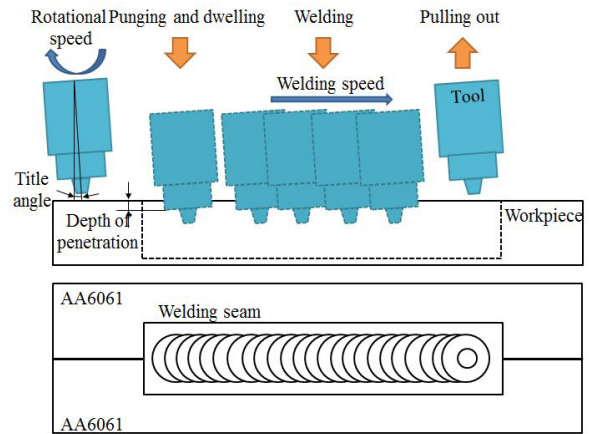


Fig. 2. The schematic illustration of the FSW operation

Consequently, the optimizing issue is expressed as follows:

$$\text{Finding } X = [S, f, D, \text{ and } T].$$

Maximizing *JE* and *MH*; Minimizing *SWE*.

$$\text{Constraints: } 480 \leq S \leq 1600 \text{ rpm; } 48 \leq f \leq 112 \text{ mm/min; } 0.6 \leq D \leq 1.2 \text{ mm; } 0 \leq T \leq 4 \text{ deg}$$

The systematic approach for generating optimal FSW parameters is shown in Fig. 3.

Step 1: The physical experiments of the FSW operation are then conducted using the orthogonal array  $L_{32}$ .

Step 2: The ANFIS models of the *SWE*, *JE*, and *MH* are developed in terms of the FSW parameters. In this investigation, the ANFIS with five layers are developed to model welding performances [24].

Layer I: This layer is employed to convert the inputs set to fuzzy set with the aid of the assigned membership function. The outputs of three welding responses are expressed:

$$L1, x = \mu Ax(E), \quad (4)$$

$$L1, y = \mu By(T), \quad (5)$$

$$L1, z = \mu Cz(L), \quad (6)$$

where  $E$ ,  $T$ , and  $L$  are the input variable nodes, while  $x$ ,

$y, z, A, B,$  and  $C$  are connected labels having  $\mu(E), \mu(S,$  and  $\mu(P)$  as memberships.

Layer II: This layer is employed to generate the fixed function of the input. The node function  $\Pi$  is expressed as:

$$L2, x = \mu Ax(E) \times \mu By(T) \times \mu Cz(L). \quad (7)$$

Layer III: This layer contains the fixed node labelled N. The output namely the normalized firing strength is represented as:

$$L3x = \bar{\omega}_i = \frac{\omega_i}{\sum_{i=1}^n \omega_i}. \quad (8)$$

Layer IV: This layer contains an adaptive node. The current layer is applied to assign the consequent parameters of the rules. The output of this layer is expressed as:

$$L4x = \bar{\omega}_i(a_i x + b_i x + c_i), \quad (9)$$

where  $a_i, b_i,$  and  $c_i$  are the consequent parameters, respectively.

Layer V: This layer comprises only one fixed node. The fifth layer is used to calculate the overall output of all incoming signals. The output of this layer is expressed as:

$$L5x = \sum_i \bar{\omega}_i f_i. \quad (10)$$

Step 3: The optimal parameters of the ANFIS models are selected using the Taguchi method.

It is necessary to select the proper operating factors of each ANFIS model to minimize the predictive errors. The aforementioned publications randomly determine the operating parameters, including the number of inputs, types of input, optimal method, and types of output. Practically, a variety of each ANFIS parameter changes the mean square error (MSE), which is expressed as:

$$MSE = \frac{1}{n} \sum_{i=1}^n (y_m - y_p)^2, \quad (11)$$

where  $y_m$  and  $y_p$  are the measured and predicted values, respectively.

Step 4: The optimal outcomes of the FSW process factors and technical responses are selected with the aid of the NCGA.

The NCGA is an effective solution to solve the trade-off analysis between the conflicting responses. This algorithm possesses various advantages, including easy computational skills, a large number of feasible solutions, and producing global optimization results. The NCGA provides

better results than conventional approaches, such as multi-objective genetic algorithm (MOGA) and non-dominated sorting genetic algorithm II (NSGA-II) when responses have a multiple peak landscape and a higher number of design variables. However, the NCGA requires higher computational time to conduct the algorithm. The working principle of the NCGA is summarized, as follows (Fig. 4):

- Assigning initial population ( $P_0$ ) and computing fitness of the initial individual.
- Generating and sorting a new generation ( $P_t$ ) based on the objective purpose.
- Performing crossover and mutation operations for generating new child individuals.
- Assembling produced individuals and generating a new population.

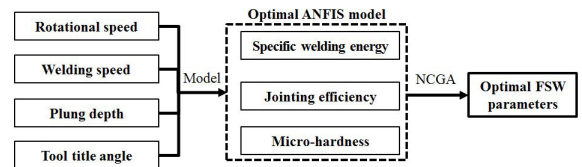


Fig. 3. The flow chart of optimization approach

Table 1. FSW parameters for the experimental work

No.	Symbol	Parameters	Values		
1	$S$	Rotational speed [rpm]	480	1120	1600
2	$f$	Welding speed [mm/min]	48	77	112
3	$D$	Depth of penetration [mm]	0.60	0.90	1.20
4	$T$	Tool title angle [deg]	0	2	4

## 2 EXPERIMENTS AND MEASUREMENTS

The welding specimens with a length of 160 mm, a width of 100 mm, and a thickness of 6 mm are prepared with the aid of milling process. The joints between the AA6061 plates are widely utilized in the marine industry to resist the corrosion of seawater. The chemical compositions and mechanical properties of the AA6061 with the aid of the axial tension test are presented in Table 2.

The welding experiments are done with the aid of a vertical milling machine and a fabricated fixture (Fig. 5). The welding tool with a cylindrical tapered pin is applied to perform trials. The hot die steel entitled H13 is used as the tool material due to its high strength, wear resistance, and stability at higher temperatures. The flat bars are employed to clamp the workpiece tightly using the bolts.

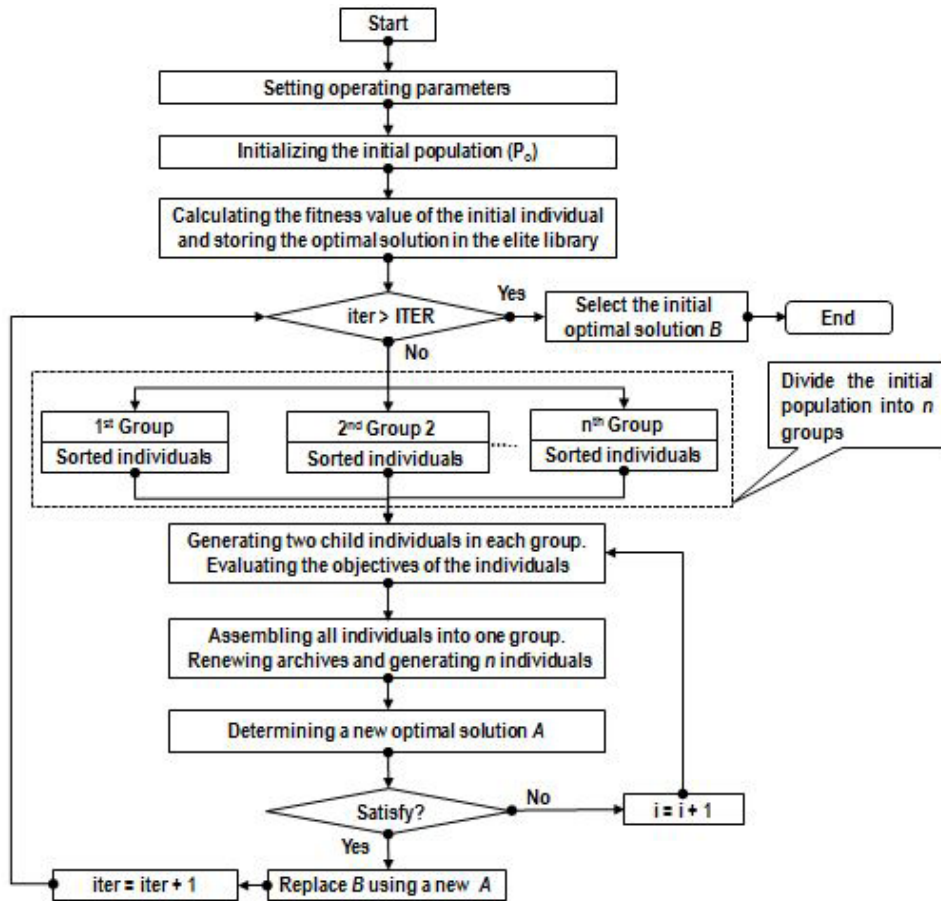


Fig. 4. The operating principle of the NCGA

Table 2. Chemical compositions and mechanical properties of the AA6061

Element	Mn	Fe	Mg	Si	Cu	Zn	Ti	Cr	Others	Al
[%]	0.12	0.55	0.10	0.60	0.30	0.20	0.10	0.30	0.10	Balance
Mechanical properties										
Ultimate tensile strength [MPa]	Yield stress [MPa]	Elongation [%]	Vickers Hardness [HV]	Poisson's ratio	Modulus of elasticity [GPa]					
241	214	15.2	104	0.33	68.9					

A power sensor (Kyoritsu 6305) is used to record the variety of power components during the welding time. The obtained data is stored in the flashcard and visualized with the aid of the KEW6305 software. The reading and scaling errors are  $\pm 0.3\%$  and  $\pm 0.2\%$ , respectively, to improve the measuring precision, while the up-dating time of 1 second is utilized to visualize the capture data.

The ultimate tensile strength and elongation are obtained with the aid of the Exceed E45 machine based on the American Society for Testing of Materials (ASTM E8) guidelines. The resolution of 0.1 MPa is employed to improve the accuracy of

the measuring tensile strength. The Vickers Wolpert Wilson machine is used to measure the micro-hardness with the force of 500d at the dwell time of 20 seconds. The resolution of 0.1 HV is applied to capture the experimental data.

### 3 RESULTS AND DISCUSSION

#### 3.1 Development of the Optimal ANFIS Models

The experimental outcomes of the FSW operation are shown in Table 3.

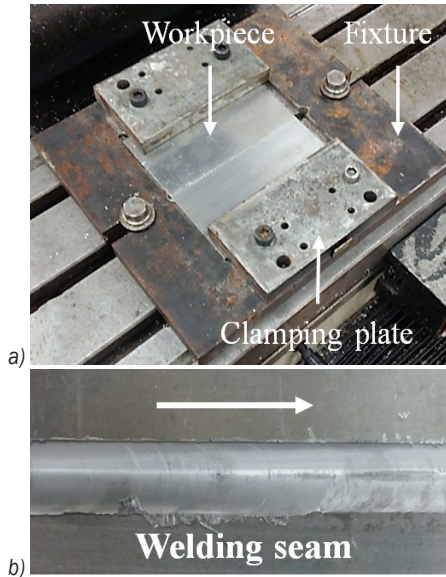


Fig. 5. FSW Experiment; a) experimental setting, b) representative specimen

Practically, the optimal architecture of the ANFIS model is randomly determined using the decisive maker, which decreases the predicting precision. In this study, optimal Taguchi-based ANFIS models are proposed to render the relations between process parameters and FSW performances. Four ANFIS operating parameters are the number of input MFs ( $N$ ), types of input MFs ( $TI$ ), optimal method ( $O$ ), and types of output MFs ( $TO$ ). The parameter combinations of the ANFIS model are produced with the support of the Taguchi experimental matrix  $L_{16}$ . The numerical experiments of ANFIS models are executed to calculate the MSE values for three welding responses. As shown in Fig. 6a, the optimal outcomes of the  $N$ ,  $TI$ ,  $O$ , and  $TO$  for the  $SWE$  model are 2, *gaussmf*, *hybrid*, and *linear*, respectively. As shown in Figs. 6b and c, the optimal outcomes of the  $N$ ,  $TI$ ,  $O$ , and  $TO$  for the  $JE$  and  $MH$  models are 2, *gaussmf*, *hybrid*, and *constant*, respectively. The 2-2-2-2-2 ANFIS architecture can be used to render the relations between welding parameters and the responses (Fig. 7). The schematic rules for ANFIS models of the  $SWE$ ,  $JE$ , and  $MH$  are shown in Figs. 8 a, b, and c, respectively.

The Gaussian membership function is expressed as:

$$\mu_{A_i}(x) = \exp \left[ -\frac{1}{2} \left( \frac{x - c_i}{a_i} \right)^2 \right], \quad (12)$$

where  $a_i$  and  $c_i$  are the definite centre and its width of the membership function, respectively.

To investigate the accuracy of developed ANFIS models, a set of experiments is performed at random points. The comparisons between the obtained and ANFIS results are presented in Table 4. The errors of the  $SWE$ ,  $JE$ , and  $MH$  lie within the range of -1.48 % to 0.53 %, -0.86 % to 0.59 %, and -0.11 % to 1.20 %, respectively. The accepted deviations indicate that the developed models performed well in predicting welding responses.

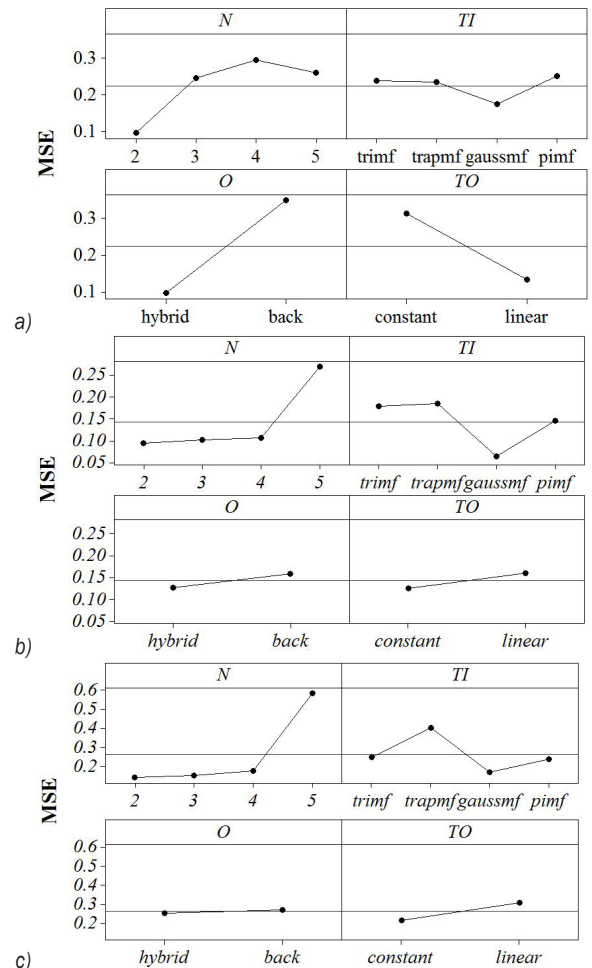


Fig. 6. MSE values for FSW responses; a) for  $SWE$  model, b) for  $JE$  model, c) for  $MH$  model

### 3.2 ANOVA Results for Welding Performances

The ANOVA results of the  $SWE$ ,  $JE$ , and  $MH$  models are presented in Tables 5 to 7, respectively. The  $R^2$ , adjusted  $R^2$ , and predicted  $R^2$  values indicate that the developed models are adequate.

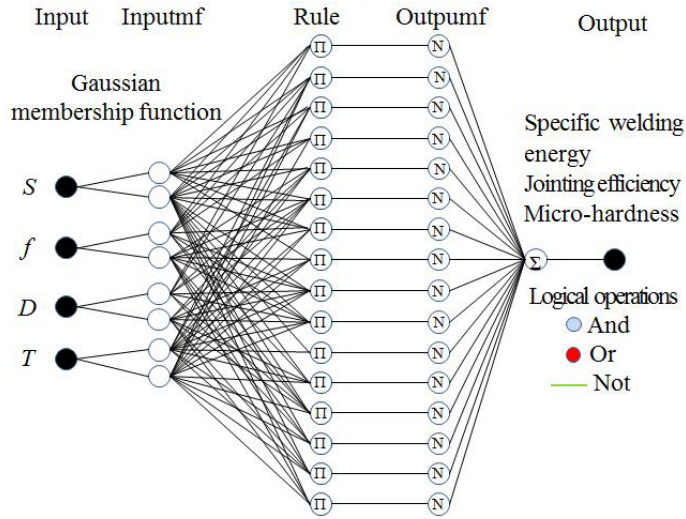


Fig. 7. The ANFIS structures for welding performances

Table 3. Experimental data for the FSW operation

No.	$S$ [rpm]	$f$ [mm/min]	$D$ [mm]	$T$ [deg]	$SWE$ [J/mm]	$UTS_w$ [MPa]	$JE$ [%]	$MH$ [HV]
1	480	48	0.6	0	1693.64	133.1	55.24	74.2
2	1120	77	0.6	2	1211.24	158.9	65.95	62.8
3	1600	112	0.6	4	960.73	131.2	54.45	60.3
4	480	48	0.6	0	1693.64	133.2	55.28	74.2
5	480	48	0.6	2	1741.24	152.7	63.36	71.4
6	1120	77	0.6	0	1175.54	139.5	57.89	66.2
7	1600	112	0.6	0	909.19	113.8	47.22	69.3
8	480	48	0.6	4	1801.61	151.1	62.68	66.7
9	480	77	0.9	4	1255.48	151.3	62.78	62.8
10	1120	48	0.9	0	1903.33	165.0	68.45	55.3
11	1600	48	0.9	0	2013.54	164.3	68.17	51.1
12	480	112	0.9	2	889.28	139.2	57.78	72.4
13	480	77	0.9	0	1183.62	142.1	58.98	68.3
14	1120	48	0.9	4	2016.12	174.1	72.22	47.5
15	1600	48	0.9	2	2066.76	179.5	74.48	47.5
16	480	112	0.9	0	879.27	124.2	51.53	73.8
17	480	48	1.2	0	1854.52	160.3	66.53	61.2
18	1120	112	1.2	2	934.86	161.1	66.83	60.4
19	1600	77	1.2	4	1461.78	170.3	70.67	43.9
20	480	48	1.2	0	1854.52	160.5	66.58	61.2
21	480	48	1.2	2	1898.37	171.3	71.08	59.9
22	1120	112	1.2	0	922.43	150.3	62.36	62.2
23	1600	77	1.2	0	1378.67	169.9	70.49	51.1
24	480	48	1.2	4	1954.99	161.1	66.86	56.5
25	480	112	0.6	4	860.74	126.4	52.45	74.4
26	1120	48	0.6	0	1800.72	147.8	61.31	63.5
27	1600	48	0.6	0	1910.77	145.7	60.44	59.2
28	480	77	0.6	2	1134.09	146.3	60.71	73.5
29	480	112	0.6	0	824.22	108.9	45.17	80.7
30	1120	48	0.6	4	1917.26	165.6	68.73	54.2
31	1600	48	0.6	2	1965.87	165.2	68.54	54.9
32	480	77	0.6	0	1102.67	126.8	52.63	75.9
33	560	66	0.8	2	1397.78	160.3	66.52	65.7
34	800	90	1.0	0	1052.33	150.1	62.28	63.1
35	1250	112	1.2	4	973.83	151.1	62.68	55.3
36	1600	66	0.9	0	1557.83	159.2	66.05	53.4
37	1250	90	1.1	4	1178.58	164.2	68.15	50.2
38	1120	90	1.0	4	1151.58	162.1	67.27	52.6

**Table 4.** Comparative errors for the welding responses

No.	SWE [J/mm]			JE [%]			MH [HV]		
	Exp.	ANFIS	Err. [%]	Exp.	ANFIS	Err. [%]	Exp.	ANFIS	Err. [%]
33	1397.78	1390.42	0.53	66.52	66.14	0.57	65.7	65.2	0.76
34	1052.33	1067.89	-1.48	62.28	62.77	-0.79	63.1	63.8	-1.11
35	973.83	970.12	0.38	62.65	62.28	0.59	55.3	55.7	-0.72
36	1557.83	1552.94	0.31	66.05	66.62	-0.86	53.4	53.8	-0.75
37	1178.58	1172.93	0.48	68.15	68.73	-0.85	50.2	49.6	1.20
38	1151.58	1159.46	-0.68	67.27	67.59	-0.48	52.6	52.1	0.95

Exp.: Experimental value; Err.: Error

For the SWE model, single terms (*S*, *f*, *D*, and *T*), interactive terms (*Sf*, *fD*, and *fT*), and quadratic terms (*S*<sup>2</sup>, *f*<sup>2</sup>, and *D*<sup>2</sup>) are significant factors. The contributions of the *S*, *f*, *D*, and *T* are 7.89 %, 50.59 %, 5.47 %, and 3.77 %, respectively. The contributions of the *Sf*, *fD*, and *fT* are 3.28 %, 2.35 %, and 1.77 %, respectively. The contributions of the *S*<sup>2</sup>, *f*<sup>2</sup>, and *D*<sup>2</sup> are 1.73 %, 19.74 %, and 2.18 %, respectively.

For the *JE* model, single terms (*S*, *f*, *D*, and *T*), interactive term (*Sf*, *SD*, and *DT*), and quadratic terms (*S*<sup>2</sup>, *f*<sup>2</sup>, *D*<sup>2</sup>, and *T*<sup>2</sup>) are significant factors. The contributions of the *S*, *f*, *D*, and *T* are 8.81 %, 20.64 %, 16.09 %, and 6.64 %, respectively. The contributions of the *Sf*, *SD*, and *DT* are 2.78 %, 2.46 %, and 6.29 %, respectively. The contributions of the *S*<sup>2</sup>, *f*<sup>2</sup>, *D*<sup>2</sup>, and *T*<sup>2</sup> are 11.16 %, 6.93 %, 2.45 %, and 15.52 %, respectively.

For the *MH* model, single terms (*S*, *f*, *D*, and *T*), interactive term (*Sf*, *ST*, *fD*, and *DT*), and quadratic terms (*S*<sup>2</sup>, *f*<sup>2</sup>, *D*<sup>2</sup>, and *T*<sup>2</sup>) are significant factors. The contributions of the *S*, *f*, *D*, and *T* are 23.89 %, 16.87 %, 16.49 %, and 11.49 %, respectively. The contributions of the *Sf*, *ST*, *fD*, and *DT* are 2.94 %, 2.53 %, 2.29 %, and 2.29 %, respectively. The contributions of the *S*<sup>2</sup>, *f*<sup>2</sup>, *D*<sup>2</sup> and, *T*<sup>2</sup> are 7.18 %, 3.86 %, 5.66 %, and 3.37 %, respectively.

### 3.3 The Impacts of FSW Parameters

The influences of FSW parameters on the specific welding energy are shown in Fig. 9.

Fig. 9a indicates that a higher *S* increases the *SWE*, while an increased *f* causes a reduction in the *SWE*. When the *S* relatively rises from 480 rpm to 1600 rpm, the *SWE* is relatively increased by 13.6 %. At a higher *S*, the momentum of the main spindle increases and the spindle system consumes more power consumed to satisfy the desired value. The total power consumed of the machine tool increases; hence, the *SWE* increases according to Eq. (1). An increased *S* causes higher welding engagement between the tool and

**Table 5.** ANOVA results for the SWE model

So	SS	MS	F Value	p-value
Mo	343725.7	343725.7	35.3	0.0001
S	598793.7	598793.7	859.8	0.0001
f	383216.9	383216.9	5512.8	0.0001
D	415233.3	415233.3	596.1	0.0001
T	286087.7	286087.7	410.8	0.0001
Sf	248222.2	248222.2	357.4	0.0033
fD	178436.6	178436.6	256.1	0.0046
fT	134269.3	134269.3	192.9	0.0058
S2	131912.9	131912.9	188.5	0.0062
f2	149067.7	149067.7	2151.1	0.0001
D2	164422.1	164422.1	237.5	0.0048
Res	76608.1	6964.4		
Cor	351433.8			

*R*<sup>2</sup> = 0.9782; Adjusted *R*<sup>2</sup> = 0.9734; Predicted *R*<sup>2</sup> = 0.9622

**Table 6.** ANOVA results for JE model

So	SS	MS	F Value	p-value
Mo	892.76	63.769	41.008	< 0.0001
S	26533.5	26533.5	17063.37	< 0.0001
f	62162.5	62162.5	39975.93	< 0.0001
D	48459.1	48459.1	31163.41	< 0.0001
T	199981	199981	12860.47	< 0.0001
Sf	8372.6	8372.6	5384.35	0.0045
SD	7408.9	7408.9	4764.57	0.0048
DT	18943.9	18943.9	12182.58	0.0003
S2	33611.1	33611.1	21614.89	< 0.0001
f2	20871.4	20871.4	13422.15	0.0001
D2	7378.7	7378.7	4745.205	0.0048
T2	46742.4	46742.4	30059.42	< 0.0001
Res	17.105	1.555		
Cor	909.865			

*R*<sup>2</sup> = 0.9812; Adjusted *R*<sup>2</sup> = 0.9746; Predicted *R*<sup>2</sup> = 0.9622

workpiece to be machined, leading to higher friction at the interfaces. Greater resistance is produced, which requires more power used to overcome the friction of the joining materials; hence, the *SWE* logically increases. There are similar impacts of the spindle

**Table 7.** ANOVA results for *MH* model

	So	SS	MS	F Value	p-value
Mo		1446.74	103.34	33.081	< 0.0001
S		1639.87	1639.87	524.963	< 0.0001
f		1158.00	1158.00	370.705	< 0.0001
D		113.91	113.91	362.354	< 0.0001
T		788.70	788.70	252.483	< 0.0001
Sf		201.81	201.81	64.604	0.0056
ST		173.66	173.66	55.595	0.0058
fD		157.19	157.19	50.321	0.0061
DT		157.19	157.19	50.321	0.0061
S2		492.85	492.85	157.775	0.0002
f2		264.96	264.96	84.820	0.0043
D2		388.51	388.51	124.374	0.0003
T2		231.32	231.32	74.053	0.0044
Res		34.36	3.12		
Cor		1481.10			
$R^2 = 0.9768$ ; Adjusted $R^2 = 0.9691$ ; Predicted $R^2 = 0.9638$					

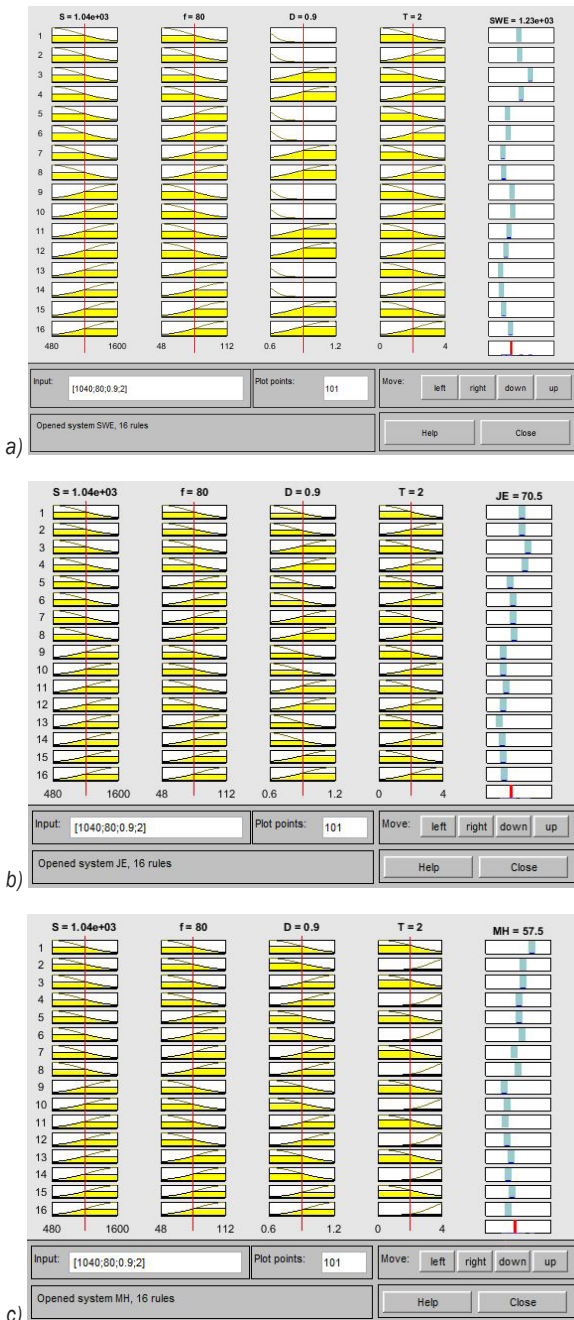


**Fig. 8.** The schematic rules for;

a) *SWE* model, b) *IF* model, and c) *MH* model

speed on the energy consumption for the turning [25], milling [26], and burnishing [27] processes.

As shown in Fig. 9a, when the  $f$  relatively changes from 47 mm/min to 112 mm/min, the *SWE* is relatively decreased by 52.6 %. An increased  $f$  causes higher power consumption in the feed driving system; hence, the total power used in the machine tool increases.

Fortunately, the *SWE* is inversely proportional to  $f$  according to Eq.1; therefore, higher  $f$  decreases the *SWE* value. An increment in the  $f$  causes a reduction in the welding time, which decreases the machining engagement between the tool and workpiece; hence, a decreased friction at the interfaces is obtained. Low power consumption is required due to low resistance; hence, the *SWE* decreases. Similar impacts of the transverse speed on the energy consumption can be found in the turning [25], milling [26], and burnishing [27] operations.

As shown in Fig. 9b, an increased  $D$  causes a higher *SWE*. When the  $D$  relatively changes from 0.6 mm to 1.2 mm, the *SWE* is relatively increased by 9.6 %. An increase in the  $D$  causes a higher depth of shoulder inside the workpiece. This creates hindrances for tool movement, leading to higher friction at the interfaces between the tool and workpiece. Higher power consumed is required to overcome greater resistance; hence, the *SWE* increases. An increased energy consumption with a higher depth of penetration can be found for the turning [25], milling [26], and burnishing [27] processes.

As shown in Fig. 9b, an increased  $T$  causes a higher *SWE*. When the  $T$  relatively rises from 0 deg mm to 4 deg, the *SWE* is relatively increased by 6.3 %. At a higher  $T$ , the depth of the shoulder inside the specimen increases; which leads to higher friction between the tool and workpiece. Greater resistance for tool movement is obtained, which requires more power consumption; hence, a higher *SWE* is required. Higher energy consumption with an increased  $T$  was presented in the work of [10].

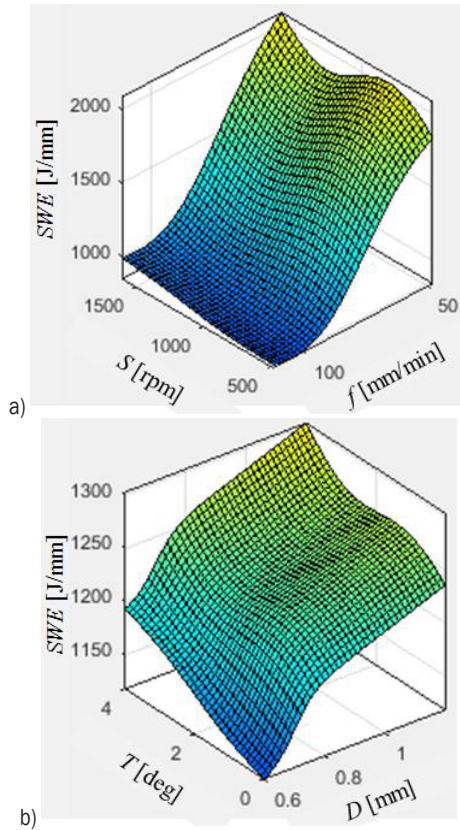


**Fig. 9.** The interactive influences; a)  $SWE$  versus  $S$  and  $f$ ; and b)  $SWE$  versus  $T$  and  $D$

The influences of FSW parameters on the jointing efficiency are shown in Fig. 10. As shown in Fig. 10a, the  $JE$  increases as the  $S$  increases to the middle value and decreases thereon. When the  $S$  rises from 480 rpm to 1120 rpm, the  $JE$  is relatively increased by 8.4 %. The  $JE$  is relatively decreased by 0.6 % as the  $S$  changes from 1120 rpm to 1600 rpm. A higher  $S$  increases the welding engagement, leading to higher heat generation at the interfaces. The hardness and strength of the two materials decrease, which increases the degree of the mixture; hence, the stir zone size and the bonded area enhances. Consequently, the tensile strength improves, leading to higher jointing efficiency. In contrast, a further  $S$  causes excessive heat input, which results in grain growth in the welded region. The tensile strength of the weld decreases, leading to a reduction in the  $JE$ . The similar influences of the  $S$  on the tensile strength can be found in the works of [1], [2], [4] and [6].

As shown in Fig. 10a, a higher  $f$  decreases the  $JE$ . When the  $f$  rises from 47 mm/min to 112 mm/min, the  $JE$  is relatively reduced by 15.73 %. A higher  $f$  increases the velocity of the welding tool and decreases the processing time. The heat generation at

the interfaces decreases, resulting in the lack of proper diffusion between the two plates. In other words, the degree of the mixture decreases, leading to higher grain size in the welded region. The tensile strength of the weld decreases, leading to a decreased  $JE$ . A reduction in the tensile strength with higher welding speed can be found in the works of [1], [2], [4], and [11].

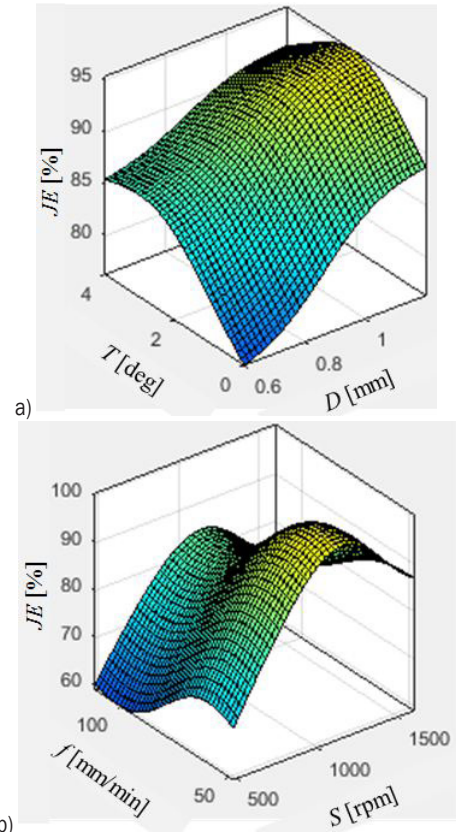


**Fig. 10.** The interactive influences; a)  $JE$  versus  $S$  and  $f$ ; and b)  $JE$  versus  $T$  and  $D$

Fig. 10b indicates that an increase in the  $D$  increases the  $JE$ . When the  $D$  relatively rises from 0.6 mm to 1.2 mm, the  $JE$  is relatively increased by 13.9 %. A higher depth of shoulder inside the workpiece is obtained with an increased  $D$ . An increase in the heat generation is obtained due to higher friction at the interfaces between the tool and workpiece increases. The consolidation of the weld by effective diffusion of atoms between the two plates is enhanced. A better mixture between two materials is achieved, leading to higher tensile strength; hence, the  $JE$  increases. Higher tensile strength with an increase in the depth of penetration can be found in the publications [8], [9], and [11].

As shown in Fig. 10b, the  $JE$  increases as the  $T$  increases to the middle value and decreases thereon. When the  $T$  rises from 0 deg to 2 deg, the  $JE$  is relatively increased by 10.1 %. The  $JE$  is relatively decreased by 3.9 % as the tool tile angle changes from 2 deg to 4 deg. A higher  $T$  causes an increased depth of shoulder inside the specimen; which leads to higher friction between the tool and workpiece. The heat generation increases at the interfaces, leading to a better mixture between two materials due to the enlargement in the welded zone. Therefore, the tensile strength of the joint increases, resulting in a higher  $JE$ . Further  $T$  causes excessive heat generation, leading to a coarse grain; hence, the  $JE$  decreases. The similar impacts of the tool title angle on the tensile strength are presented in the works of [3], [6], [16], and [18].

The influences of FSW parameters on the micro-hardness at the welded zone are shown in Fig. 11. As shown in Fig. 11a, a higher  $S$  decreases the  $MH$ . When the  $S$  relatively rises from 480 rpm to 1600 rpm, the  $MH$  is relatively reduced by 21.8 %. An increased  $S$  causes higher welding engagement at the interfaces between the tool and specimen. A higher degree of friction increases, leading to an increased heat generation in the welding region. The hardness and strength of the welded specimen decrease, resulting in soft and flexible structures; hence, the  $MH$  decreases. A decreased micro-hardness with higher welding speed can be found in the works of [2], [9], [12], and [15].

As shown in Fig. 11a, a higher  $f$  increases the  $MH$ . When the  $f$  relatively rises from 47 mm/min to 112 mm/min, the  $MH$  is relatively enhanced by 19.3 %. Higher  $f$  causes an increased velocity of the tool and a reduction in the welding time. The welding engagement decreases, leading to a reduction in the friction at the interfaces. The heat generation decreases, resulting in higher strength and hardness of the welded specimen. Therefore, an increased  $MH$  is obtained. Similar impacts of the welding speed on the micro-hardness are presented in the works of [2] and [12].

As shown in Fig. 11b, the  $MH$  decreases with an increased  $D$ . When the  $D$  relatively rises from 0.6 mm to 1.2 mm, the  $MH$  is relatively decreased by 15.9 %. A higher  $D$  increases the depth of the shoulder inside the workpiece. The friction at the interfaces between the tool and workpiece to be machined increases. Excessive heat generation is obtained, which causes the coarse-graining in welding metal and dissolves of sediments in aluminium alloys. Consequently, the  $MH$  decreases. Low micro-hardness with higher depth of penetration can be found in the works of [7] and [8].

As shown in Fig. 11b, the  $MH$  decreases with an increased  $T$ . When the  $T$  relatively rises from 0 deg to 4 deg, the  $MH$  is relatively decreased by 11.7 %. At a higher  $T$ , the depth of shoulder inside the specimen increases; which leads to higher friction between the tool and workpiece. The heat generation increases at the interfaces, leading to a higher grain size at the welded region. Consequently, low  $MH$  is observed with an increased  $T$ . The similar impacts of the tool title angle on the micro-hardness are presented in the works of [10] and [15].

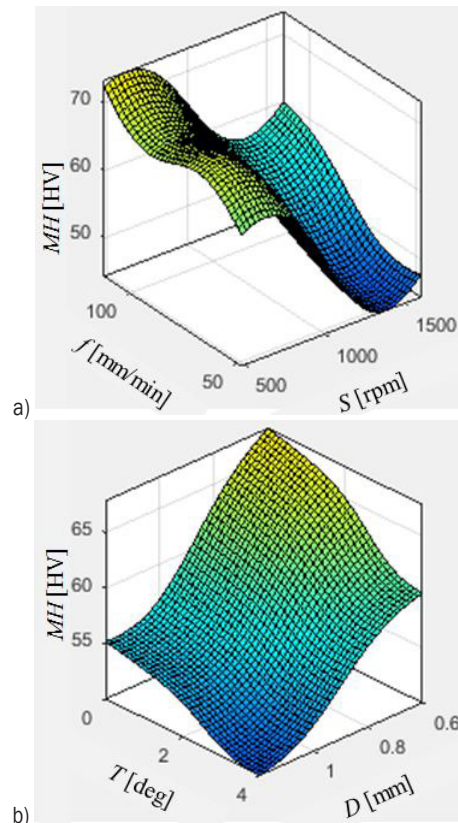


Fig. 11. The interactive influences, a) EL versus  $S$  and  $f$ , and b) EL versus  $T$  and  $D$

### 3.4 Optimization Results

The developed ANFIS models are applied to select the optimal outcomes with the aid of the NCGA. The operating parameters of the NCGA are shown in Table 8. In this study, we select the collapse of the population ( $\alpha$ ) as the convergence parameter, which can be expressed as:

$$\alpha = \left( \frac{y_{\max} - y_{\min}}{y_{\max}} \right) \times 100, \quad (13)$$

where  $y_{max}$  and  $y_{min}$  are the maximum and minimum responses.

**Table 8.** Operating parameters of the NCGA

No.	Symbol	Parameters	Values		
1	PO	Population size	20	40	60
2	NG	Number of generations	20	40	60
3	MR	Mutation rate	0.01	0.03	0.05
4	GS	Gene size	40	60	80

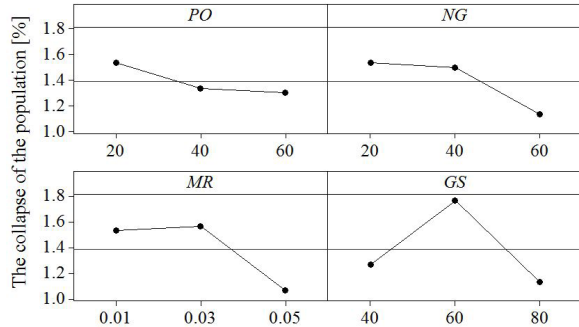


**Fig. 12.** Selection of optimal NCGA parameters

The minimum value of the  $\alpha$  is utilized to select the convergence, while the  $SWE$  is considered as the objective function. The computation trials are conducted by means of the Taguchi experimental matrix  $L_9$ . As shown in Fig. 12, the optimal data of the  $PO$ ,  $NG$ ,  $MR$ , and  $GS$  are 60, 60, 0.05, and 80, respectively.

We have simultaneously performed the PSO to solve the optimization issue. The Pareto graphs produced by the NCGA and PSO are presented in Figs. 13a and b, respectively. As a result, the number of feasible designs of the NCGA and PSO are 560 and 301, respectively. Moreover, the NCGA provides better results, as compared to the PSO ones (Table 9).

An experimental confirmation is conducted at the optimal point to check the reliability of the obtained results. The small deviation indicates that the proposed approach comprising the ANFIS, Taguchi method, and NCGA is feasible and reliable (Table 10).

The microstructure in the nugget zone is shown in Fig. 14, in which the grains are entirely transformed into fine-sized structure with even distribution and equal space. The welding defects, such as porosity, voids, flash, and cracks, have not been found in the welded zones. It can be stated that the fine grains using the recrystallization have been produced with the aid of optimal FSW parameters. In other words, the joints of AA6061 plates have been successfully implemented, leading to high-quality joint.

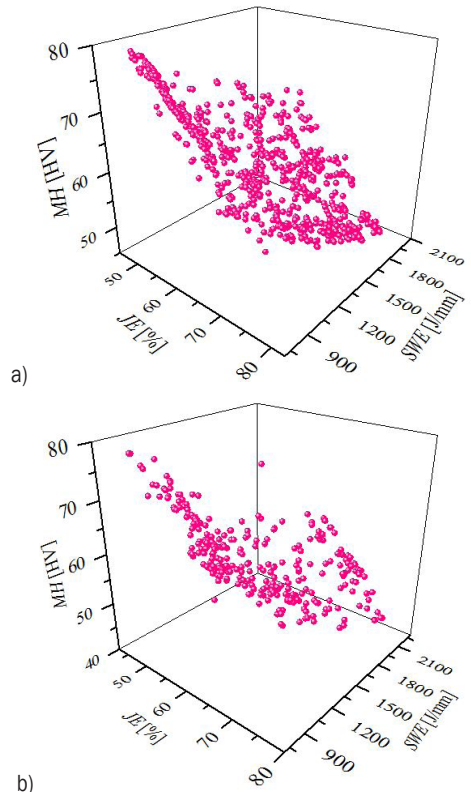


**Fig. 13.** Pareto fronts; a) produced by the NCGA, b) produced by the PSO

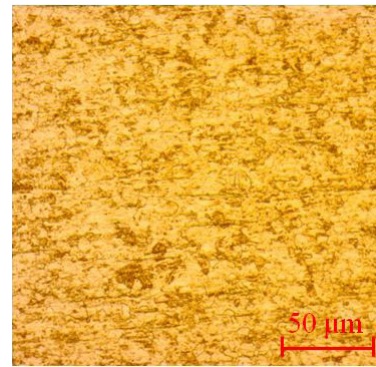


**Fig. 14.** The microstructure in the nugget zone

The industrial values can be listed as follows.

The obtained results are effectively applied to improve performance measures of the FSW process of the aluminium alloy.

The 2-2-2-2-2 ANFIS architectures could be used to render the relations between FSW parameters and the welding performances. The welding models proposed by the ANFIS approach are significant and adequate, which are capable of generating accurate predictions for the response values of the FSW operation of the aluminium alloy.

**Table 9.** Optimization results generated by the NCGA and PSO

Method	Optimization parameters				Responses		
	$S$ [rpm]	$f$ [mm/min]	$D$ [mm]	$T$ [deg]	$EW$ [kJ]	$JE$ [%]	$MH$ [HV]
Initial values	480	77	0.9	4	1255.47	62.78	62.8
Optimal results-PSO	1040	85	0.8	3	1090.21	61.73	63.8
Optimal results-NCGA	560	90	0.9	2	1042.63	64.21	66.8
Improvement [%]					-17.0	2.3	6.4

**Table 10.** Confirmatory results

Method	Optimization parameters				Responses		
	$S$ [rpm]	$f$ [mm/min]	$D$ [mm]	$T$ [deg]	$EW$ [kJ]	$JE$ [%]	$MH$ [HV]
Optimal results	560	90	0.9	2	1042.63	64.21	66.8
Experiment	560	90	0.9	2	1048.38	64.96	68.2
Error [%]					-0.6	-1.2	-2.1

#### 4 CONCLUSIONS

In the current investigation, the friction stir welding (FSW) operation of the AA6061 has been addressed and optimized to decrease the specific welding energy ( $SWE$ ) and enhance the jointing efficiency ( $JE$ ) as well as the micro-hardness ( $MH$ ). The optimizing FSW parameters are the rotational speed ( $S$ ), welding speed ( $f$ ), depth of penetration ( $D$ ), and tool title angle ( $T$ ). The ANFIS models of the welding responses were proposed in terms of the optimizing inputs, in which optimal operating parameters were optimized using the Taguchi method. The NCGA was applied to determine optimal values of welding parameters and objectives. The finding can be listed as follows.

1. The lowest levels of the  $S$ ,  $D$ , and  $T$  could be utilized to reduce the  $SWE$ , while the highest  $f$  was recommended. To enhance the  $JE$ , higher values of the  $S$ ,  $D$ , and  $T$  could be utilized, while lower  $f$  could be applied. Similarly, an increased  $MH$  could be obtained with higher values of the  $S$ ,  $D$ , and  $T$ , while a lower  $f$  is encouraged.
2. All machining factors have significant contributions to the ANFIS models. For the  $SWE$  model, the  $f$  was named as the most effective factor, followed by the  $S$ ,  $D$ , and  $T$ , respectively. For the  $JE$  model, the welding speed was the most effective factor, followed by the  $D$ ,  $S$ , and  $T$ , respectively. For the  $MH$  model, the  $S$  had the highest contribution, followed by the  $f$ ,  $D$ , and  $T$ , respectively.
3. The optimal parameters proposed by orthogonal array-based ANFIS-Taguchi method-NCGA of the  $S$ ,  $f$ ,  $D$ , and  $T$  were 560 rpm, 90 mm/min, 0.9 mm, and 2 deg, respectively. The  $SWE$  was

decreased by 17 %, while the  $JE$  and  $MH$  were enhanced by 2.3 % and 6.4 %, respectively.

4. This investigation addressed the specific welding energy, jointing efficiency, and micro-hardness at the welded zone under the variation of FSW parameters. The impacts of welding conditions on the costs and grain size will be explored in future works.
5. Practically, the weights reflect the importance of each response in relation to other performances. Therefore, the weight should be objectively determined based on experimental data, instead subjective chosen of the decisive maker to generate reliable optimal outcomes.

#### 5 ACKNOWLEDGEMENTS

This research is funded by Vietnam National Foundation for Science and Technology Development (NAFOSTED) under grant number 107.04-2020.02.

#### 6 REFERENCES

- [1] Kasman, Ş. (2013). Multi-response optimization using the Taguchi-based grey relational analysis: a case study for dissimilar friction stir butt welding of AA6082-T6/AA5754-H111. The International Journal of Advanced Manufacturing Technology, vol. 68, p. 795-804, DOI:10.1007/s00170-012-4720-0.
- [2] Babajanzade Roshan, S., Behboodi Jooibari, M., Teimouri, R., Asgharzadeh-Ahmadi, G., Falahati-Naghbi, M., Sohrabpoor, H., (2013). Optimization of friction stir welding process of AA7075 aluminum alloy to achieve desirable mechanical properties using ANFIS models and simulated annealing algorithm. The International Journal of Advanced Manufacturing Technology, vol. 69, p. 1803-1818, DOI:10.1007/s00170-013-5131-6.

- [3] Ahmadi, H., Mostafa Arab, N.B., Ghasemi, F.A. (2014). Optimization of process parameters for friction stir lap welding of carbon fibre reinforced thermoplastic composites by Taguchi method. *Journal of Mechanical Science and Technology*, vol. 28, p. 279-284, DOI:10.1007/s12206-013-0966-1.
- [4] Shojaeefard, M.H., Akbari, M., Asadi, P. (2014). Multi objective optimization of friction stir welding parameters using FEM and neural network. *International Journal of Precision Engineering and Manufacturing*, vol. 15, p. 2351-2356, DOI:10.1007/s12541-014-0600-x.
- [5] Senthilraja, R., Sait, A.N. (2015). Optimization of the parameters of friction stir welding for AZ91D magnesium alloy using the Taguchi Design. *Materials Science*, vol. 51, p. 180-187, DOI:10.1007/s11003-015-9826-8.
- [6] Kumar, S., Kumar, S. (2015) Multi-response optimization of process parameters for friction stir welding of joining dissimilar Al alloys by gray relation analysis and Taguchi method. *Journal of the Brazilian Society of Mechanical Sciences and Engineering*, vol. 37, p. 665-674, DOI:10.1007/s40430-014-0195-2.
- [7] Guo, C., Shen, Y., Hou, W., Yan, Y., Huang, G., Liu, W. (2018). Effect of groove depth and plunge depth on microstructure and mechanical properties of friction stir butt welded AA6061-T6. *Journal of Adhesion Science and Technology*, vol. 32, p. 2709-2726, DOI:10.1080/01694243.2018.1505347.
- [8] Saju, T.P., Narayanan, G.R. (2018). Effect of tool plunge depth on joint formation and mechanical performance of friction stir forming joints made between AA 5052-H32 and AA 6061-T6 sheet metals. *Transactions of Nonferrous Metals Society of China*, vol. 28, no. 4, p. 613-628, DOI:10.1016/S1003-6326(18)64694-1.
- [9] Siddharth, S., Senthilkumar, T. (2016). Optimization of friction stir spot welding process parameters of dissimilar Al 5083 and C 10100 joints using response surface methodology. *Russian Journal of Non-Ferrous Metals*, vol. 57, p. 456-466, DOI:10.3103/S1067821216050151.
- [10] Elyasi, M., Aghajani Derazkola, H., Hosseinzadeh, M. (2016). Investigations of tool tilt angle on properties friction stir welding of A441 AISI to AA1100 aluminium. *Proceedings of the Institution of Mechanical Engineers, Part B: Journal of Engineering Manufacture*, vol. 230, no. 7, p. 1234-1241, DOI:10.1177/0954405416645986.
- [11] Farzadi, A., Bahmani, M., Haghshenas, D.F. (2017). Optimization of operational parameters in friction stir welding of AA7075-T6 aluminum alloy using response surface method. *Arabian Journal for Science and Engineering*, vol. 42, p. 4905-4916, DOI:10.1007/s13369-017-2741-6.
- [12] Gupta, S.K., Pandey, K.N., Kumar, R. (2018). Multi-objective optimization of friction stir welding process parameters for joining of dissimilar AA5083/AA6063 aluminum alloys using hybrid approach. *Proceedings of the Institution of Mechanical Engineers, Part L: Journal of Materials: Design and Applications*, vol. 232, no. 4, p. 343-353, DOI:10.1177/1464420715627294.
- [13] Palanivel, R., Laubscher, R., Vigneshwaran, S., Dinaharan, I. (2018). Prediction and optimization of the mechanical properties of dissimilar friction stir welding of aluminum alloys using design of experiments. *Proceedings of the Institution of Mechanical Engineers, Part B: Journal of Engineering Manufacture*, vol. 232, no. 8, p. 1384-1394, DOI:10.1177/0954405416667404.
- [14] D'Orazio, A., Forcellese, A., Simoncini, M. (2019). Prediction of the vertical force during FSW of AZ31 magnesium alloy sheets using an artificial neural network-based model. *Neural Computing & Applications*, vol. 31, p. 7211-7226, DOI:10.1007/s00521-018-3562-6.
- [15] Rajendran, C., Srinivasan, K., Balasubramanian, V., Balaji, H., Selvaraj, P. (2019). Effect of tool tilt angle on strength and microstructural characteristics of friction stir welded lap joints of AA2014-T6 aluminum alloy. *Transactions of Nonferrous Metals Society of China*, vol. 29, no. 9, p. 1824-1835, DOI:10.1016/S1003-6326(19)65090-9.
- [16] Kamal Babu, K., Panneerselvam, K., Sathiya, P., Noorul Haq, A., Sundarajan, S., Mastanaiah, P., Srinivasa Murthy, C.V. (2018). Parameter optimization of friction stir welding of cryorolled AA2219 alloy using artificial neural network modeling with genetic algorithm. *The International Journal of Advanced Manufacturing Technology*, vol. 94, p. 3117-3129, DOI: 10.1007/s00170-017-0897-6.
- [17] Senthil, S.M., Parameshwaran, R., Ragu Nathan, S., Bhuvanesh Kumar, M., Deepandurai, K. (2020). A multi-objective optimization of the friction stir welding process using RSM-based-desirability function approach for joining aluminum alloy 6063-T6 pipes. *Structural and Multidisciplinary Optimization*, vol. 62, p. 1117-1133, DOI:10.1007/s00158-020-02542-2.
- [18] Verma S, Kumar V. (2021). Optimization of friction stir welding parameters of dissimilar aluminium alloys 6061 and 5083 by using response surface methodology. *Proceedings of the Institution of Mechanical Engineers, Part C: Journal of Mechanical Engineering*, DOI:10.1177/09544062211005804.
- [19] Boukraa, M., Chekifi, T., Lebaal, N., Aissani, M. (2021). Robust optimization of both dissolution time and heat affected zone over the friction stir welding process using SQP technique. *Experimental Techniques*, DOI:10.1007/s40799-021-00515-8.
- [20] Satheesh, C., Sevel, P., Senthil Kumar, R. (2020). Experimental identification of optimized process parameters for FSW of AZ91C Mg alloy using quadratic regression models. *Strojniški vestnik - Journal of Mechanical Engineering*, vol. 66, no. 12, p. 736-751, DOI:10.5545/sv-jme.2020.6929.
- [21] Sevel, P., Dhanesh Babu, S.D., Senthil Kumar, R. (2020). Peak temperature correlation and temperature distribution during joining of AZ80A Mg alloy by FSW - a numerical and experimental investigation. *Strojniški vestnik - Journal of Mechanical Engineering*, vol. 66, no. 6, p. 395-407, DOI:10.5545/sv-jme.2020.6566.
- [22] Bhatia, A., Wattal, R. (2021). Process parameters optimization for maximizing tensile strength in friction stir-welded carbon steel. *Strojniški vestnik - Journal of Mechanical Engineering*, vol. 67, no. 6, p. 311-321, DOI:10.5545/sv-jme.2021.7203.
- [23] Dhanesh Babu, S.D., Sevel, P., Senthil Kumar, R. (2020). Simulation of heat transfer and analysis of impact of tool pin geometry and tool speed during friction stir welding of AZ80A Mg alloy plates. *Journal of Mechanical Science and Technology*, vol. 34, p. 4239-4250, DOI:10.1007/s12206-020-0916-7.

- [24] Ho, W.H., Tsai, J.T., Lin, B.T., Chou, J.H. (2009). Adaptive network-based fuzzy inference system for prediction of surface roughness in end milling process using hybrid Taguchi-genetic learning algorithm. *Expert Systems with Applications*, vol. 36, no. 2, p. 3216-3222, DOI:10.1016/j.eswa.2008.01.051.
- [25] Warsi, S.S., Agha, M.H., Ahmad, R., Jaffery, S.H.I., Khan, M. (2019). Sustainable turning using multi-objective optimization: a study of Al 6061 T6 at high cutting speeds. *The International Journal of Advanced Manufacturing Technology*, vol. 100, p. 843-855, DOI:10.1007/s00170-018-2759-2.
- [26] Jang, D.-Y., Jung, J., Seok, J. (2016). Modeling and parameter optimization for cutting energy reduction in MQL milling process. *International Journal of Precision Engineering and Manufacturing-Green Technology*, vol. 3, p. 5-12, DOI:10.1007/s40684-016-0001-y.
- [27] Teimouri, R. Amini, S. (2019). A comprehensive optimization of ultrasonic burnishing process regarding energy efficiency and workpiece quality. *Surface and Coatings Technology*, vol. 375, p. 229-242, DOI:10.1016/j.surfcoat.2019.07.03.

# Determination of Limiting Dome Height (LDH) Values for Inconel 718 Alloy Sheet Using FEA and a Hemispherical Punch Method

Kanmani Ganesan\* – Saravanan Sambasivam – Rajesh Ramadass  
PSG College of Technology, Department of Production Engineering, India

*In a uniaxial tensile test, the material properties of Inconel 718 alloy sheet, such as yield strength, ultimate tensile strength, percentage of elongation, normal anisotropy, planar anisotropy, strain hardening exponent and the strength coefficient were determined in the longitudinal, diagonal, and transverse rolling directions. The main aim of this research is focused on the determination of limiting dome height (LDH) values for Inconel 718 alloy sheet of 1 mm thickness through experiments and finite element analysis using a hemispherical punch method. A limit curve was established through experimentation, which ensures a safe working region for 1 mm thick Inconel 718 sheet at room temperature. Scanning electron microscope (SEM) analysis of 100 mm and 120 mm width specimens indicated smooth surfaces and ductile fractures. The examination of 140 mm and 160 mm width specimens showed rough surfaces and shear-ductile failures. In finite element analysis, Barlat-89 yield criterion was used to obtain the limiting dome height (LDH) values and strain distribution in the specimen using ABAQUS6.1. A close relationship with minor deviation was observed between the experimental LDH values and finite element analysis results. The chemical composition of the fractured sheet examined using energy dispersive spectrum (EDS) analysis was similar to the results observed with an X-ray fluorescence (XRF) technique conducted on the Inconel 718 alloy sheet before failure. The approach presented in this work can be applied to obtain the LDH values of researched material focused.*

**Keywords:** Inconel 718 alloy sheet, uniaxial tensile test, hemispherical punch method, LDH values, SEM, EDS

## Highlights

- The mechanical properties of Inconel 718 alloy sheet of 1mm thickness were obtained in different rolling directions.
- The percentage of elongation was high (47.6 %) in the rolling direction compared to other transverse directions.
- The strain hardening ( $n$ ) is found to be 0.34, which indicates good stretch ability and formability.
- The strain limit obtained is the safe region where the material is susceptible to plastic deformation without failure.
- The LDH values obtained from ABAQUS6.1 and experimental results were in good agreement. The error was found to be less than 5 %.

## 0 INTRODUCTION

The usage of superalloys is increasing in aerospace and defence applications. Inconel is a nickel-chromium alloy with exceptional corrosion and oxidation resistance that is used at extreme environments. The transformation of sheet metal into desired shapes without deformation is considered as the measure of formability of a material. The sheet metal formability is evaluated using different methods, such as the Keeler test, Hecker test, Markiniak test, Nakizima test, and Hasek test. Gupta and Kumar [1] applied a Hecker simplified technique for the formability of galvanized interstitial free sheets. The forming limit diagram (FLD) has been evaluated experimentally using a hemispherical punch method. Pérez Caro et al. [2] determined that among the various nickel-based superalloys, the properties of Inconel 718 alloys sheets have attracted the attention of researchers for manufacturing sheet metal components. Reed [3] and Anderson et al. [4] discussed sheet metal forming processes that are commonly used in industries and

compared them to other manufacturing process as the grain orientation remains unaffected after processing the material. The authors [4] also reported that Inconel 718 alloy sheet is one of the hardest alloys in nickel-chromium-iron-based superalloy family widely used in the form of sheet metal for fabricating fuel cells, outer casings, heat exchanger devices, fuel tanks, and various structures of space and aircraft vehicles. Sajun Prasad et al. [5] reported that the formability of the material in the sheet metal forming process is evaluated using FLD, and the trend line is obtained as a plot between circumferential and radial strain measurement. A rigid hemispherical punch and die set up was used to obtain the FLD. It indicated the maximum strain that the material can withstand before failure. Banabic al. [6] observed that the experimental determination of FLD is a time-consuming process, which has led to the development of numerical models and computational methods. Jayahari et al. [7] predicted the mechanical properties of Inconel 718 alloy sheet at sub-zero temperatures in different rolling directions using artificial neural networks

(ANN). Djavanroodi and Derogar [8] investigated the strain distribution in the forming of Ti6Al4 alloy and Al6061-T6 alloy sheets; the impact of factors on the FLD was also evaluated and simulated using ABAQUS. Narayanasamy and Narayanan [9] obtained the experimental FLD for interstitial free (IF) steel of different thicknesses by press forming. Also, the SEM analysis of fractured test specimens in a uniaxial test showed ductile fractures. Badr et al. [10] explored various yield criteria and hardening rules to convert the forming limit diagram to a forming limit stress diagram. It was found that the Barat-89 and Hosford-79 material models provided extremely high accuracy values against the experimental results obtained using the forming limit diagram. Toshniwal et al. [11] studied the mechanical properties of Ti-6Al-4V using tensile test and obtained the FLD of the material using a stretch forming test. Sudarsanetal. [12] determined the mechanical properties of SS304 in three different rolling directions and studied the influence of parameters on the limiting strain. Rahmaan et al. [13] examined the strain rate influence on flow stress and anisotropy for the sheet metal alloys DP600, TRIP780 and AA5182-O. These materials exhibit no significant dependence of anisotropy and strain rate in the tensile test. Li et al. [14] studied the strain rate influence on the mechanical properties, fracture mechanism of DP780 dual-phase steel was investigated; it was found that the micro-cracks and voids increased with increases in the strain rate. Mahalle et al. [15] found that the FLD for precipitate hardened Inconel 718 alloy at various temperatures from room temperature to 700° using Nakazima test. The author also emphasized that the theoretical models proposed for FLD prediction are the Swift model, Hill model, and M-K model. The application of these models for formability prediction is a time-consuming process. The finite element method for the prediction of LDH values is urgently needed in the sheet metal industry. Finite element analysis reduces the costs incurred by the trial-and-error method of sheet metal forming. Paul [16] declared that FLD is extremely sensitive on strain paths. The yield criterion selection had a significant impact on the results of a stress-based forming limit diagram. Paul [17] developed a model to predict the FLC of steel sheets from the simple tensile properties of the material. Paul [18] identified minor deviations of FLC using the International Organization for Standardisations (ISO), time dependant, slope, and flat valley methods. The detailed review of journal articles quoted in the above discussion [1] to [18] revealed that only very minimum work was done in

the topic of “LDH determination for Inconel 718 alloy sheet at room temperature”.

Therefore, the proposed work discusses the new findings related to the gap identified in the literature study. The chemical composition of Inconel 718 alloy sheet was found using XRF. The mechanical properties of the sheet were obtained in different rolling directions using a uniaxial tensile test. The LDH values of 1 mm thick Inconel 718 alloy sheet were determined by experimentation and finite element analysis using the hemispherical punch method. SEM and EDS analysis of the fracture specimen is also presented.

## 1 MATERIALS AND METHODS

The workflow process chart is indicated in Fig. 1. The Inconel 718 alloy sheet was tested for chemical composition using the XRF technique. The sheet was subjected to uniaxial tensile testing, and the mechanical properties were determined in different rolling directions. The specimens were prepared as per Hecker’s simplified technique; experimental LDH values and FLD for the Inconel 718 alloy sheet were obtained using the hemispherical punch method. The test results obtained from uniaxial tensile test were provided as input to ABAQUS 6.1. The strain distribution along with simulated LDH values was obtained. The LDH values obtained through experiment and Finite Element Analysis (FEA) simulation results were compared. If the results are not in agreement, the FEA-based simulation is repeated in ABAQUS 6.1. If the results are in close agreement, then the results of the work are summarized in the conclusion.

### 1.1 Chemical Composition and Microstructure

Inconel 718 alloy sheet (1 mm thickness) was subjected to chemical composition testing using an X-ray fluorescence (XRF) technique. The elements Cr, Mo, Fe, Al, and Ti are especially important for increasing solid solution strengthening and corrosion resistance; the count of niobium helps to increase the creep strength in the deep-drawing application. The chemical composition of Inconel 718 alloy sheet is shown in Table 1. The alloy specimens were prepared by electrically etching them. The polishing was performed using oxalic acid and water in a proportion of 1:10 for studying the microstructure with an optical microscope.

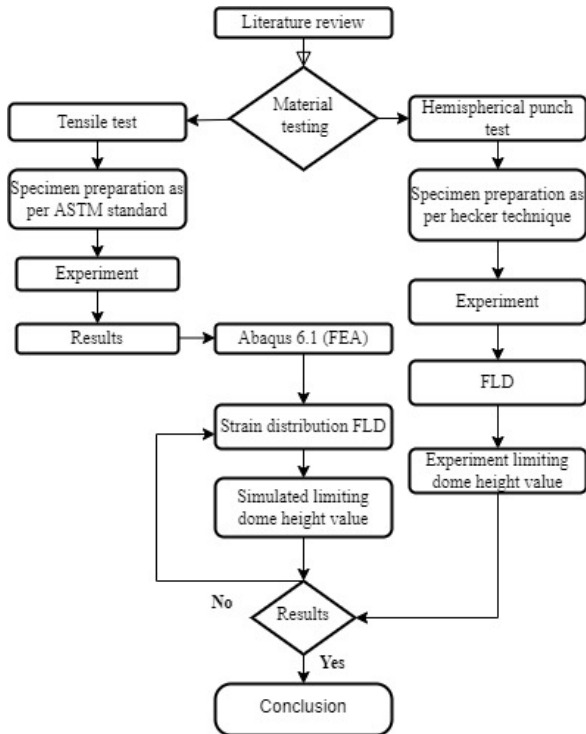


Fig. 1. Process flow chart

Table 1. Chemical composition of Inconel 718 alloy sheet

Element	Ni	Cr	Fe	Nb	Mo	Ti	Al
%	53.2	19.5	18.2	4.8	3.0	1.8	1.2

Microstructure obtained from optical microscope, shown in Fig. 2. indicates grain size of 7.5 μm with morphology variations in rolling direction, transverse and diagonal direction.

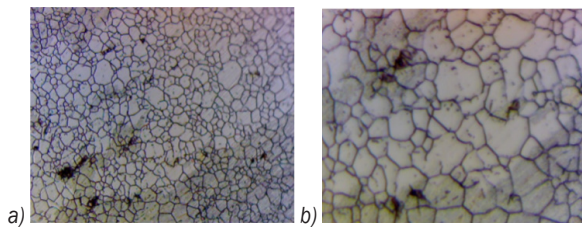


Fig. 2. Microstructure of Inconel 718 alloy sheet before deformation; a) mag:200x, and b) mag:500x

### 1.2 Tensile Test

The specimen the or uniaxial tensile test is prepared as per ASTM E8M standard [19] by wire-cut electrical discharge machining (WEDM) shown in Fig. 3.

The specimen was prepared using WEDM to obtain good surface finish and tight tolerance in Inconel 718 alloy sheets. The specimens were prepared

in three different directions: parallel (0 degree), diagonal (45 degree) and perpendicular (90 degree) rolling direction as indicated in Fig. 4. The uniaxial test was carried out at a constant crosshead speed of 2 mm/min. The tensile test was per formed in a Zwick/Roelltensile testing machine of 100 kN (UTM). The constants representing the material behaviour in a range of the plastic region is determined using the true stress-strain curves.

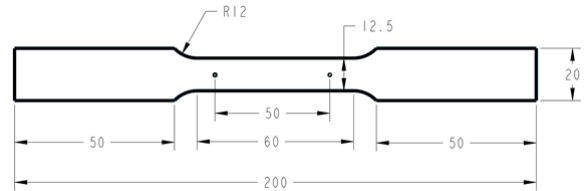


Fig. 3. Tensile specimen as per ASTM E8M

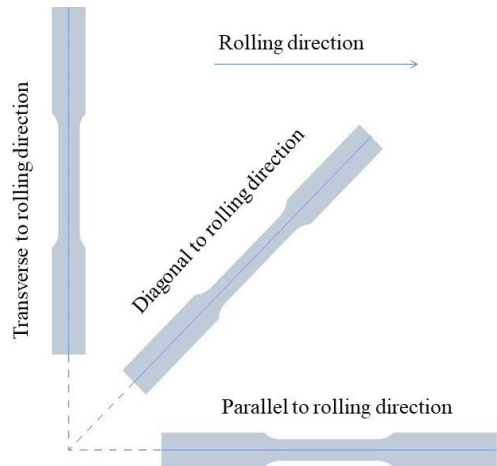


Fig. 4. Tensile samples in different rolling direction

The strain-hardening exponent ( $n$ ) of materials is characterized by Hollomon’s power law, and it plays an important role in formability, as shown in Eq. (1). The Lankford coefficient ( $r$ -value), normal ( $R$ ) and planar ( $\Delta R$ ) anisotropy of the sheet materials are calculated with Eqs. (2) to (4).

$$\sigma = K \epsilon^n, \tag{1}$$

$$r = \frac{\partial w}{\partial t} = \frac{\ln\left(\frac{w_f}{w_0}\right)}{\ln\left(\frac{l_0 w_0}{l_f w_f}\right)}, \tag{2}$$

$$R = \frac{r_0 + r_{45} + r_{90}}{4}, \tag{3}$$

$$\Delta R = \frac{r_0 - 2r_{45} + r_{90}}{2}, \tag{4}$$

where  $K$  is the strength coefficient,  $\epsilon$  true strain,  $w_f$  is final width,  $w_0$  initial width,  $l_f$  final length,  $l_0$  initial length of sheet.

### 1.3 Forming Limit Diagram (FLD)

FLD is an important parameter index that describes the maximum limit of principal strain that the material can withstand before failure. Limiting strains at necking and fracture are determined using forming limit diagram and fracture limit curve in sheet metal forming. Kotkunde et al. [20] prepared the specimens using Hecker's simplified technique for experimental determination of FLD in Ti-6Al-4V alloy. Thus, in this work, the specimens of the Inconel 718 alloy sheet for experimental FLD were also prepared with Hecker's simplified technique.

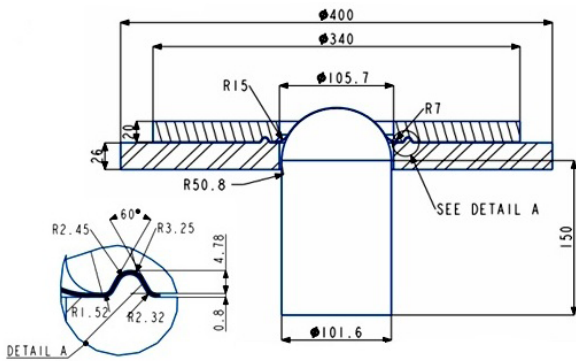


Fig. 5. Schematic model of hemispherical punch test

The FLD for Inconel 718 alloy sheet is obtained using a specifically designed and fabricated hemispherical punch, blank holder, and die. Fig. 5 shows a schematic drawing of the hemispherical punch die setup. Fig. 6 indicates the 3D model and the details of the individual parts. Three steps are followed during the experimental procedure: grid marking, punch-stretching of a grid marked sheet, and strain measurement of a deformed specimen.

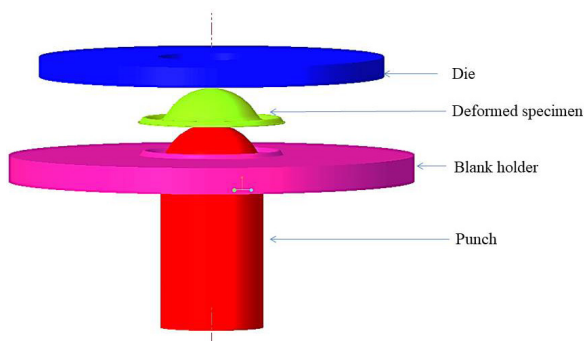


Fig. 6. 3D Model of forming die setup

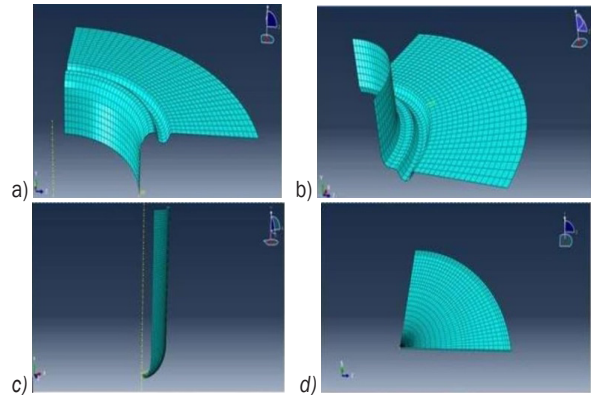


Fig. 7. Meshing of components in ABAQUS 6; a) die meshed eight node linear brick element, b) blank holder meshed four node linear tetrahedron element, c) punch meshed four node linear tetrahedron element, and d) sheet meshed eight node linear brick element

### 1.4 Finite Element Analysis

The components of the setup (e.g., die, blank holder, and hemispherical punch) were modelled based on the reference [9]. The numerical simulation of the stretch forming process was performed using ABAQUS6.1. The punch, die, and blank holder were modelled as discrete rigid bodies, while the sheet metal was modelled as a deformable material. Explicit surface-to-surface contact was established between the punch and blank, the blank and blank holder, and between the blank and die. An eight-node linear brick element (C3D8R) was used as a meshing element for the die, punch, and blank holder. Four-node linear tetrahedron elements were used as meshing elements for the blank. The punch is assigned the movement only in the  $z$  direction. The degrees of freedom in  $x$ ,  $y$  and  $z$  directions were arrested for the rest of the components in the die. A draw bead was created on the die to inhibit the material flow from the flange part where the blank holding force was applied in the  $z$ -direction. The quarter model is considered to reduce the simulation time; the meshing of components is shown in Fig.7. A Barlat-89 yield function material model is shown in Eq. (5) and the terms  $k_1$  and  $k_2$  are mentioned in Eq. (6). The experimentally determined material properties (i.e., yield strength, ultimate tensile strength, percentage of elongation, normal anisotropy, planar isotropy, strain hardening exponent and Poisson's ratio) were given as inputs for the material and are simulated by ABAQUS 6.1.

$$a |k_1 + k_2|^M + b |k_1 - k_2|^M + c |2k_2|^M = 2\sigma_e^M, \quad (5)$$

$$k_1 = \frac{(\sigma_x - h_{\sigma_y})}{2}; \quad k_2 = \left( \frac{\sigma_x - h_{\sigma_y}}{2} + p^2 \tau_{xy}^2 \right)^2, \quad (6)$$

where  $a$ ,  $b$ ,  $c$ , and  $p$  are anisotropic parameters,  $k_1$  and  $k_2$  coefficients,  $M$  invariants of the stress, and  $\sigma_x$  effective stress.

### 1.5 SEM Fracture Analysis

The micro-structural changes of sheet metal are examined using SEM. The behaviour of the sheet metal is predicted from SEM images. The main aim is to understand the limits and behaviour of the material and possible causes of failure under biaxial strain conditions. Narayanasamy and Narayanan [21] used SEM fractography to understand the fracture behaviour and formability of interstitial free steel. In this work, the SEM fractography was used to examine the fracture surface of an Inconel 718 alloy sheet obtained from a hemispherical punch method.

## 2 RESULTS AND DISCUSSION

### 2.1 Tensile Test Results

Mechanical properties, such as yield strength, ultimate tensile strength, elongation, anisotropy parameters, strain hardening and strength coefficient of Inconel 718 alloy sheet metal are determined in three different rolling directions; the results of the tests are shown in Tables 2 and 3.

**Table 2.** Tensile properties of Inconel alloy sheet

Direction	YS [N/mm <sup>2</sup> ]	UTS [N/mm <sup>2</sup> ]	Total % of elongation
0°	512.1	820.9	47.6
45°	545.3	942.5	43.9
90°	614.6	931.3	45.1

**Table 3.** Anisotropy properties & strain hardening exponent of Inconel alloy sheet

Direction	$r$ values	$R$	$\Delta R$	$n$	$K$
0°	1.18	1.03	-0.04	0.33	2022
45°	0.97	0.97		0.31	1564
90°	0.91	0.94		0.32	1522

where YS is yield strength, UTS ultimate tensile strength,  $r$  anisotropy parameter,  $R$  normal anisotropy,  $\Delta R$  planar anisotropy,  $n$  strain hardening exponent, and  $K$  strength coefficient.

Strain hardening  $n$  is found to be 0.33, which indicates good stretch ability and formability, whereas

normal anisotropy  $r$  is 1.02, which shows resistance to thinning while drawing. The total elongation is found to be maximum in the longitudinal rolling direction compared to the diagonal and traverse rolling directions. Prasad al. [19] and Ravi Kumar and Swaminathan [22] reported similar results in Inconel 718 alloy sheets and aluminium alloys. The Inconel 718 has a negative planar anisotropy of -0.04 which can result in earing in the diagonal rolling direction.

True stress and true strain values, engineering stress and strain values are plotted and are shown in Fig. 8. Based on the observed values, the Inconel 718 alloy sheet percentage of elongation and strength were found to be good in the rolling direction.

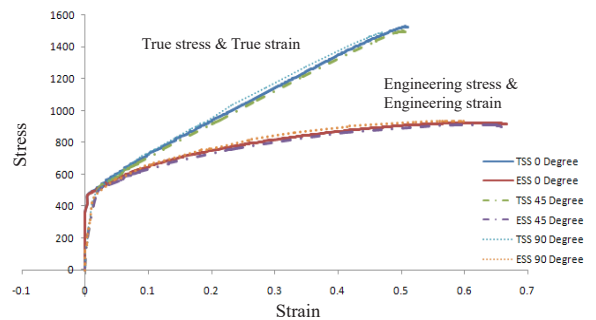


**Fig. 8.** True stress-strain curve vs engineering stress strain

True stress and true strain values, and engineering stress and strain values are plotted and are shown in Fig. 8. Based on the observed values, the Inconel 718 alloy sheet percentage of elongation and strength were found to be good in the rolling direction.

### 2.2 Experimental Results

A 100-ton hydraulic press and die setup shown in Fig. 9 is used for performing the hemispherical punch test and six specimens of sheet dimensions 200 mm × 200 mm, 200 mm × 180 mm, 200 mm × 160 mm, 200 mm × 140 mm, and 200 mm × 120 mm, 200 mm × 100 mm (shown in Fig. 10) are subjected to hemispherical punch test. A grid circle of Ø3 mm is marked on the specimens with an electrochemical-etching process. The specimens were clamped between the blank holder and the lower die rigidly with adequate blank holding force. Polyethylene sheet and Servo 4T 20w40 lubrication oil was applied to the sheet specimen for improving the flow of the material in hemispherical punch method. Prasad et al. [21] maintained a constant speed of 20 mm/min in the punch during stretch of specimen.



Fig. 9. 100-ton hydraulic press and die setup

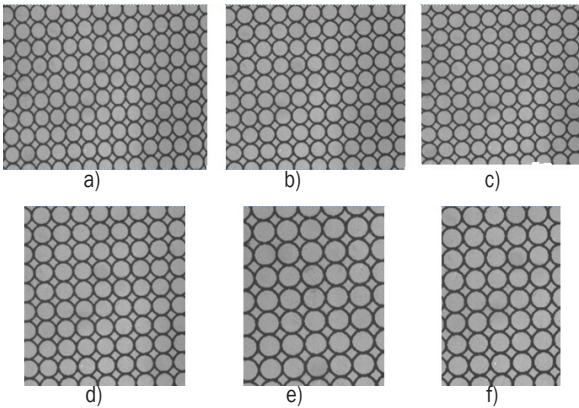


Fig. 10. Grid printed experimental specimen before deformation, a) 200 mm × 200 mm, b) 200 mm × 180 mm, c) 200 mm × 160 mm, d) 200 mm × 140 mm, e) 200 mm × 120 mm, f) 200 mm × 100 mm

Panickeret al. [23] showed that the onset of necking and failure of the specimen was monitored by a mirror mounted on the top of the die.

$$s_1 = \frac{D_1 - d_1}{D_1}, \quad (7)$$

$$s_2 = \frac{D_2 - d_1}{D_2}, \quad (8)$$

where  $s_1$  is major strain,  $s_2$  minor strain,  $D_1$  is ellipse major axis distance,  $D_2$  ellipse minor axis distance, and  $d_1$  gird circle diameter.

Eqs. (7) and (8) are used to determine the major and minor strains by measuring the diameters of the ellipses. The minor and major strains are measured using a Dalsa Corporation machine vision system and the pixel quality is 752 × 582. The accuracy is 0.1 mm is shown in Fig. 11. The Inconel 718 alloy sheet specimens deformed are shown in Fig. 12.

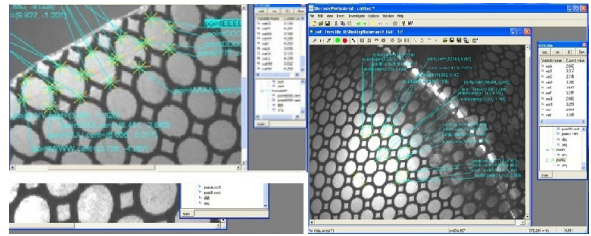


Fig. 11. Ellipse measured by using machine vision



Fig. 12. Fractured punch dome test specimen for evaluation of formability

The FLD diagram is plotted from the measured strain values obtained from various ellipses in fracture, necked and safe regions as shown in Fig. 13. The formability is measured by FLD and the point of intersection of FLD with the true major axis value is found to be 0.34. The minor strain is observed on the left side of the FLD and major strain is observed on the right side of the FLD, which is due to biaxial expansion. The formability knowledge of Inconel 718 alloy sheet material obtained can be used in sheet metal industries for failure prediction in the design stage and for minimizing the cost incurred in the trial-and-error method. The simulated LDH values obtained from ABAQUS 6.1 and experimental LDH values measured using the coordinate measuring machine (CMM) are listed in Table 4. The simulated and experimental LDH values were in close agreement; the error percentage was found to be less than 5 %.

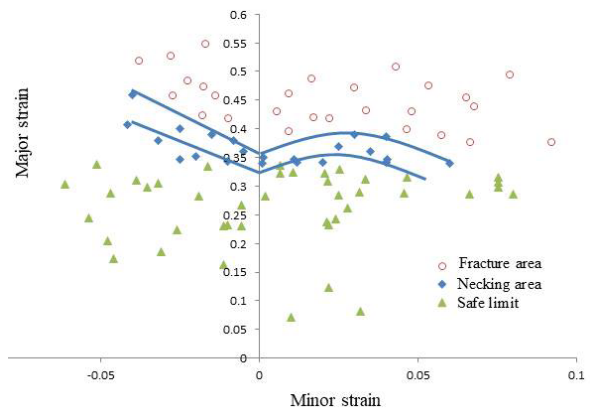
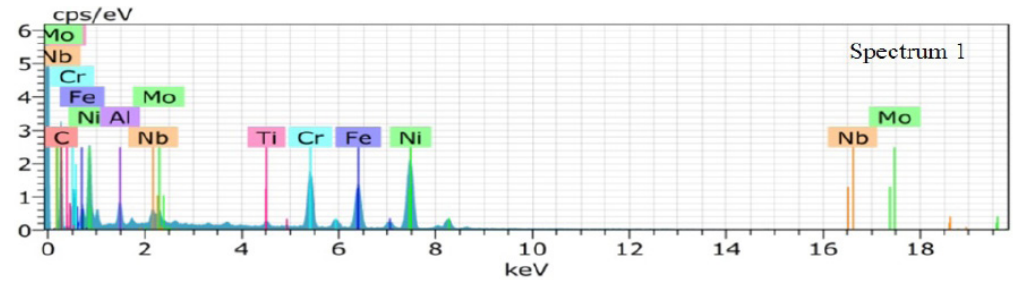
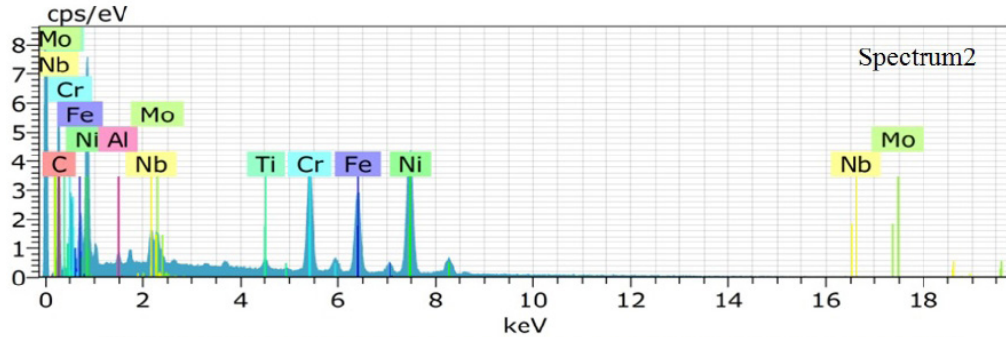


Fig. 13. Experimental forming limit diagram of Inconel 718 alloy sheet



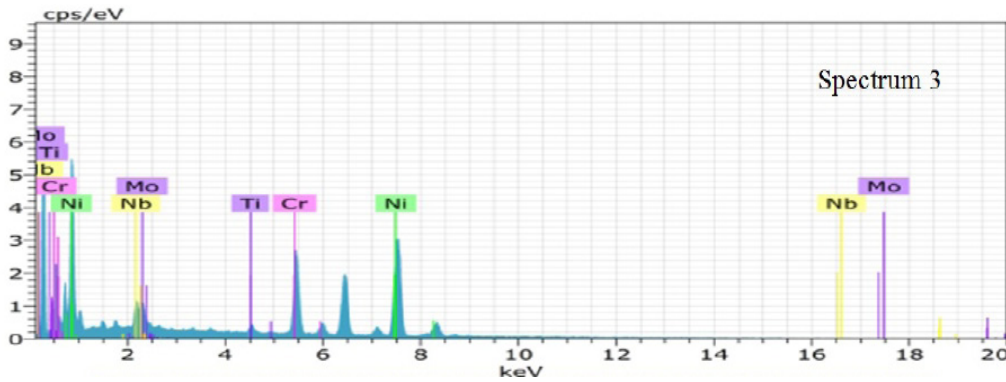
a)

Element	C K	Ni K	Fe K	Cr K	Nb K	Mo K	Ti K	Al K
Weight [%]	48.66	29.27	11.43	9.22	3.06	2.02	0.98	0.35



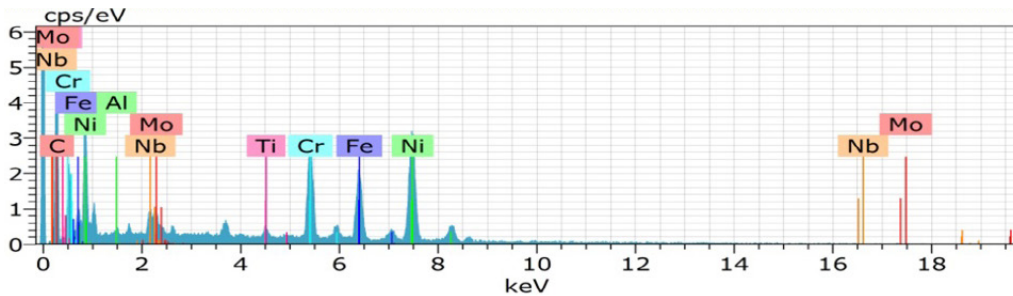
b)

Element	C K	Ni K	Fe K	Cr K	Nb K	Mo K	Ti K	Al K
Weight [%]	38.67	31.34	12.12	10.24	2.93	1.86	0.75	2.03



c)

Element	C K	Ni K	Fe K	Cr K	Nb K	Mo K	Ti K	Al K
Weight [%]	38.98	30.53	13.00	11.09	3.02	1.99	0.85	0.55



d)

Element	C K	Ni K	Fe K	Cr K	Nb K	Mo K	Ti K	Al K
Weight [%]	48.66	29.27	11.43	9.22	3.06	2.02	0.98	0.35

**Fig. 14.** EDS Element analysis for fractured specimen; a) 200 mm x 100 mm, b) 200 mm x 120 mm, c) 200 mm x 140 mm, and d) 200 mm x 160 mm

**Table 4.** The simulated LDH values from ABAQUS 6.1 and experimental LDH values using the CMM

Specimen [mm]	Simulated [mm]	Experimental (LDH) [mm]	Error [%]
200 × 100	50.65	48.6	-4.21
200 × 120	51.82	49.8	-2
200 × 140	52.25	50.2	-2
200 × 160	52.28	52.2	-0.08
200 × 180	52.83	53.2	0.69
200 × 200	53.01	53.3	0.03

### 2.3 Fractography Results

The features of the fracture are analysed using fractography. The fractography is performed using SEM. SEM examination of grid circle changes in the tension-tension region (right side of FLD) and tension-compression region (left side of FLD) is shown in Fig. 14. EDS analysis provides the details of the chemical composition of the enclosure in the vicinity of the fractured surface and is shown in Figs.

14a and b. The chemical compositions of materials examined at the fracture surface were similar to the composition identified in Table 1. Fractographs of 100 mm and 120 mm width specimens showed minimum minor strain and maximum major strain. The shallow dimples and minimum number of voids are observed in Fig. 14a and b. The blanks were subjected to plane strain condition resulting in pure ductile failure (Fig. 14 c and d). The 140 mm and 160 mm width specimen indicated a mixed plain strain condition in the majority of the region and in the circles examined in tension-tension region. Deep dimples and more numerous voids indicate shear and ductile fracture. The 200 mm width specimen indicated no necking or failure.

**Table 5.** FEA values for different specimens

Specimen [mm]	FEA [mm]	Specimen [mm]	FEA [mm]
200 × 100	50.63	200 × 160	52.28
200 × 120	51.82	200 × 180	52.83
200 × 140	52.20	200 × 200	53.01

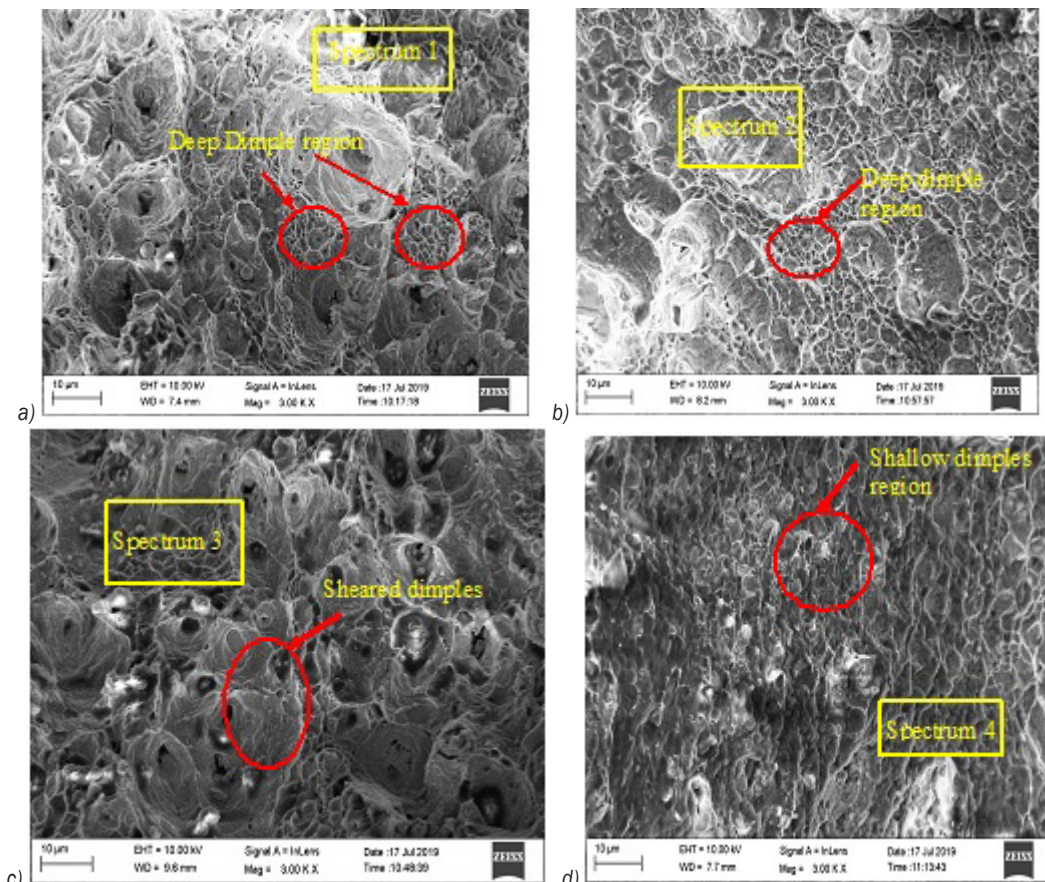


**Fig. 15.** Fractographs of Inconel 718 alloy sheet specimens in hemispherical punch test; ; a) 200 mm x 100 mm, b) 200 mm x 120 mm, c) 200 mm x 140 mm, and d) 200 mm x 160 mm

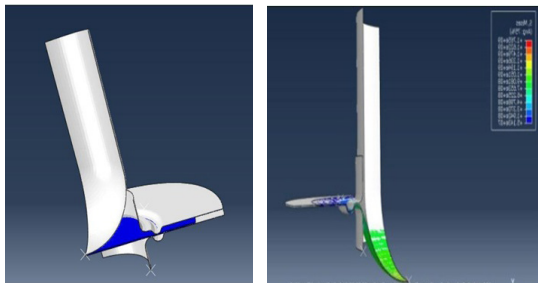


Fig. 16. Simulated LDH values different specimens in ABAQUS 6.1

The quarter finite element (FE) model strain distribution along the specimen is shown in Fig. 16. The detailed view of strain distribution in the Inconel 718 alloy sheet is presented in Fig. 17. FEA values are shown in Table 5.

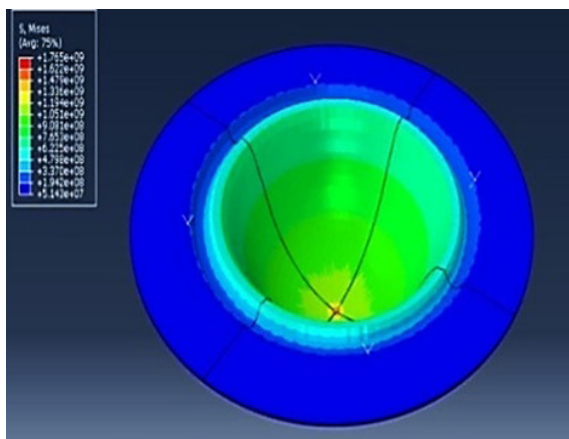


Fig. 17. Strain distributions in Inconel 718 alloy sheet

### 3 CONCLUSION

In this paper, the mechanical properties of Inconel 718 alloy sheet in longitudinal, diagonal, and traverse directions were obtained by uniaxial tensile test. Also, the LDH values of the Inconel 718 alloy sheet were examined by simulation and experimentation using a hemispherical punch method. The following are results obtained from this work.

The mechanical properties of the Inconel 718 alloy sheet of 1 mm thickness were obtained in different rolling directions. The percentage of elongation was high (47.6 %) in the rolling direction compared to other directions. The strain hardening  $n$  is found to be 0.34, which indicates good stretch ability and formability. The normal anisotropy  $r$  of 1.02 shows that material will resist thinning in drawing operation. The strength coefficient value also

indicated that the material possesses good strength in the transverse direction.

Inconel 718 alloy sheet properties observed in the rolling direction were used in ABAQUS 6.1 for finite element analysis. The strain distribution in the sample dimension of 200 mm  $\times$  200 mm indicated no necking or failure in both the simulation and experimentation. The LDH values obtained from FEA and experimental results were in good agreement. The error was found to be less than 5 %. This indicates that the developed FE model can further be used to study the material behaviour of other alloy sheets numerically thereby reducing the time and cost incurred in experiments.

FLD of the Inconel 718 sheet was obtained experimentally. The strain limit obtained is the safe region in which the material is susceptible to plastic deformation without failure. As the width of the specimen increases, the material resistance to plastic deformation also increases. SEM examination of 100 mm and 120 mm width fractured sheets showed pure ductile fracture. The strain distribution in the sample dimension of 120 mm  $\times$  140 mm indicated shear ductile fracture. The presence of alloying elements before and after failure is confirmed by EDS analysis.

### 4 ACKNOWLEDGEMENTS

The authors are thankful to the Quality Improvement Programme (QIP), Delhi, India for proving financial support and the Department of Production Engineering, PSG College of Technology, Coimbatore, Achariya College of Engineering Technology, Puducherry, India.

### 5 REFERENCES

- [1] Gupta, A.K., Ravi Kumar, R.D. (2006). Formability of galvanized interstitial-free steel sheets. *Journal of Materials Processing Technology*, vol. 172, no. 2, p. 225-237, DOI:10.1016/j.jmatprotec.2005.10.016.
- [2] Pérez Caro, L., Schill, M., Haller, K., Odenberger, E.-L., Oldenburg, M. (2020). Damage and fracture during sheet-metal forming of alloy 718. *International Journal of Material Forming*, vol. 13, p.15-28, DOI:10.1007/s12289-018-01461-4.
- [3] Reed, R.C. (2006). *The Superalloys Fundamentals and Applications*. Cambridge University Press, Cambridge, DOI:10.1017/CB09780511541285.
- [4] Anderson, M., Thielin, A.-L., Bridier, F., Bocher, P. Savoie, J. (2017).  $\delta$  phase precipitation in Inconel 718 and associated mechanical properties. *Materials Science and Engineering: A*, vol. 679, p. 48-55, DOI:10.1016/j.msea.2016.09.114.
- [5] Sajun Prasad, K., Kamal, T., Panda, S.K., Kar, S., Narayana Murty, S.V.S., Sharma, S.C. (2015). Finite element validation of forming limit diagram of IN-718 sheet metal. *Materials Today*:

- Proceedings*, vol. 2, no. 4-5, p. 2037-2045, DOI:10.1016/j.matpr.2015.07.174.
- [6] Banabic, D., Comsa, D.S., Eyckens, P., Kami, A., Gologanu, M. (2016). Advanced models for the prediction of forming limit curves. *Multiscale Modelling in Sheet Metal Forming*, Springer, Cham. p. 205-300, DOI:10.1007/978-3-319-44070-5\_5.
- [7] Jayahari, L., Hussaini, S.M., Dinesh Varmaa, Srividya Devi, P. (2020). Predictive study of Inconel718 mechanical properties at sub-zero temperature. *Advances in Materials and Processing Technologies*, vol. 6, no. 2, p. 233-243, DOI:10.1080/2374068X.2020.1731234.
- [8] Djavanroodi, F., Derogar, A. (2010). Experimental and numerical evaluation of forming limit diagram for Ti6Al4V titanium and Al6061-T6 aluminium alloys sheets. *Materials and Design*, vol. 31, p.4866-4875, DOI:10.1016/j.matdes.2010.05.030.
- [9] Narayanasamy, R., Narayanan, C.S. (2008). Forming, fracture and wrinkling limit diagram for if steel sheets of different thickness. *Materials & Design*, vol. 29, no. 7, p. 1467-1475, DOI:10.1016/j.matdes.2006.09.017.
- [10] Badr, O.M., Rolfe, B., Hodgson, P., Weiss, M. (2015). Forming of high strength titanium sheet at room temperature. *Materials & Design*, vol. 66, p. 618-626, DOI:10.1016/j.matdes.2014.03.008.
- [11] Toshniwal, K., Pareddy, S., Kotkunde, N., Gupta, A.K. (2017). Numerical investigation on stress based forming limit diagram for Ti-6Al-4V alloy. *Materials Today: Proceedings*, vol. 4, no. 8, p. 8096-8103, DOI:10.1016/j.matpr.2017.07.149.
- [12] Sudarsan, C., Banker, H.K., Hazra, S., Bhagat, R., Panda, S.K. (2019). Experimental investigations on forming limit diagram of ultra-thin SS304 steel effect of circular grid size, sheet orientation, punch size and deformation speed. *Advances in Materials and Processing Technologies*, vol. 5, no. 1, p. 25-38, DOI:10.1080/2374068X.2018.1510679.
- [13] Rahman, T., Bardelcik, A., Imbert, J., Butcher, C., Worswick, M.J. (2016). Effect of strain on flow stress and anisotropy of DP600, TRIP780, and AA5182-0 sheet metal alloys. *International Journal of Impact Engineering*, vol. 88, p. 72-90, DOI:10.1016/j.ijimpeng.2015.09.006.
- [14] Li, S.L., Kang, Y.L., Zhu, G.M., Kuang, S. (2015). Effects of strain rates on mechanical properties and fracture mechanism of DP780 dual phase steel. *Journal of Materials Engineering and Performance*, vol. 24, p. 2426-2434, DOI:10.1007/s11665-015-1495-0.
- [15] Mahalle, G., Kotkunde, N., Gupta, A.K., Singh, S.K. (2021). Efficacy of semi-empirical models for prediction of forming limit curve of IN718 alloy at elevated temperature. *Advances in Materials and Processing Technologies*, vol. 7, no. 4, p. 617-629, DOI:10.1080/2374068X.2020.1792706.
- [16] Paul, S.K. (2012). Predicting the flow behavior of metals under different strain rate and temperature through phenomenological modeling. *Computational Material Science*, vol. 65, p. 91-99, DOI:10.1016/j.commatsci.2012.06.039.
- [17] Paul, S.K. (2021). Control factors of forming limit curve: A review. *Advances in Industrial and Manufacturing Engineering*, vol. 2, art. ID 100033, DOI:10.1016/j.aime.2021.100033.
- [18] Paul, S.K. (2016). Prediction of complete forming limit diagram from tensile properties of various steel sheets by a nonlinear regression based approach. *Journal of Manufacturing Processes*, vol. 23, p. 192-200, DOI:10.1016/j.jmapro.2016.06.005.
- [19] Prasad, K.S., Panda, S.K., Kar, S.K., Sen, M., Murthy, N.S.V.S., Sharma, S.C. (2017). Microstructures, forming limit and failure analyses of Inconel718 sheets for fabrication of aerospace components. *Journal of Materials Engineering and Performance*, vol. 26, no. 4, p. 1513-1530, DOI:10.1007/s11665-017-2547-4.
- [20] Kotkunde, N., Srinivasan, S., Krishna, G., Gupta, A.K., Singh, S.K. (2016). Influence of material models on theoretical forming limit diagram prediction for Ti-6Al-4V alloy under warm condition. *Transaction of Nonferrous Metal Society of China*, vol. 26, no. 3, p. 736-746, DOI:10.1016/S1003-6326(16)64140-7.
- [21] Narayanasamy, R., Narayanan, C.S. (2007). Experimental analysis and evaluation of forming limit diagram for interstitial free steels. *Materials & Design*, vol. 28, no. 5, p. 1490-1512, DOI:10.1016/j.matdes.2006.03.010.
- [22] Ravi Kumar, D., Swaminathan, K. (1999). Formability of two aluminium alloys. *Materials Science and Technology*, vol. 15, no. 11, p. 1241-1252, DOI:10.1179/026708399101505347.
- [23] Panicker, S.S., Singh, H.G., Panda, S.K., Dashwood, R. (2015). Characterization of tensile properties, limiting strains, and deep drawing behavior of AA5754-H22 sheet at elevated temperature. *Journal of Materials Engineering and Performance*, vol. 24, p.4267-4282, DOI:10.1007/s11665-015-1740-6.

# Vsebina

**Strojniški vestnik - Journal of Mechanical Engineering**  
**letnik 68, (2022), številka 6**  
**Ljubljana, junij 2022**  
**ISSN 0039-2480**

**Izhaja mesečno**

## **Razširjeni povzetki (extended abstracts)**

- Balsam H. Abed, Ali A. Battawi, Abdul Wahab H. Khuder: Vpliv namakalnega medija na lezenje poliestrskega kompozita, ojačenega s piščančjim perjem SI 51
- Yunyue Xie, Qingliang Zeng, Kao Jiang, Zhaosheng Meng, Qinghai Li: Preiskava dinamičnega vedenja štirinožnega hidravličnega podporja pod vplivom dvojnih udarnih obremenitev SI 52
- HudaElsalam Mohamed, Unal Camdali, Atilla Biyikoglu, Metin Actas: Izboljšanje zmogljivosti kompresorskega hladilnega sistema z nanohladivom R134a + CuO/CeO<sub>2</sub> SI 53
- Tie Zhang, Yachao Cao, Guangcai Ma: Indeksi za vrednotenje zmogljivosti prenosa sile in omejitev pri paralelnih mehanizmih SI 54
- An-Le Van, Trung-Thanh Nguyen: Optimizacija varjenja z gnetenjem z optimalnim sistemom ANFIS po metodi Taguchi in z genetskim algoritmom SI 55
- Kanmani Ganesan, Saravanan Sambasivam, Rajesh Ramadass: Določitev vrednosti mejne višine polkrogle (LDH) za pločevino iz zlitine Inconel 718 po metodi polokroglega pestiča z eksperimenti in z analizo po metodi končnih elementov SI 56

## **In Memoriam**

Prof. dr. Matija Fajdiga

SI 57



# Vpliv namakalnega medija na lezenje poliestrskega kompozita, ojačenega s piščančjim perjem

Balsam H. Abed\* – Ali A. Battawi – Abdul Wahab H. Khuder  
Tehniški kolidž v Bagdadu, Srednja tehniška univerza, Irak

Kompozitni materiali se uveljavljajo v industrijskih aplikacijah po vsem svetu. Uporaba odpadkov kot je piščančje perje za ojačenje kompozitov lahko pomaga pri reševanju okoljskih problemov, saj gre za izkoriščanje obnovljivega in cenene materiala, ki ga je v izobilju. Ena glavnih prednosti kompozitov v primerjavi s klasičnimi materiali je njihova nizka masa. V članku je predstavljena preiskava vpliva medija za namakanje na lezenje poliestrskega kompozita, ojačenega s piščančjim perjem.

Kompozit je bil izdelan po postopku ročnega polaganja. Pripravljene so bili preizkušanci z različnim deležem vlaknena polnila (0 %, 0,2 %, 0,4 %, 0,6 % in 0,8 %), ki so bili nato namočeni v tri različne medije (KCl, NaOH in HNO<sub>3</sub>). Preskusi lezenja so bili opravljeni po standardih ASTM. Rezultati kažejo, da imajo kompoziti s piščančjim perjem, ki so bili namočeni v različne medije, odlične mehanske lastnosti v primerjavi s kompoziti brez ojačitve oziroma s kompoziti, ki niso bili namočeni. Pri poliestrskih kompozitih, ojačenih z 0,2 ut. % piščančjega perja in namočenih v kisel medij, je bila ugotovljena izboljšava časovnega raztezka v primerjavi s preizkušanci, namočenimi v druge medije, in s čistim poliestrom. Pri kompozitu z 0,4 ut. % piščančjega perja, namočenem v alkalnem mediju, je bila ugotovljena največja izboljšava časovne napetosti v primerjavi s čistim poliestrom in s preizkušanci, namočenimi v druge medije. Slani medij je najbolj izboljšal modul elastičnosti poliestrskega kompozita z 0,8 ut. % piščančjih vlaken v primerjavi s čistim poliestrom in preizkušanci, namočenimi v druge medije.

Pregled literature je pokazal, da je mogoče že z majhnim utežnim deležem piščančjega perja izboljšati mehanske lastnosti poliestrskih kompozitov. Odpadki kot naravna surovina se uporabljajo v različnih industrijah, študija pa poudarja potrebo po recikliranju kompozitov in njihovi uporabi v novih aplikacijah. Naravna vlakna bodo po napovedih že v bližnji prihodnosti zamenjala sintetične polimere vsaj v specializiranih aplikacijah. Naravna vlakna so lahko dobra zamenjava za sintetična vlakna, če ni zahtevana dolga življenjska doba izdelkov. Možnosti uporabe vlaken živalskega izvora za ojačitev kompozitov še niso popolnoma izkoriščene. Proizvodnja tovrstnih kompozitov je omejena zaradi pomanjkanja vlaken in uporaba perja je zato aktivno raziskovalno področje. Odpadki se v takih končnih izdelkih pretvorijo v dodano vrednost.

Prihodnje raziskave bodo zajele še druga naravna vlakna, kot so volna, konjska žima, človeški lasje, svila, juta, kokosova vlakna itd.

**Ključne besede:** namakanje, piščančje perje, poliestrski kompozit, lezenje, ojačitev

# Preiskava dinamičnega vedenja štirinožnega hidravličnega podporja pod vplivom dvojnih udarnih obremenitev

Yunyue Xie<sup>1</sup> – Qingliang Zeng<sup>2</sup> – Kao Jiang<sup>3</sup> – Zhaosheng Meng<sup>3</sup>, \* – Qinghai Li<sup>3</sup> – Junming Zhang<sup>3</sup>

<sup>1</sup> Znanstveno-tehniška univerza v Shandongu, Državni laboratorij v Shandongu  
za preprečevanje nesreč v gradbeništvu in blažitev njihovih posledic, Kitajska

<sup>2</sup> Znanstveno-tehniška univerza v Shandongu, Kolidž za strojništvo in elektroniko, Kitajska

<sup>3</sup> Znanstveno-tehniška univerza v Shandongu, Državni laboratorij za preprečevanje nesreč v rudarstvu,  
ki ga sofinancirata provinca Shandong ter Ministrstvo za znanost in tehnologijo, Kitajska

Premog je glavni primarni energijski vir na Kitajskem, hidravlična podporja pa imajo pomembno vlogo v podzemnem premogovništvu. Pogoste udarne obremenitve med rudarjenjem zlahka poškodujejo tečaje ter zmanjšajo stabilnost hidravličnega podporja. Zato je bila opravljena študija za preučitev dinamičnega odgovora hidravličnega podporja pod vplivom udarnih obremenitev in izboljšanje njegove stabilnosti.

V ta namen je bil v programskem paketu Hypermesh pripravljen togo-fleksibilni sklopljeni numerični model podporja. Osnova je toga in povezana s podlago (spodnja ploskev osnove je omejena), stropnik, ščit ter sprednja in zadnja lemniskata pa so fleksibilni. Sistem sprednjih in zadnjih stojk je modeliran z ekvivalentnim sistemom vzmeti in blažilnikov. Z uporabo nazivne statične delovne nosilnosti na modelu podporja je bila določena togost hidravličnega podporja pod statično obremenitvijo in na podlagi omenjenih rezultatov je bila nato ocenjena uporabnost modela. Sledili so udarni preizkusi hidravličnega podporja. Za boljšo simulacijo naključnosti udarnih obremenitev so bile uporabljene enojne in dvojne udarne obremenitve. Analizirane so bile sile v tečajih in vibracije sistema stojk, ko sta stropnik in ščitnik podvržena udarnim obremenitvam.

Rezultati so pokazali, da je najbolj občutljiv tečaj sprednje stojke (139,4 %), ko udarne obremenitve prenaša samo stropnik. Dinamični odgovor vseh tečajev na hidravličnem podporju (razen na zadnji stojki) doseže vršno vrednost, ko udarne obremenitve delujejo na stropnik in na ščitnik. Ko se udarne obremenitve pomikajo nazaj po ščitu, se spreminja tudi razbremenitev pritiska na tečaj.

Hidravlično podporje je mogoče obravnavati kot paralelni ročni mehanizem. Pri analizi mehanskih lastnosti takih mehanizmov je pomembna zračnost med členi. Zaradi kompleksnosti numeričnega modela in omejene računske moči so bili zgibi med deli podporja v okviru te študije modelirani kot idealni zgibi. Tak pristop seveda ne omogoča popolnega opisa realnega mehanskega odgovora hidravličnega podporja in avtorji bodo zato v prihodnje skušali oblikovati dinamični model hidravličnega podporja ob upoštevanju zračnosti v zgibih za izboljšanje teorije dinamike hidravličnega podporja.

Predmet raziskave je štirinožno hidravlično podporje. Oblikovan je bil togo-fleksibilni sklopljeni numerični model podporja za preučitev njegovih dinamičnih lastnosti. Podana je primerjava dinamičnega odgovora štirinožnega hidravličnega podporja v pogojih brez obremenitve, enojnih udarnih obremenitev in dvojnih udarnih obremenitev, s čimer je bila dokazana potreba po preučitvi dinamičnega vedenja štirinožnega podporja pod dvojnimi udarnimi obremenitvami. Odgovor tečajev na statične sile in togost podporja sta bila analizirana za primer statične obremenitve stropnika. Dinamični odgovor podporja na dvojne udarne obremenitve je bil analiziran z uporabo naključnih udarnih obremenitev stropnika in ščita. Študija tako podaja nove raziskovalne metode in pristope za analizo dinamičnih lastnosti druge mehanske opreme.

**Ključne besede:** udarna obremenitev, štirinožno hidravlično podporje, dvojni udarci, prenos sil, numerična simulacija, dinamične lastnosti, zveza brez zračnosti

# Izboljšanje zmogljivosti kompresorskega hladilnega sistema z nanohladivom R134a + CuO/CeO<sub>2</sub>

HudaElsam Mohamed<sup>1,\*</sup> – Unal Camdali<sup>1</sup> – Atilla Biyikoglu<sup>2</sup> – Metin Actas<sup>3</sup>

<sup>1</sup> Univerza Yildirim Beyazit v Ankari, Oddelek za strojništvo, Turčija

<sup>2</sup> Univerza Gazi, Oddelek za strojništvo, Turčija

<sup>3</sup> Univerza Yildirim Beyazit v Ankari, Oddelek za energetiko, Turčija

V pričujoči raziskavi je bila najprej opravljena eksperimentalna in teoretična študija zmogljivosti kompresorskega hladilnega sistema (VCRS) s hladilnim sredstvom R134a brez dodanih nanodelcev. Ujemanje eksperimentalnih in teoretičnih rezultatov je bilo skoraj 98-odstotno. V drugem koraku je bila uporabljena programska oprema Ansys Fluent za teoretično analizo vpliva dodanih nanodelcev ter preverjanje možnosti za izboljšanje hladilnega števila sistema z zmesjo bakrovih in cerijeve oksidov.

Večina novejših študij na zadevnem področju obravnava uporabo kovin, kovinskih oksidov in hibridnih zmesi oksidov v hladilnih sistemih. Hibridne zmesi so v zadnjih letih pritegnile pozornost raziskovalcev, saj izboljšajo termofizikalne lastnosti in dolgotrajno stabilnost delcev v osnovnem hladilnem sredstvu. Nanodelci za raziskavo so bili pripravljene na cenen in preprost način kot preprosti oksidi ter kot zmesi bakrovih in cerijeve oksidov. Način priprave in surovine za pripravo nanodelcev so na voljo v vsakem kemijskem laboratoriju. S tem je odpravljena stroškovna bariera pri uporabi nanodelcev in je omogočeno želeno izboljšanje toplotne prevodnosti ob sprejemljivih stroških.

Opravljeni so bili eksperimenti z VCRS, ki je bil napolnjen s hladilnim sredstvom R134a. Temperature in tlaki na vstopu in na izstopu kompresorja, kondenzatorja in uparjalnika so bili merjeni z digitalnimi merilniki. Za nadzor nad rabo električne energije je bil uporabljen digitalni merilnik moči, za spremljanje masnega toka sredstva R134a pa digitalni merilnik pretoka. Vsak eksperiment je bil opravljen trikrat za točno določitev zmogljivosti v stacionarnem stanju. Vrednost hladilnega števila je bila izračunana na osnovi spremembe entalpije hladiiva. V naslednjem koraku je bilo pripravljenih sedem različnih vrst nanodelcev, ki so bili dodani v hladilni sistem za teoretično analizo vpliva na hladilno število.

Za opredelitev vpliva povprečne temperature v uparjalniku in kondenzatorju na hladilno število in na rabo energije je bil zasnovan teoretični model uparjalnika in kondenzatorja s specifikacijami, podobnimi kot pri eksperimentalnem sistemu. Rezultati se ujemajo z izsledki predhodnih študij: hladilno število se povečuje s temperaturo v uparjalniku ter zmanjšuje s povišanjem temperature v kondenzatorju, raba energije pa pada s povišanjem povprečne temperature v uparjalniku oz. narašča z višanjem povprečne temperature v kondenzatorju. Rezultati teoretične analize vpliva dodajanja različnih nanodelcev potrjujejo, da se v vsakem primeru izboljša hladilno število hladilnega sistema.

V pričujoči raziskavi je predstavljen koncept novih nanodelcev, ki bi lahko v prihodnosti odgovoril na mnoga vprašanja. Med drugim je bila uporabljena zmes cerijevega in bakrovega oksida. Rezultati za bakrov oksid se ujemajo s prejšnjimi študijami, ki so dokazale izboljšanje zmogljivosti hladilnega sistema in 25-odstotno povišanje hladilnega števila. Z dodatkom cerijevega oksida se je zmogljivost sistema izboljšala v manjši meri. Rezultati dodajanja zmesi so boljši pri večjem deležu bakrovega oksida.

Predstavljeni način priprave nanodelcev je preprost in cenovno dosegljiv. Nadaljnje raziskave bodo pokazale, ali je primeren tudi za pridobivanje drugih oksidov, zlasti tistih z visoko toplotno prevodnostjo. Raziskovalce spodbuja tudi k eksperimentalnim študijam vedenja cerijevega oksida v hladilnih sistemih in pri različnih temperaturah. Podana so tudi priporočila za izboljšanje rezultatov z dodajanjem zmesi, pripravljenih z drugimi hladiivi in mazalnimi olji.

**Ključne besede:** kompresorski hladilni sistem, hladilno število, nanohladivo, nanodelci

# Indeksi za vrednotenje zmogljivosti prenosa sile in omejitev pri paralelnih mehanizmih

Tie Zhang\* – Yachao Cao – Guangcai Ma

Tehniška univerza Južne Kitajske, Šola za strojništvo in avtomobilsko tehniko, Kitajska

Večina indeksov za opisovanje prenosa sil je odvisnih od koordinatnega sistema, kar lahko pri paralelnih mehanizmih privede do različnih rezultatov pri izbiri različnih referenčnih koordinatnih sistemov. Obstoječi indeksi zmogljivosti tudi merijo samo prenos po enem kraku in ne po celotnem paralelnem mehanizmu, prav tako pa nekateri indeksi niso homogeni. Na voljo je le malo člankov, ki bi obravnavali omejitve pri prenosu sil ter doslednost odpora proti deformaciji.

Na podlagi singularnega razcepa ter možne sestave matrike prenosa in omejitev sta bila izpeljana indeksa za šest primerov: indeks manipulabilnosti prenosa sile (TMI) in indeks doslednosti omejitve sil (CCI).

Za metodološko podlago so bili izbrani teorija vijaka, singularni razcep in vrednotenje zmogljivosti.

Predlagana indeksa TMI in CCI imata naslednje lastnosti:

- (1) TMI in CCI kot brezdimenzijska indeksa sta neodvisna od koordinatnega sistema, s čimer se je mogoče izogniti odstopanjem pri izbiri različnih referenčnih koordinatnih sistemov;
- (2) območje vrednosti indeksov TMI in CCI je od 0 do 1, kar omogoča intuitivne meritve in primerjavo brez vpliva ostalih dejavnikov paralelnega mehanizma (npr. različne dolžine palic);
- (3) ob uporabi predlaganega indeksa CCI za vrednotenje doslednosti omejitev PM z manjšo mobilnostjo je treba v večini primerov analizirati samo mobilnost.

Dokler je gibanje omejeno v smeri nemobilnosti, je kakovost omejevanja pogosto prezrta. Predlagani indeks CCI omogoča vrednotenje doslednosti omejevalne sile upora proti deformaciji za boljšo analizo PM z nizko mobilnostjo. Indeks TMI in CCI sta bila uporabljena pri paralelnem mehanizmu 4-URU z mešanim gibanjem, paralelnem mehanizmu 2-UPR+SPR s parazitskim gibanjem in čistem translacijskem mehanizmu 3-CRU. Ovrednoteni sta bili manipulabilnost prenosa sile in doslednost omejitvene sile omenjenih mehanizmov.

Nova indeksa TMI in CCI omogočata vrednotenje manipulabilnosti prenosa sile in doslednosti odpora proti deformaciji. Formule so bile izpeljane ob pogoju, da sta matriki prenosa in omejitev sestavljeni iz linearnih vektorjev sil, dvojic sil ali obojega. Prvič je bila zasnovana konfiguracija paralelnega mehanizma 3-CRU z maksimalno vrednostjo TMI in CCI, kar pomeni, da TWS in CMW ne povzročata nobene deformacije na premični platformi ter da sta doseženi najboljša manipulabilnost in doslednost v celotnem delovnem prostoru.

**Ključne besede:** manipulabilnost prenosa sile, doslednost omejevanja sile, vijak izvina prenosa, vijak izvina omejitev, paralelni mehanizem, teorija vijaka

# Optimizacija varjenja z gnetenjem z optimalnim sistemom ANFIS po metodi Taguchi in z genetskim algoritmom

An-Le Van<sup>1</sup> – Trung-Thanh Nguyen<sup>2,\*</sup>

<sup>1</sup> Univerza Nguyen Tat Thanh, Tehniška fakulteta, Ho Chi Minh, Vietnam

<sup>2</sup> Tehniška univerza Le Quy Don, Fakulteta za strojništvo, Ha Noi, Vietnam

Pričujoče delo obravnava analizo in optimizacijo varjenja aluminijeve zlitine z gnetenjem s cilji zmanjšanja specifične energije varjenja (SWE), izboljšanja učinkovitosti spajanja (JE) ter povečanja mikrotrdote (MH) v območju zvarnega spoja.

Varjenje z gnetenjem je učinkovit postopek varjenja v trdnem stanju, pri katerem orodje plastično deformira material in ga premeša za izdelavo močnega zvara. Izbira optimalnih parametrov varjenja z gnetenjem za manjšo rabo energije in izboljšanje kakovosti zvarov (porušitvene natezne trdnosti in mikrotrdote) do sedaj še ni bila raziskana.

Za določitev odgovorov pri varjenju z izbranimi parametri so bili uporabljeni modeli z optimalnim adaptivnim nevro-mehkim inferenčnim sistemom (ANFIS), za optimizacijo delovnih parametrov ANFIS pa je bila uporabljena metoda Taguchi. Najboljša rešitev je bila določena z genetskim algoritmom s kultiviranjem soseščine (NCGA).

Rezultati in ugotovitve raziskave:

- Pri optimalni rešitvi se je vrednost SWE zmanjšala za 17,0 %, medtem ko sta se vrednosti JE in MH izboljšali za 2,3 in 6,4 %.
- Optimalni modeli odgovorov pri varjenju ANFIS so primerni in zanesljivo napovedujejo vrednosti odgovorov.
- Ugotovitve so pomembne za določitev optimalnih parametrov varjenja z gnetenjem in izboljšanje odgovorov pri varjenju.

Članek daje naslednje prispevke na raziskovalnem področju:

- Razvita optimizacijska metoda, ki vključuje metode Taguchi, ANFIS in NCGA, predstavlja učinkovit pristop za reševanje kompleksnih izzivov pri optimizaciji ter izbiri optimalnih izidov. Ta pristop ponuja več prednosti, kot so nizki eksperimentalni stroški, manj človeških naporov in preprosta implementacija. Razvito tehniko je mogoče učinkovito uporabiti za optimizacijo varjenja ali drugih obdelovalnih procesov.
- V članku je podrobno analiziran vpliv parametrov procesa na odgovore pri varjenju z gnetenjem. To znanje bo operaterjem strojev lahko pomagalo do poglobljenega razumevanja fizikalnih dogajanj pri varjenju zlitine AA6061 z gnetenjem.
- Rezultate študije bo mogoče uporabiti tudi pri prihodnjih raziskavah ter pri razvoju ekspertnih sistemov za procese varjenja z gnetenjem.

**Ključne besede:** varjenje z gnetenjem, energijska učinkovitost, učinkovitost spajanja, mikrotrdota, NCGA

# Določitev vrednosti mejne višine polkrogle (LDH) za pločevino iz zlitine Inconel 718 po metodi polokroglega pestiča z eksperimenti in z analizo po metodi končnih elementov

Kanmani Ganesan\* – Saravanan Sambasivam – Rajesh Ramadass  
Tehniški kolidž PSG, Coimbatore, Tamil Nadu, Indija

Glavni cilj raziskave je določitev vrednosti mejne višine polkrogle (LDH) za 1 mm debelo pločevino iz zlitine Inconel 718, in sicer eksperimentalno ter z analizo po MKE (metoda končnih elementov) po metodi polokroglega pestiča in pri sobni temperaturi.

Pločevina iz Inconela 718 je med preoblikovanjem izpostavljena kombinaciji tlačnih in nateznih obremenitev. Plastična deformacija, ki jo material vzdrži brez porušitve, je lastnost materiala. Inconel 718 se uporablja v letalski industriji, za izdelavo vodilnih lopatic ter delov visokotlačnih kompresorjev in plinskih turbin. Vrednosti LDH za 1 mm debelo pločevino iz zlitine Inconel 718 so bile določene eksperimentalno ter z analizo po MKE po metodi polokroglega pestiča.

Mehanske lastnosti pločevine Inconel 718 iz nateznega preizkusa so bile uporabljene kot vhodni podatki v programskem paketu za analizo po MKE. Za napovedovanje vrednosti LDH je bil uporabljen model z deformacijsko funkcijo Barlat-89. Podana je primerjava vrednosti LDH, pridobljenih eksperimentalno in z analizo po MKE. Pri delu so bile uporabljene teoretične osnove preoblikovanja kovin.

Eksperimentalno določene vrednosti LDH za pločevino iz Inconela 718 se dobro ujemajo z rezultati simulacij v programski opremi ABAQUS 6.1. Raziskovalci bodo lahko uporabili predlagani pristop za določanje vrednosti LDH tudi pri drugih materialih. Na osnovi rezultatov eksperimentov je bila določena mejna krivulja, ki zagotavlja varno delovno območje za pločevino iz Inconela 718. Analiza 100 mm in 120 mm širokih preizkušancev z vrstičnim elektronskim mikroskopom (SEM) je pokazala gladko površino in duktilni zlom. Med preiskavo preizkušancev širine 140 mm in 160 mm sta bili odkriti groba površina in strižno-duktilni zlom. Analiza površine preloma z energijsko disperzijskim spektrometrom (EDS) je potrdila sestavo pločevine pred porušitvijo.

**Ključne besede:** pločevina iz zlitine Inconel 718, natezni preizkus, metoda polokroglega pestiča, metoda končnih elementov, LDH, elektronski mikroskop, energijsko disperzijski spektrometer

## Prof. dr. Matija Fajdiga (1941-2022)



Zapustil nas je zaslužni profesor Fakultete za strojništvo Univerze v Ljubljani prof. dr. Matija Fajdiga. Rojen je bil leta 1941 v Sodražici, kjer je preživel mladostna leta in obiskoval osnovno šolo. Kasneje se je šolal na Srednji tehnični šoli v Ljubljani, na Fakulteti za strojništvo v Ljubljani pa je diplomiral leta 1963. Leta 1973 je magistriral, leta 1975 pa doktoriral iz področja obratovalne trdnosti motornih vozil. Leta 1975 je postal učitelj z nazivom docent. Leta 1981 je bil izvoljen v naziv izrednega profesorja in leta 1996 v naziv rednega profesorja. Svoje pedagoško delo na fakulteti je zaključil leta 2011, od takrat do upokojitve leta 2013 opravljal naloge znanstvenega svetnika.

Raziskovalno delo je pričel leta 1968 v okviru Katedre za konstruiranje, ki jo je vodil zasl. prof. dr. Jože Hlebanja. Kasneje je opravljal samostojne raziskave iz področja obratovalne trdnosti. V okviru dolgoročnega sodelovanja s podjetji je koncipiral in zgradil preskuševališča za transmisijske elemente vozil, za merjenje sojemalnih sil v jeklenih vrveh, za zavore vozil, itn. S tem je Fakulteta za strojništvo Univerze v Ljubljani v tistem času pridobila ugled odlične in vodilne raziskovalne ustanove na področju motornih vozil na območju bivše Jugoslavije. Med leti 1976 in 1980 je bil predsednik Odbora za žičnice in vlečnice pri Skupščini Republike Slovenije. V tem času je bila sprejeta osnovna zakonodaja za žičnice in vlečnice, ter pravilniki o tehničnih prevzemih, za katere je profesor koncipiral postopek preskusov in preskusno opremo. Leta 1982 je bil med ustanovitelji raziskovalnega polja Konstruiranje. Znotraj polja je prevzel raziskovalno skupino za Razvojna vrednotenja. Leta 1985 je ustanovil Laboratorij za razvojna vrednotenja – LAVEK. V okviru laboratorija je potekalo zelo intenzivno dolgoročno sodelovanje z jugoslovansko, kasneje po letu 1990, pa s slovensko industrijo.

Več let je bil predstojnik Katedre za strojne elemente in konstruiranje, ki je takrat združevala obsežen pedagoški program in pet laboratorijev. Leta 2002 je ustanovil Programsko skupino za razvojna vrednotenja. S tem je uveljavil obratovalno trdnost kot samostojno znanstveno področje. Sočasno je poskrbel, da je bilo novo znanje iz obratovalne trdnosti ves čas aplikativno preverjano v sodelovanju z industrijo. Raziskave, aplikativno delo z industrijo in mednarodno sodelovanje so omogočili, da se je v konstruiranju uveljavila eksperimentalna tehnika in probabilistični koncept projektiranja izdelkov. Vse to delo je omogočilo, da je zasl. prof. dr. Matija Fajdiga leta 2005 ustanovil samostojno Katedro za strojne elemente in razvojna vrednotenja.

V sodelovanju s skupino propulzivnih podjetij je leta 2002 na Fakulteti za strojništvo Univerze v Ljubljani ustanovil Center za razvojna vrednotenja (CRV), pri katerem je bil nosilni Laboratorij za vrednotenje konstrukcij (LAVEK). V njem je raziskovalna skupina skozi aplikacije preverjala temeljno znanje, usposabljala razvojne inženirje in omogočala povezavo dodiplomskih in podiplomskih študentov s prakso. Leta 2003 je bil pobudnik in soustanovitelj Avtomobilskega grozda Slovenije – ACS in tri mandate predsednik nadzornega sveta ACS. V ACS se še dandanes med seboj in s tujino uspešno povezujejo slovenski avtomobilski razvojni dobavitelji.

Predvsem pa je bil zasl. prof. dr. Matija Fajdiga enkratni predavatelj in pedagog Fakultete za strojništvo Univerze v Ljubljani. Bil je mentor več kot 100 študentom, 19 magistrantom in 18 doktorandom. Na matični fakulteti in na univerzi je opravljal različne pomembne funkcije. Bil je član in predsednik Upravnega odbora Fakultete za strojništvo, prodekan za raziskovalno delo na Fakulteti za strojništvo, dekan Fakultete za strojništvo, član upravnega odbora Univerze v Ljubljani, član senata Fakultete za strojništvo. V svojem dolgoletnem delu je dobil več priznanj za svoj pedagoški, raziskovalni, strokovni in družbeni angažma: red zaslug za narod s srebrno zvezdo Republike Slovenije, priznanje za uspešno delo na Fakulteti za strojništvo Univerze v Ljubljani, številna priznanja za uspešno sodelovanje od slovenskih in jugoslovanskih podjetij, zlato plaketo Univerze v Ljubljani ter nagrado za življenjsko delo Zveze strojnih inženirjev Slovenije.

Zasl. prof. dr. Matija Fajdiga je pustil globok pečat tako na Fakulteti za strojništvo, kot tudi na celotni Univerzi v Ljubljani. Zaradi tega ga bomo v trajnem spominu ohranili tako njegovi sodelavci, s katerimi je soustvarjal odmevne zgodbe o uspehih, kot tudi študentje, katerim je nesebično razdajal svoje obsežno strokovno znanje.

*Zapisal:  
prof. dr. Jernej Klemenc*

# Guide for Authors

All manuscripts must be in English. Pages should be numbered sequentially. The manuscript should be composed in accordance with the Article Template given above. The suggested length of contributions is 10 to 20 pages. Longer contributions will only be accepted if authors provide justification in a cover letter. For full instructions see the Information for Authors section on the journal's website: <http://en.sv-jme.eu>.

## SUBMISSION:

Submission to SV-JME is made with the implicit understanding that neither the manuscript nor the essence of its content has been published previously either in whole or in part and that it is not being considered for publication elsewhere. All the listed authors should have agreed on the content and the corresponding (submitting) author is responsible for having ensured that this agreement has been reached. The acceptance of an article is based entirely on its scientific merit, as judged by peer review. Scientific articles comprising simulations only will not be accepted for publication; simulations must be accompanied by experimental results carried out to confirm or deny the accuracy of the simulation. Every manuscript submitted to the SV-JME undergoes a peer-review process.

The authors are kindly invited to submit the paper through our web site: <http://ojs.sv-jme.eu>. The Author is able to track the submission through the editorial process - as well as participate in the copyediting and proofreading of submissions accepted for publication - by logging in, and using the username and password provided.

## SUBMISSION CONTENT:

The typical submission material consists of:

- A **manuscript** (A PDF file, with title, all authors with affiliations, abstract, keywords, highlights, inserted figures and tables and references),
- Supplementary files:
  - a **manuscript** in a WORD file format
  - a **cover letter** (please see instructions for composing the cover letter)
  - a ZIP file containing **figures** in high resolution in one of the graphical formats (please see instructions for preparing the figure files)
  - possible **appendices** (optional), cover materials, video materials, etc.

Incomplete or improperly prepared submissions will be rejected with explanatory comments provided. In this case we will kindly ask the authors to carefully read the Information for Authors and to resubmit their manuscripts taking into consideration our comments.

## COVER LETTER INSTRUCTIONS:

Please add a **cover letter** stating the following information about the submitted paper:

1. Paper **title**, list of **authors** and their **affiliations**. **One** corresponding author should be provided.
2. **Type of paper**: original scientific paper (1.01), review scientific paper (1.02) or short scientific paper (1.03).
3. A **declaration** that neither the manuscript nor the essence of its content has been published in whole or in part previously and that it is not being considered for publication elsewhere.
4. State the **value of the paper** or its practical, theoretical and scientific implications. What is new in the paper with respect to the state-of-the-art in the published papers? Do not repeat the content of your abstract for this purpose.
5. We kindly ask you to suggest at least two **reviewers** for your paper and give us their names, their full affiliation and contact information, and their scientific research interest. The suggested reviewers should have at least two relevant references (with an impact factor) to the scientific field concerned; they should not be from the same country as the authors and should have no close connection with the authors.

## FORMAT OF THE MANUSCRIPT:

The manuscript should be composed in accordance with the Article Template. The manuscript should be written in the following format:

- A **Title** that adequately describes the content of the manuscript.
- A list of **Authors** and their **affiliations**.
- An **Abstract** that should not exceed 250 words. The Abstract should state the principal objectives and the scope of the investigation, as well as the methodology employed. It should summarize the results and state the principal conclusions.
- 4 to 6 significant **key words** should follow the abstract to aid indexing.
- 4 to 6 **highlights**; a short collection of bullet points that convey the core findings and provide readers with a quick textual overview of the article. These four to six bullet points should describe the essence of the research (e.g. results or conclusions) and highlight what is distinctive about it.
- An **Introduction** that should provide a review of recent literature and sufficient background information to allow the results of the article to be understood and evaluated.
- A **Methods** section detailing the theoretical or experimental methods used.
- An **Experimental section** that should provide details of the experimental set-up and the methods used to obtain the results.
- A **Results** section that should clearly and concisely present the data, using figures and tables where appropriate.
- A **Discussion** section that should describe the relationships and generalizations shown by the results and discuss the significance of the results, making comparisons with previously published work. (It may be appropriate to combine the Results and Discussion sections into a single section to improve clarity.)
- A **Conclusions** section that should present one or more conclusions drawn from the results and subsequent discussion and should not duplicate the Abstract.
- **Acknowledgement** (optional) of collaboration or preparation assistance may be included. Please note the source of funding for the research.
- **Nomenclature** (optional). Papers with many symbols should have a nomenclature that defines all symbols with units, inserted above the references. If one is used, it must contain all the symbols used in the manuscript and the definitions should not be repeated in the text. In all cases, identify the symbols used if they are not widely recognized in the profession. Define acronyms in the text, not in the nomenclature.
- **References** must be cited consecutively in the text using square brackets [1] and collected together in a reference list at the end of the manuscript.
- **Appendix(-ices)** if any.

## SPECIAL NOTES

**Units:** The SI system of units for nomenclature, symbols and abbreviations should be followed closely. Symbols for physical quantities in the text should be written in italics (e.g.

*v*, *T*, *n*, etc.). Symbols for units that consist of letters should be in plain text (e.g. ms<sup>-1</sup>, K, min, mm, etc.). Please also see: <http://physics.nist.gov/cuu/pdf/sp811.pdf>.

**Abbreviations** should be spelt out in full on first appearance followed by the abbreviation in parentheses, e.g. variable time geometry (VTG). The meaning of symbols and units belonging to symbols should be explained in each case or cited in a **nomenclature** section at the end of the manuscript before the References.

**Figures** (figures, graphs, illustrations digital images, photographs) must be cited in consecutive numerical order in the text and referred to in both the text and the captions as Fig. 1, Fig. 2, etc. Figures should be prepared without borders and on white grounding and should be sent separately in their original formats. If a figure is composed of several parts, please mark each part with a), b), c), etc. and provide an explanation for each part in Figure caption. The caption should be self-explanatory. Letters and numbers should be readable (Arial or Times New Roman, min 6 pt with equal sizes and fonts in all figures). Graphics (submitted as supplementary files) may be exported in resolution good enough for printing (min. 300 dpi) in any common format, e.g. TIFF, BMP or JPG, PDF and should be named Fig1.jpg, Fig2.tif, etc. However, graphs and line drawings should be prepared as vector images, e.g. CDR, AI. Multi-curve graphs should have individual curves marked with a symbol or otherwise provide distinguishing differences using, for example, different thicknesses or dashing.

**Tables** should carry separate titles and must be numbered in consecutive numerical order in the text and referred to in both the text and the captions as Table 1, Table 2, etc. In addition to the physical quantities, such as *t* (in italics), the units [s] (normal text) should be added in square brackets. Tables should not duplicate data found elsewhere in the manuscript. Tables should be prepared using a table editor and not inserted as a graphic.

## REFERENCES:

A reference list must be included using the following information as a guide. Only cited text references are to be included. Each reference is to be referred to in the text by a number enclosed in a square bracket (i.e. [3] or [2] to [4] for more references; do not combine more than 3 references, explain each). No reference to the author is necessary.

References must be numbered and ordered according to where they are first mentioned in the paper, not alphabetically. All references must be complete and accurate. Please add DOI code when available. Examples follow.

### Journal Papers:

Surname 1, Initials, Surname 2, Initials (year). Title. *Journal*, volume, number, pages, DOI code.

- [1] Hackenschmidt, R., Alber-Laukant, B., Rieg, F. (2010). Simulating nonlinear materials under centrifugal forces by using intelligent cross-linked simulations. *Strojniški vestnik - Journal of Mechanical Engineering*, vol. 57, no. 7-8, p. 531-538, DOI:10.5545/sv-jme.2011.013.

Journal titles should not be abbreviated. Note that journal title is set in italics.

### Books:

Surname 1, Initials, Surname 2, Initials (year). Title. Publisher, place of publication.

- [2] Groover, M.P. (2007). *Fundamentals of Modern Manufacturing*. John Wiley & Sons, Hoboken.

Note that the title of the book is italicized.

### Chapters in Books:

Surname 1, Initials, Surname 2, Initials (year). Chapter title. Editor(s) of book, book title. Publisher, place of publication, pages.

- [3] Carbone, G., Ceccarelli, M. (2005). Legged robotic systems. Kordić, V., Lazinica, A., Merdan, M. (Eds.), *Cutting Edge Robotics*. Pro literatur Verlag, Mammendorf, p. 553-576.

### Proceedings Papers:

Surname 1, Initials, Surname 2, Initials (year). Paper title. Proceedings title, pages.

- [4] Štefanič, N., Martinčević-Mikić, S., Tošanović, N. (2009). Applied lean system in process industry. *MOTSP Conference Proceedings*, p. 422-427.

### Standards:

Standard-Code (year). Title. Organisation. Place.

- [5] ISO/DIS 16000-6.2:2002. *Indoor Air - Part 6: Determination of Volatile Organic Compounds in Indoor and Chamber Air by Active Sampling on TENAX TA Sorbent, Thermal Desorption and Gas Chromatography using MSD/FID*. International Organization for Standardization. Geneva.

### WWW pages:

Surname, Initials or Company name. Title, from <http://address>, date of access.

- [6] Rockwell Automation. Arena, from <http://www.arenasimulation.com>, accessed on 2009-09-07.

## EXTENDED ABSTRACT:

When the paper is accepted for publishing, the authors will be requested to send an **extended abstract** (approx. one A4 page or 3500 to 4000 characters or approx. 600 words). The instruction for composing the extended abstract are published on-line: <http://www.sv-jme.eu/information-for-authors/>.

## COPYRIGHT:

Authors submitting a manuscript do so on the understanding that the work has not been published before, is not being considered for publication elsewhere and has been read and approved by all authors. The submission of the manuscript by the authors means that the authors automatically agree to publish the paper under CC-BY 4.0 Int. or CC-BY-NC 4.0 Int. when the manuscript is accepted for publication. All accepted manuscripts must be accompanied by a Copyright Agreement, which should be sent to the editor. The work should be original work by the authors and not be published elsewhere in any language without the written consent of the publisher. The proof will be sent to the author showing the final layout of the article. Proof correction must be minimal and executed quickly. Thus it is essential that manuscripts are accurate when submitted. Authors can track the status of their accepted articles on <https://en.sv-jme.eu/>.

## PUBLICATION FEE:

Authors will be asked to pay a publication fee for each article prior to the article appearing in the journal. However, this fee only needs to be paid after the article has been accepted for publishing. The fee is 380 EUR (for articles with maximum of 6 pages), 470 EUR (for articles with maximum of 10 pages), plus 50 EUR for each additional page. The additional cost for a color page is 90.00 EUR (only for a journal hard copy; optional upon author's request). These fees do not include tax.



<http://www.sv-jme.eu>

# Contents

## Papers

- 377 Balsam H. Abed, Ali A. Battawi, Abdul Wahab H. Khuder:  
**Effect of Immersion Media for Polyester Composite Reinforced with Chicken Feathers on Creep Behaviour**
- 385 Yunyue Xie, Qingliang Zeng, Kao Jiang, Zhaosheng Meng, Qinghai Li:  
**Investigation of Dynamic Behaviour of Four-Leg Hydraulic Support under Double-Impact Load**
- 395 HudaElslam Mohamed, Unal Camdali, Atilla Biyikoglu, Metin Actas:  
**Enhancing the Performance of a Vapour Compression Refrigerator System Using R134a with a CuO/CeO<sub>2</sub> Nano-refrigerant**
- 411 Tie Zhang, Yachao Cao, Guangcai Ma:  
**Indices to Evaluate the Performance of Force Transmission and Constraint for Parallel Mechanisms**
- 424 An-Le Van, Trung-Thanh Nguyen:  
**Optimization of Friction Stir Welding Operation using Optimal Taguchi-based ANFIS and Genetic Algorithm**
- 439 Kanmani Ganesan, Saravanan Sambasivam, Rajesh Ramadass:  
**Determination of Limiting Dome Height (LDH) Values for Inconel 718 Alloy Sheet Using FEA and a Hemispherical Punch Method**